DISSERTATION

submitted to the
COMBINED FACULTIES OF THE
NATURAL SCIENCES AND MATHEMATICS

of the
RUPERTO-CAROLA-UNIVERSITY
OF HEIDELBERG, GERMANY

for the degree of
DOCTOR OF NATURAL SCIENCES

Put forward by
CÉDRIC DANIEL GHISLAIN BODET
born in **Charleroi (D1), Belgium**

Oral examination:
January 19, 2011

DYNAMICS OF QUANTUM STATISTICAL CORRELATIONS IN ULTRACOLD BOSE GASES

Abstract

The dynamical evolution of an ultracold Bose gas distributed across the sites of an optical lattice is investigated theoretically in the framework of the Bose-Hubbard model. First, the focus is set on the evolution of squeezing correlations in the two mode system. It is shown that the eigenstates of the Hamiltonian do not exploit the full region of possible squeezing allowed by Heisenbergs uncertainty relation for number and phase fluctuations. The development of nonclassical correlations and relative number squeezing is studied at the transition from the Josephson to the Fock regime. Comparing the full quantum evolution with classical statistical simulations allows us to identify quantum aspects of the squeezing formation. In the quantum regime, the measurement of squeezing allows us to distinguish even and odd total particle number states. Then, a far from equilibrium quantum field theory method, the so-called two-particle-irreducible effective action approach, is presented for the description of the dynamics in larger lattices. The resulting dynamics is compared to the classical statistical time evolution. The validity of the quantum field evolution is probed for various initial conditions in the classical regime.

Zusammenfassung

Die dynamische Entwicklung eines ultrakalten Bose-Gases in einem optischen Gitter wird theoretisch im Rahmen des Bose-Hubbard-Modells untersucht. Zuerst liegt der Fokus auf der Beschreibung der Korrelationen in gequetschen Zuständen eines zwei-Moden Systems. Es wird gezeigt, dass die Eigenzustände des Hamilton-Operators nicht das volle Spektrum abdecken, das von der Heisenbergschen Unschärferelation für Teilchenzahl- und Phasenfluktuationen erlaubt ist. Die Entwicklung von nicht-klassischen Korrelationen und von Quetschen in der Teilchenzahldifferenz wird am Über-gang von dem Josephson- in das Fock-Regime untersucht. Der Vergleich der vollen quan-tenmechanischen Zeitentwicklung mit klassischen, statistischen Simulationen ermöglicht es uns, Quanten-Aspekte der Entstehung von gequetschen Zuständen zu identifizieren. In dem Quantenregime erlaubt uns die Messung der Quetschung gerade und unger-ade Gesamtbesetzungszahlzustände zu unterscheiden. Dann wird eine Methode aus der Nichtgleichgewichts-Quantenfeldtheorie, die Methode der Zwei-Teilchen-irreduziblen ef-fektiven Wirkung, für die Beschreibung der Dynamik in größeren Gittern vorgestellt. Die resultierende Dynamik wird mit der klassischen statistischen Entwicklung verglichen. Die Gültigkeit der quantenfeldtheoretischen Evolution wird dann für verschiedene An-fangsbedingungen im klassischen Bereich überprüft.

Acknowledgements

I would like to start this thesis by thanking all those that helped my realize this work. First, I would like to thank my supervisor, Thomas Gasenzer, who guided me throughout this work and M.K. Oberthaler for his experimental insight. Special acknowledgments go to my two other examiners, J. Evers and M. Schmidt. Finally, without particular order, my thanks go to J. Estève, D. Gonţa, C. Gross, M. Holland, S. Kessler, M. Kronnenwett, A. Maurissen, P. Maurissen, D. Meiser, B. Nowak, B. M. Penden, R. Pepino, D. Sexty, K. Temme, D. Tieri, M.-.I Trappe, and all those that I forgot to mention here.

Contents

Chapter 1

Introduction

In the beginning of the 20th century, quantum mechanics introduced the concept of matter-wave duality. It brought to us an explanation for phenomena such as black-body radiation and the photoelectric effect, and eventually allowed for important applications such as the laser. The classical physics known before was shown to result as a specific limiting case of the new, more general quantum physics. The quantum theory is built on the concept of the wave function which brought the important idea of interference into play. This leads to quantum effects that cannot be described by the classical statistical description of physics.

In recent years, Bose-Einstein condensation (BEC) of cold atomic gases has opened a whole new field of experimental investigation of those quantum effects. BEC was predicted more than eighty years ago by A. Einstein [Eins24], initiated by Bose's new formulation of the statistical properties of photons [Bose24]. It was not, however, before 1995, with the experimental realization of such a condensate in dilute alkali gases at JILA [Ande95] and MIT [Davi95], that this state of matter could really start to revolutionize the field of atomic physics. In a BEC, a large fraction of massive bosonic particles are condensed into the same quantum state. Since the thermal noise is very small as compared to the case of "normal" matter, BECs form a good ground for studying certain quantum effects and performing high-precision measurements.

Quantum mechanics predicts a fundamental limit for the precision of simultaneous measurements in the form of Heisenberg's uncertainty relations [Heis27, Cond29, Robe29]. For a single particle, this limit determines the shot noise [Giov04], and the precision gained by repeating an experiment many times scales with the inverse of the square root of the number of times it is performed. If one considers an ensemble of N non-interacting uncorrelated particles in the condensate, the square-root of the variance divided by the mean of generic variables scales like $1/\sqrt{N}$ with N the particle number [Giov06]. This limit is called the standard quantum limit.

Nowadays, some of the most precise measurements have reached the standard quantum limit [Sant99, Arci06, Goda08]. Despite this apparent fundamental limit, the precision can be increased even further. The strategy is to exploit correlations formed by the interactions between particles which lead to so-called squeezing. Heisenberg's uncertainty relations pose a lower bound to the product of the variances of conjugate variables. Therefore, one can reduce the uncertainty on a particular variable of interest at the expense of its conjugate. In other words, at the standard quantum limit, the area of incertitude can be seen as a circle in the plane defined by the variances of the two observables considered. To gain precision, this circle can be squeezed to an ellipse reducing the variance in the direction of interest. As it would happen when one squeezes a balloon, its size in the other directions increases, in our case to satisfy Heisenberg's uncertainty relations.

In the following, we consider a gas of bosons distributed over the two sites of a double-well trap. This two-mode system can be easily used to describe other systems, such as an isospin. This is why squeezing of a two-mode system is usually called spin-squeezing. A method to obtain a spin squeezed state in a two mode system was first proposed by Kitagawa et al. in 1993 [Kita93]. Its use for precision measurements and atom interferometers was proposed later by Wineland [Wine94]. The idea is to send a state with squeezing correlations into a Ramsey interferometer. This interferometer involves coupling of the two modes, followed by a certain time of free evolution before coupling again the modes to allow analysis of their phase difference [Rams50]. Tuning the intermediate evolution allows to perform measurements with precision better than given by the standard quantum limit.

It was pointed out that there is a close link between spin squeezing and quantum entanglement [Søre01a, Søre01b]. This lead to the proposal to use spin squeezed states for quantum teleportation of continuous variables. Different schemes were proposed in Refs. [Benn93, Vaid94, Brau98].

In the first part of this thesis, we study the production of spin squeezing in an ultra-cold Bose gas enclosed in a double-well trap. Our study was motivated by an experiment performed by the group of M. K. Oberthaler at the Kirchhoff Institute for Physics in Heidelberg. The results of this experiment were presented in Ref. [Estè08]. Similar squeezed states were used later by the same group in an interferometry experiment involving two hyperfine states of ^{87}Rb to beat the standard quantum limit [Gros10]. In the experiment we consider, the atoms are cooled in a series of successive steps and condensed to a BEC in a final double-well trap. The double well is created by adding a short-wavelength periodic optical trap on top of a wider optical dipole trap producing an overall confinement. The short-wavelength lattice is created by two lasers that intersect at a set angle. Within this intersection, a standing wave is created whose wavelength can be tuned by variation of the angle. The height of the barrier between the wells can be changed by adjusting the intensities of the two lasers. One can tune the dipole outer
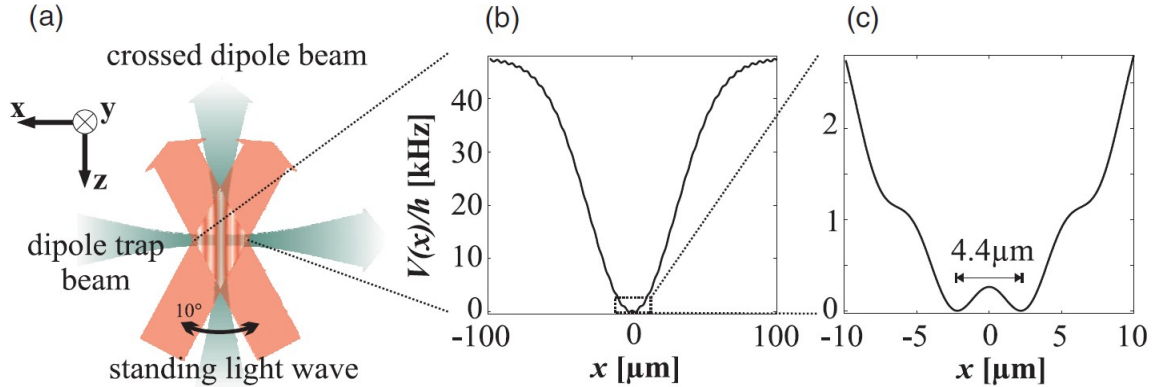
FIGURE 1.1: Sketch of the trapping potential created in Ref. [Estè08]. Picture taken from Ref. [Gati06].

trap in such a way that only two of the minima of the optical lattice are populated, hence creating a double-well trap. A sketch of the final trap is presented in FIG. 1.1.

Tuning the barrier height can be employed for the production of many-body states with squeezing in the relative number difference of particles. This squeezing occurs in the suppression of the fluctuations of the relative number difference of particles in the two wells. In the experiment described above, such squeezing was observed in the distribution of atoms, by counting them after high-resolution imaging of the atom cloud in subsequent runs and by calculating the variance of the resulting count. In each such run, a condensate was prepared in the double-well trap with a low barrier height, allowing the atoms to be delocalized across the almost flat potential floor. Then, the potential barrier was slowly raised, allowing for an almost adiabatic adjustment of the system's state to the modified external conditions. They observed that the finally strong barrier suppresses the fluctuations in the particle number difference below the classical limit. This suppression was interpreted as due to the squeezing that manifests itself theoretically in the approximate low-energy many-body eigenstates.

Other groups have realized experiments with spin squeezed states with laser cooled atoms [Schl08], and using other methods, for example in vapor cells [Hald99, Fern08, Appe09] or ion traps [Meye01]. Those experiments focus on the realization of squeezing in the objective of improving measurement sensitivity beyond the standard quantum limit. The systems uses different atoms at different temperatures in various trapping schemes, but all discuss the use of squeezed states for interferometry experiments.

A theoretical description of a non-relativistic gas in an optical lattice at ultralow temperatures is provided by the Bose-Hubbard Hamiltonian. Its derivation from a general bosonic many-particle Hamiltonian is presented in Chapter 2. This discrete

model will be used throughout the thesis. The properties of the energy spectrum of the two-mode Bose-Hubbard Hamiltonian are discussed in Chapter 3. We introduce the Schwinger angular-momentum operators to discuss the fundamental squeezing limits in the Bloch-sphere picture. We show that the Heisenberg limit cannot be reached, in the generic case, by adiabatically changing the systems parameters, starting from an incoherent mixture of energy eigenstates. In particular, in the ground state of the system, though being rather close to the Heisenberg limit, the variances of the conjugate variables number difference and relative phase between the wells are in general not minimized at the Heisenberg limit.

A prominent motivation of the work presented here is to study the role of quantum statistical fluctuations in the preparation of the spin-squeezed states. The quantum evolution is obtained by exact numerical integration of the Bose-Hubbard Hamiltonian. By comparison of those results with semiclassical Monte Carlo simulations, we show in Chapter 4 that the spin squeezing produced in a setup as that in the experiment [Estè08] is equivalent to reduced classical fluctuation of the occupation number difference between the two wells. The production of squeezed states in the experiment follows a quasistatic path in state space, the reduction of the fluctuations arises from the evolution of the eigenstates towards well-defined number states.

We show that quantum effects can be seen when producing squeezed states. However, due to the low degree of degeneracy in the system, it is possible only at significantly lower temperatures than in the experiment. The detection of such squeezing and quantum correlations requires the measurement of particle number at the single-particle level. In those cases, crucial differences arise for systems with an even total particle number as compared to such with an odd number.

In the second part of the thesis, we depart from the description of the double-well and the production of squeezing to focus on the description of a Bose gas on larger lattices. As the Hilbert space grows exponentially with the number of lattice sites, we can no longer use the exact numerical integrations from the first part. The numerical effort would be prohibitive. Providing a good description of the dynamics of larger system leads us to quantum field theoretic methods for quantum many-body dynamics.

Quantum many-body dynamics poses a series of general problems that are usually not solvable exactly. In some particular cases, analytic solutions to the models can be found [Zima64] and can be used to benchmark more general approximative techniques. The Lieb-Liniger model is an example [Lieb63], it describes the evolution of a continuous 1D Bose gas with contact interaction and periodic boundary conditions. For instance, the analytic evolution of the wave-function of an initially trapped gas allowed to expand freely was calculated in Ref. [Bulj08]. But the evaluation of the relevant observables necessitates the resolution of a number of integrals scaling with the number of particles. This renders the exact solution of the model unpractical for many-body physics with

large particle numbers.

Numerical techniques were developed to describe more general systems such as the density-matrix renormalization group (DMRG) [Scho05, Whit04], time-dependent block-decimation [Vida04] and functional renormalization group [Gase08] methods. Semi-classical simulation techniques were also studied [Stee98b, Blak08, Polk09]. Those techniques can be compared to each other and to special exact solutions, in order to exhibit the most useful method for a particular problem.

Our focus is set on far-from-equilibrium dynamics of a Bose gas in a lattice in one spatial dimension. Far from equilibrium, the evolution cannot be considered as a perturbation of the equilibrium situation and solved using linearization techniques. Other perturbative methods rely on the smallness of the interaction parameters, and the dynamic equation are expanded in powers of this parameter. In strongly coupled systems, this parameter is large and perturbation techniques are no longer valid. Semi-classical Monte-Carlo methods are also used for nonequilibrium dynamics. Those method provide a good description of the system, for as long as quantum fluctuations remain small. As the study of those quantum effects is one of the motivations of this thesis, we need another method for the quantum description of far-from-equilibrium dynamics.

A series of powerful approaches to the problem comes with quantum field theory. In particular, we consider a method called the two-particle-irreducible (2PI) effective action approach [Lutt60, Baym62, Corn74]. The power of this approach comes from the fact that the approximation are made at the level of the action, before the equations of motion are derived. This allows to keep certain symmetries intact at any level of approximation and ensures the conservation of crucial quantities such as particle number and energy. Furthermore, we consider a non-perturbative expansion of the effective action in inverse powers of the number of field components $\mathcal{N}$ [Berg01, Aart02, Gase05]. This is useful, e.g., for a gas of identical bosons described by $\mathcal{N}$ complex scalar field. This truncation technique has the advantage of not being explicitly dependent on the smallness of the interactions, and is valid for strongly coupled systems. In the following, the truncation is made at the next-to-leading order (NLO) in $1/\mathcal{N}$. The 2PI effective action at NLO in $1/\mathcal{N}$ is discussed in detail in the review [Berg05], and the derivation of the equations of motion for the case of the Bose-Hubbard model in 1D is described with and without field expectation values in Refs. [Gase05, Temm06]. We present this approach in the framework of a Bose gas on a lattice in Chapter 5.

This method was compared with exact calculations and the Hartree-Fock-Bogoliubov (HFB) approximation in Ref. [Temm06] for dynamics of a degenerate Bose gas in a 1D lattice for two and three sites. The main results are presented in Fig. 1.2 for a two-site system. Qualitative agreement was found between the results from the 2PI $1/\mathcal{N}$ NLO-expansion and exact calculations. The qualitative improvement over the meanfield HFB and low-order loop approximations is remarkable. Increasing total number of particles
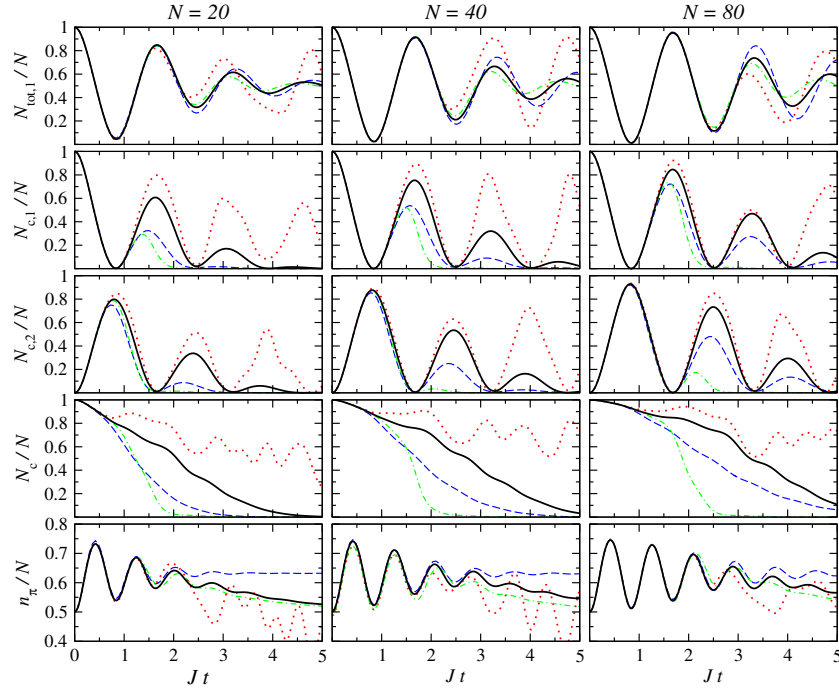
FIGURE 1.2: Time evolution of an ultracold Bose gas in a two-site 1-dimensional lattice and periodic boundary conditions. Several techniques are compared in the evolution of various observables. The three columns show the same quantities, for a different total number of atoms N. The blue dashed lines show the results from an exact calculation [Rey04]. The thick solid lines presents the results from the 2PI $1/\mathcal{N}$ NLO-expansion. The red dotted curves correspond to the Hartree-Fock-Bogoliubov approximation while the green dash-dotted curves show the dynamics resulting from a further approximation of the 2PI $1/\mathcal{N}$ NLO-expansion. More details are to be found in that Ref. [Temm06].

seemed to improve the accuracy of the approximation.

In this work, we investigate the dependence of the quantitative disagreement on the number of lattice sites. As no exact calculations are available, we limit our study to the semiclassical regime and use classical statistical simulations as a reference for the comparison. Our results are presented in Chapter 6, after a discussion of the numerical implementation of the field-theoretic equations and of the classical model. This quantitative disagreement is found to be somewhat smaller for larger lattices, but no general scaling was found. This points to a general limitation of the NLO $1/\mathcal{N}$ approximation at large couplings. We show, however, that evolution of the total occupation of a single site is well described by the 2PI approach while the evolution of the phase coherence is not properly reproduced. Hence, we find a clear sign of the significance of higher-order correlations left out at the level of the approximation.

Chapter 2

Bose gas in a lattice potential

In this thesis, we study the dynamics of a Bose gas trapped on a lattice. In Part I, we will concentrate on the study of gas trapped in a double-well potential with two energetically degenerate minima separated by a barrier of variable height. In Part II, we will look at the dynamics of a gas this time trapped in an optical lattice. In that case, the number of local minima is much higher than two. For both settings, the underlying model is the Bose-Hubbard Hamiltonian, that describes a non-relativistic gas of bosons in an optical lattice. In this chapter, we show a derivation of this Hamiltonian. It is obtained as an approximation of the standard continuous bosonic many-particle Hamiltonian, using Wannier functions as a basis for discretization.

2.1 Hamiltonian

We will now start to present a derivation of the Hamiltonian: Consider a system of identical bosons of mass m, having a binary interaction of the form $V(\vec{x}_i - \vec{x}_j)$. We also add an external potential $V_{\text{ext}}(\vec{x})$, in which the atoms are placed. This system is described by the Hamiltonian

$$
\begin{aligned}
\hat{H} = \int \mathrm{d}^d\vec{x}\; \hat{\Psi}^\dagger(\vec{x}) \left(-\frac{\hbar^2\Delta}{2m} + V_{\text{ext}}(\vec{x}) \right) \hat{\Psi}(\vec{x}) \\
+ \frac{1}{2}\int \mathrm{d}^d\vec{x}\; \mathrm{d}^d\vec{y}\; \hat{\Psi}^\dagger(\vec{x})\hat{\Psi}^\dagger(\vec{y})V(\vec{x}-\vec{y})\hat{\Psi}(\vec{y})\hat{\Psi}(\vec{x}),
\end{aligned}
\tag{2.1}
$$

in d dimensions. The field operators $\hat{\Psi}$ and $\hat{\Psi}^\dagger$ act on the Fock space of totally symmetric wave-functions. They follow the standard bosonic commutation relations

$$
\begin{aligned}
[\hat{\Psi}(\vec{x}), \hat{\Psi}(\vec{y})] = [\hat{\Psi}^\dagger(\vec{x}), \hat{\Psi}^\dagger(\vec{y})] = 0, \\
[\hat{\Psi}(\vec{x}), \hat{\Psi}^\dagger(\vec{y})] = \delta^{(d)}(\vec{x}-\vec{y}).
\end{aligned}
\tag{2.2}
$$

In the situation we will consider, the external potential $V_{\text{ext}}(\vec{x})$ is usually manufactured by light dipole potential coming from detuned lasers. Usually, we need this potential to exhibit some periodicity in order to be able to derive a discrete Hamiltonian. We discuss the considered potential in more details in Sect. 2.2.

As we are considering a dilute gas of Bosons at ultra-cold temperature, the binary interaction can be approximated by a contact potential, $V(\vec{x} - \vec{y}) = g\delta^{(d)}(\vec{x} - \vec{y})$. The coupling constant g is given by $g = 4\pi a_s \hbar^2/m$, where a_s is the s-wave scattering length. This approximation of the real interaction is valid for small energies, where only s-wave scattering between particles has to be considered [Legg01, Mess00]. With this interaction, (2.1) becomes

$$\hat{H} = \int \mathrm{d}^d \vec{x} \, \hat{\Psi}^\dagger(\vec{x}) \left(-\frac{\hbar^2 \Delta}{2m} + V_{\text{ext}}(\vec{x}) \right) \hat{\Psi}(\vec{x}) + \frac{g}{2} \int \mathrm{d}^d \vec{x} \, \hat{\Psi}^\dagger(\vec{x}) \hat{\Psi}^\dagger(\vec{x}) \hat{\Psi}(\vec{x}) \hat{\Psi}(\vec{x}). \quad (2.3)$$

This Hamiltonian will be used to derive the Bose-Hubbard Hamiltonian, but let us have a short digression from here to the classical equation of motion. This equation is obtained from (2.3) by replacing the field operators by a complex field

$$\hat{\Psi}(x) \rightarrow \psi(x). \quad (2.4)$$

Under that approximation, the classical equation of motion for $\psi(x)$ then reads

$$i\hbar \frac{\partial}{\partial t} \psi(\vec{x}) = \left(-\frac{\hbar^2}{2m} \Delta + V_{\text{ext}}(\vec{x}) + g|\psi(\vec{x})|^2 \right) \psi(\vec{x}). \quad (2.5)$$

In the following, we will obtain the semiclassical dynamics of the system from this equation. This equation is formally the same as the Gross-Pitaevskii equation [Gros61, Pita61], which is obtained from (2.3) by using the Liouville equation $i\hbar \partial_t \langle \hat{\Psi} \rangle = \langle [\hat{\Psi}, \hat{H}] \rangle$ and then by approximating the 3-point function $\langle \hat{\Psi}^\dagger(\vec{x}) \hat{\Psi}(\vec{x}) \hat{\Psi}(\vec{x}) \rangle$ by a product of field expectation values $\psi^*(\vec{x}) \psi(\vec{x}) \psi(\vec{x})$. It provides a mean field description of a non-relativistic dilute Bose gas.

2.2   Wannier basis decomposition

We shall now consider the setting of the experiment exposed in Ref. [Estè08]. Six lasers are used to generate a periodic potential in three dimensions. Each dimension uses a pair of counterpropagating lasers. The resulting standing wave gives rise to an standing electric field in which the atoms are traps, due the Stark effect. The number of laser can be reduced to three by using mirrors to create a reflected wave. It shall be noted here that a variety of other atom/laser configurations exists, many of which have been explored experimentally or theoretically [Jaks05].

In the configuration we consider, the laser beams create a optical potential of the form

$$V_{\text{lat}} = V_{0,x} \cos^2(k_x x) + V_{0,y} \cos^2(k_y y) + V_{0,z} \cos^2(k_z z). \tag{2.6}$$

The periodicity a_i of this lattice in the direction $i = x, y, z$ is the half of the laser wavelength in that direction, ie $a_i = \lambda_i/2$. The depth of the potential $V_{0,i}$ is given by the intensity of the laser in that direction. Therefore, the parameters of the potential can be controlled experimentally by changing the intensities and the wavelengths of the lasers.

To create a quasi-one-dimensional lattice, one can take very high intensities for lasers in two of the three dimensions. Since BECs exist only a low energies, the high gap to the first exited state in those direction suppresses the occupation of that state, and the atoms are confined to the transverse ground-state of the system. We can therefore neglect those two dimensions, as the interesting dynamics will happen in the remaining dimension.

The periodicity in the remaining dimension yields to a band structure in energy, which can be described by the basis of Bloch functions $\phi_q^{(n)}(x)$ [Kohn59], with n the band index and q the quasi-momentum. They are defined as

$$\phi_q^{(n)}(x) = e^{iqx} u_q^{(n)}(x), \tag{2.7}$$

where $u_q^{(n)}(x)$ has the same periodicity as the potential [Asch76, Zima64]. However, in our case, it is more convenient to describe the system in a basis which is spatially located. To that end, we use the Wannier functions. This set of orthogonal, real functions, can be obtained by a Fourier transform of the Bloch functions

$$\omega^{(n)}(x - x_j) = \Theta^{-1/2} \sum_q e^{-iqx_j} \phi_q^{(n)}(x), \tag{2.8}$$

where Θ is a normalization constant. These functions are centered around x_j. This allows us to associate the occupation of the Wannier functions to a population of the corresponding lattice bin.

For an infinite lattice depth, $V_0 \to \infty$, the potential tends towards a series of harmonic potentials centered around each lattice bin, and the Wannier functions $\omega^{(n)}(x)$ towards the the n-th excited eigen-function of the corresponding harmonic oscillator [Jaks05].

2.3 The Bose-Hubbard Hamiltonian

The Bose-Hubbard Hamiltonian is derived from the Hamiltonian (2.3) using the Wannier basis. As discussed above, we use a Hamiltonian that is reduced to the one

relevant dimension. Then we separate the now 1D external potential $V_{\text{ext}}(x)$ into two parts. The optical lattice potential $V_{\text{lat}}(x) = V_0 \cos(kx)$, and another trapping potential $V_{\text{trap}}(x)$ used to confine the atoms spatially,

$$V_{\text{ext}}(x) = V_{\text{lat}}(x) + V_{\text{trap}}(x). \tag{2.9}$$

As we will see later, it is also possible to set this last trapping potential to zero, and study delocalized atoms under periodic boundary conditions. In any case, we always assume that the trapping potential varies on a larger scale than the lattice potential. This allows us to decompose the wave function in terms of the Wannier functions, centered around the lattice minima x_i. Furthermore, since we deal with low energy systems, it is sufficient to consider only the first band, neglecting the dynamics in the higher bands of the optical lattice. The field operator can therefore be written as

$$\hat{\Psi}(x) = \sum_i \hat{b}_i \omega^{(0)}(x - x_i), \tag{2.10}$$

where $\hat{b}_i$ is the annihilation operator for a particle in the first-band Wannier mode centered around x_i. Like the field operator (2.2), the operator $\hat{b}_i$ and its conjugate $\hat{b}_i^\dagger$ obey the bosonic commutation relations

$$
\begin{aligned}
[\hat{b}_i, \hat{b}_j] &= [\hat{b}_i^\dagger, \hat{b}_j^\dagger] = 0, \\
[\hat{b}_i, \hat{b}_j^\dagger] &= \delta_{ij}.
\end{aligned}
\tag{2.11}
$$

By inserting the ansatz (2.10) into the Hamiltonian (2.3), we obtain a discrete Hamiltion expressed in terms of the new operators $\hat{b}_i$ and $\hat{b}_i^\dagger$,

$$\hat{H} = -\sum_{i,j} J_{ij} \hat{b}_i^\dagger \hat{b}_j + \sum_{i,j} \epsilon_{ij} \hat{b}_i^\dagger \hat{b}_j + \frac{1}{2} \sum_{i,j,k,l} U_{ijkl} \hat{b}_i^\dagger \hat{b}_j^\dagger \hat{b}_k \hat{b}_l, \tag{2.12}$$

where the parameters J_{ij}, ϵ_{ij} and U_{ijkl} are defined as

$$J_{ij} = -\int \mathrm{d}x \; \omega^{(0)}(x - x_i) \left(-\frac{\hbar^2 \Delta}{2m} + V_{\text{lat}}(x) \right) \omega^{(0)}(x - x_j), \tag{2.13a}$$

$$\epsilon_{ij} = \int \mathrm{d}x \; \omega^{(0)}(x - x_i) V_{\text{trap}}(x) \omega^{(0)}(x - x_j), \tag{2.13b}$$

$$U_{ijkl} = \int \mathrm{d}x \; \omega^{(0)}(x - x_i) \omega^{(0)}(x - x_j) \omega^{(0)}(x - x_k) \omega^{(0)}(x - x_l). \tag{2.13c}$$

It has been shown by numerical calculations [Jaks05] that, for reasonably deep lattices, the values of the non-local matrix elements U_{ijkl} are small compared to on-site interaction $U_i = U_{iiii}$, as the overlap of the corresponding Wannier function is small.

The same argument holds for ϵ_{ij}, dominated by $\epsilon_i = \epsilon_{ij}$. Also, because of the Laplacian operator Δ, the J_{ij} matrix is dominated by nearest neighbor tunneling $J_i = J_{i,i+1}$. Furthermore, if the trapping potential does not affect too much the lattice potential $V_{\text{lat}} \gg V_{\text{trap}}$, one can take the same value for each interaction parameter $U = U_i$ and hopping parameter $J = J_i$. With those assumptions, the Hamiltonian (2.12) rewrites as

$$\hat{H} = -J \sum_i (\hat{b}_i^\dagger \hat{b}_{i+1} + \hat{b}_{i+1}^\dagger \hat{b}_i) + \sum_i \epsilon_i \hat{b}_i^\dagger \hat{b}_i + \frac{U}{2} \sum_i \hat{b}_i^\dagger \hat{b}_i^\dagger \hat{b}_i \hat{b}_i, \tag{2.14}$$

which is the standard Bose-Hubbard Hamiltonian in one dimension.

Using the completeness relation of the Wannier function, one sees that the integral needed to calculate ϵ_i simplifies to the actual value of the trapping potential at the position of lattice minimum, $\epsilon_i = V_{\text{trap}}(x_i)$.

2.3.1 $\mathcal{O}(2)$ decomposition

The spectrum of this Hamiltonian will be studied in detail in Chapter 3, in the particular case of a double-well trap. However, in Part II, it will be more convenient to study this Hamiltonian in a slightly different basis, that we discuss in this section.

We choose to decompose the complex-value operator $\hat{b}_i$ into a two-component field in $\mathbb{R}^2$, defined in the following way

$$\hat{b}_i = \frac{1}{\sqrt{2}} \left(\hat{\Phi}_i^0 + i\hat{\Phi}_i^1 \right), \tag{2.15a}$$

$$\hat{b}_i^\dagger = \frac{1}{\sqrt{2}} \left(\hat{\Phi}_i^0 - i\hat{\Phi}_i^1 \right). \tag{2.15b}$$

Those operators obey commutation relations easily derived from (2.11), and are

$$[\hat{\Phi}_i^a, \hat{\Phi}_i^b] = -ih^{ab}\delta_{ij}, \tag{2.16}$$

where the newly introduced 2×2-matrix h^{ab} is defined by

$$\left(h^{ab} \right) = \begin{pmatrix} 0 & -1 \\ 1 & 0 \end{pmatrix}. \tag{2.17}$$

Using this new operator, the Bose-Hubbard Hamiltonian (2.14) rewrites as

$$\hat{H} = -J \sum_i \sum_a (\hat{\Phi}_i^a \hat{\Phi}_{i+1}^a) + \sum_i \frac{\epsilon_i}{2} \sum_a \hat{\Phi}_i^a \hat{\Phi}_i^a + \frac{U}{8} \sum_i \sum_{a,b} \hat{\Phi}_i^a \hat{\Phi}_i^a \hat{\Phi}_i^b \hat{\Phi}_i^b, \tag{2.18}$$

where we have neglected a constant term equal to $\sum_i (\epsilon_i/2 + U/8)$. This expression of the Hamiltonian will be used in Part II.

Part I

Two-mode model:
Beyond classical squeezing

Chapter 3

The two-mode Bose gas

In this first part of the thesis, we will study the production of squeezed states of a Bose gas in a double well trap. We have discussed in Chapter 2 how a condensate could be placed on a one dimensional lattice. The external trapping potential $V_{\text{trap}}(x)$ is assumed to be harmonic. By tuning its intensity and the position, one can create a potential with two degenerate minima, the other local minima being raised to an energy high enough to have their occupation suppressed when filled with an ultracold Bose gas. Such a setup was realized, for instance, in the experiment of J. Estève et al. [Estè08].

Such a trap creates a so-called double-well system, where the intensity of the lattice potential $V_{\text{lat}}(x)$ is directly related to the height of the barrier. This intensity dependence allows an easy experimental control on the height of the barrier. The shape of the potential for two values of the intensity of the barrier of the lattice V_0 is shown in FIG. 3.1. Mathematically discretized with the Bose-Hubbard Hamiltonian, this setup becomes a two-mode problem. The properties that will be discussed here can easily be mapped to other two-modes systems, for instance a gas of bosons with an internal degree of freedom, e.g. an hyperfine state.

We will concentrate on the dynamical production of squeezed states in a double-well, under the framework of the Bose-Hubbard Hamiltonian. While Section 3.1 gives some motivations on why such states are of particular interest, the rest of the chapter focuses on the static properties of the two-mode Bose-Hubbard Hamiltonian, i.e. the properties of its spectrum, while in Chapter 4, we investigate the dynamics of the system, and the production of the squeezed states.
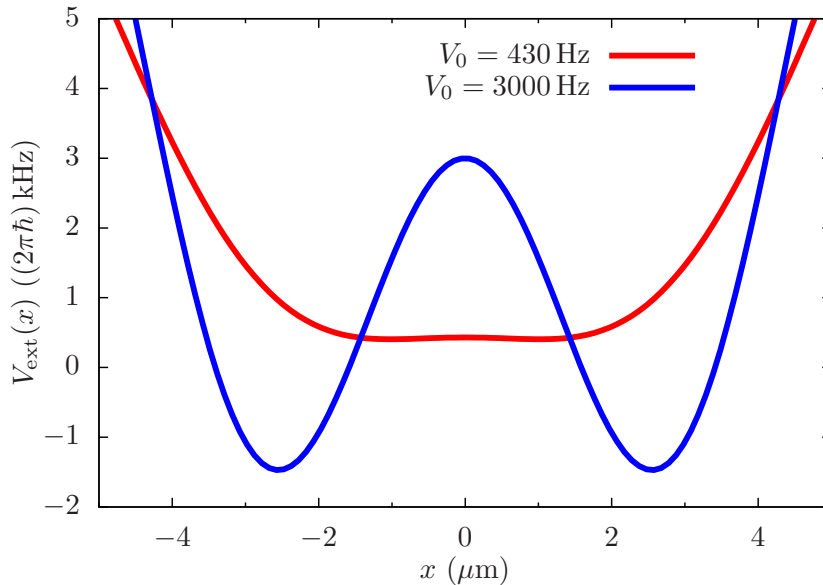
FIGURE 3.1:   Trapping potential V_{ext} realised in the experiment [Estè08] for two different barrier heights before (red) and after (blue) an adiabatically conducted ramp-up.

3.1   Motivations on number squeezing

So far, technical difficulties have been the main source of error in physical experiments. Nowadays, as those are mastered, an intrinsic physical principle must now be taken into account: Heisenberg's uncertainty relation. This principle limits precision measurements at the quantum level. As a matter of fact, this standard quantum limit is already reached by today's best sensors of various quantities such as time [Sant99] and position [Arci06, Goda08].

This principle implies that squeezing an observable of interest, i.e. decreasing its fluctuations below the standard quantum limit given by the central limit theorem, necessarily increases the fluctuations in one or more conjugate observables. However, different ways to use such squeezed states, e.g., to measure frequency in Ramsey-type interferometers have been discussed in great detail in the past [Wine92, Kita93, Wine94, Boll96]. For example, Heisenberg-limited Mach-Zehnder interferometry using number squeezed photon states were studied in detail in Refs. [Holl93, Kim98, Huel97, Dunn02].

In the case of non-interacting particles, a two-mode Bose-Einstein condensate is a coherent semiclassical macroscopic ensembles of particles. Therefore, in the limit of zero temperature, the probability for each mode to contain a certain number of atoms is binomial. For large total particle number N, it is therefore approximately Poissonian. Hence, the variance $(\Delta n)^2$ of the particle number difference is directly proportional to the

total particle number N, and the standard quantum limit then reads $(\Delta n)/N \sim 1/\sqrt{N}$.

The observable that we associate to the particle number difference in the Heisenberg uncertainty relation is the relative phase ϕ between the modes which can be measured, e.g., through interference effects. In a closed non-relativistic system of massive particles, both phase and particle number can only be measured relative to that of a different system, or they can be measured locally comparing the system at different space-time points. In such a closed system, a finite mass implies a fixed total particle number and therefore an undefined total phase. The Heisenberg uncertainty relation $\Delta n \Delta \phi \sim 1$ leads to the relative standard deviation $(\Delta \phi)/\phi \sim 1/\sqrt{N}$.

However, the presence of interactions between the particles strongly modifies the situation. Fluctuations of the particle number and squeezing in trapped atomic gases have been the subject of numerous recent experimental and theoretical studies [Orze01, Grei02, Gerb06, Sebb07, Jo07, Li07, Estè08]. Here, we are mainly interested in squeezed states of Bose-Einstein condensed ensembles of trapped atoms. As mentioned above, we specifically consider squeezing in the particle number difference between the two minima of a double-well trap in one spatial dimension. Of course, this reduction of number fluctuations below the standard quantum limit occurs at the expense of increased fluctuations in the relative phase between the wells.

Such two-mode quantum systems can be described, by use of Schwinger's representation, in terms of angular momentum states with the maximum length of the spin vector related to the total particle number. Consequently, the non-classical states we consider exhibit a variant of spin squeezing [Wine92, Kita93].

3.2   Hamiltonian for a Bose gas in a double-well trap

Here, we consider a Bose condensate trapped in a double-well potential with two energetically degenerate minima separated by a barrier of variable height. We will show in this section that the Bose-Hubbard Hamiltonian derived in Chapter 2 can also be used for this model, using a different set of arguments. The barrier between the wells of the system is taken much smaller than the outer walls of the trap such that the main source of number fluctuations in each well is given by tunneling processes between the wells.

In the experiment [Estè08] such a potential was formed optically by counterpropagating laser waves creating the superposition of standing waves with two different frequencies. Near the trapping minima the potential can be approximately described as

$$V_{\text{ext}}(x) = V_0 \cos(kx) + \frac{1}{2}m\omega^2 x^2 \qquad\qquad (3.1)$$

In the experiment [Estè08], the frequency of the harmonic trap was chosen $\omega \simeq (2\pi)5\,\mathrm{Hz}$ while the amplitude of the barrier was varied in the range between $V_0 \simeq (2\pi)430\,\mathrm{Hz}$ and $V_0 \simeq (2\pi)3\,\mathrm{kHz}$. FIG. 3.1 shows the potential in these limits. The slow ramp-up splits the two wells, and has the effect of decreasing the hopping between them, and therefore also the fluctuation of the particle number.

Considering the shape of the potential (3.1) for the values of V_0 shown in FIG. 3.1 and the low temperatures encountered in the experiment, the occupation of the other minima of $\cos(kx)$ will be greatly suppressed. At first glance, one could think that it would be sufficient to consider the Hamiltonian (2.14) and by considering only two sites $N_S = 2$. However, in Chapter 2, we made the assumption that the external trapping potential was only slightly modifying the shape of Wannier functions arising from the lattice. This is unfortunately not true anymore for a double-well potential. We will briefly describe here how one can show, by assumptions valid for the double-well, that the Bose-Hubbard Hamiltonian (2.14) also describes this system.

We start again from the equation (2.3), that we repeat here for convenience,

$$\hat{H} = \int \mathrm{d}^d\vec{x}\; \hat{\Psi}^\dagger(\vec{x}) \left(-\frac{\hbar^2\Delta}{2m} + V_{\mathrm{ext}}(\vec{x}) \right) \hat{\Psi}(\vec{x}) + \frac{g}{2} \int \mathrm{d}^d\vec{x}\; \hat{\Psi}^\dagger(\vec{x})\hat{\Psi}^\dagger(\vec{x})\hat{\Psi}(\vec{x})\hat{\Psi}(\vec{x}). \quad (3.2)$$

This time, we consider the external potential given in Eq. (3.1). For a single particle, the ground and first excited states of the Hamiltonian (2.5), in the absence of a barrier ($V_0 = 0$), are the corresponding harmonic oscillator eigenstates. The ground (excited) state is (anti-)symmetric under the reflection $r \to -r$. Raising the barrier adiabatically these states are transformed into the lowest two energy eigenstates $\psi_0(x)$, $\psi_1(x)$ in the double well, both with amplitudes peaked within the two wells. Those two states retain, of course, the symmetry of the harmonic oscillator states.

For the typical temperatures reached in the experiment, ie around 20 nK, we can restrict ourselves to describe the system using those two functions, as the occupation of the higher states will be suppressed. It is furthermore convenient to work with localized functions. To that end, we use a linear combination of those states,

$$\psi_l(x) = \frac{1}{\sqrt{2}}(\psi_0(x) + \psi_1(x)), \quad (3.3\mathrm{a})$$

$$\psi_r(x) = \frac{1}{\sqrt{2}}(\psi_0(x) - \psi_1(x)). \quad (3.3\mathrm{b})$$

Using the symmetry properties of the two lowest eigenstates, one can see that $\psi_l(x)$ (and $\psi_r(x)$) are localized around the left (right) well, respectively. Then, one makes the following ansatz on the field operator.

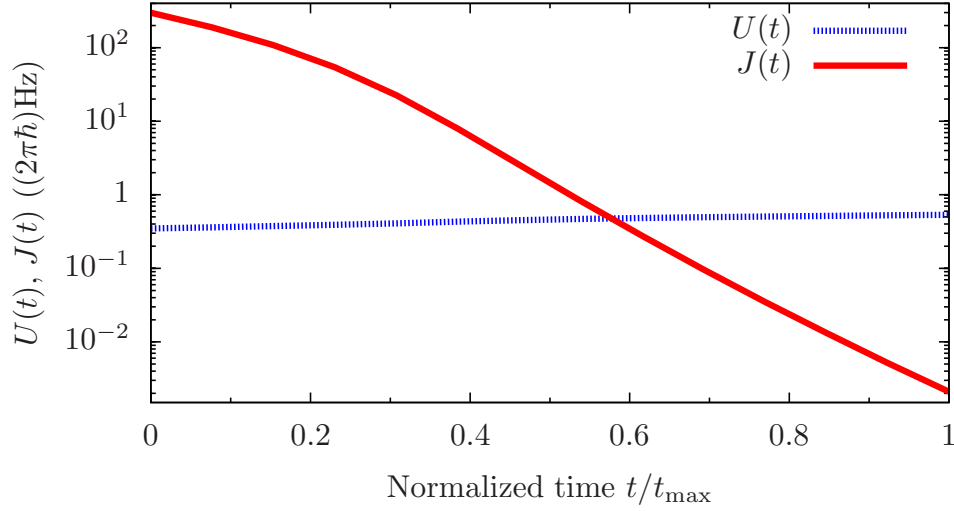$$\hat{\Psi}(x) = \hat{b}_1\psi_l(x) + \hat{b}_2\psi_r(x), \quad (3.4)$$

FIGURE 3.2: Time evolution of the parameters $U(t)$ and $J(t)$ of the Bose-Hubbard Hamiltonian as realized in the experiment [Estè08]. This evolution drives the system from the Rabi to the Fock regime.

where the operators $\hat{b}_i$ and $\hat{b}_i^\dagger$ also obey the bosonic commutation relations (2.11). Then, after a derivation similar to the one used in Section 2.3, one obtains again the Bose-Hubbard Hamiltonian, this time for two sites

$$\hat{H} = -J(\hat{b}_1^\dagger \hat{b}_2 + \hat{b}_2^\dagger \hat{b}_1) + \frac{U}{2} \sum_{i=1}^{2} \hat{b}_i^\dagger \hat{b}_i^\dagger \hat{b}_i \hat{b}_i. \tag{3.5}$$

where J is the tunneling and U is the onsite interaction parameter. Here, we consider that the two minima of the potential are degenerate, this means $\epsilon_i = 0$ in Eq. (2.14).

The parameters U and J are obtained by solving the three-dimensional Gross-Pitaevskii equation for the trapping potential realized in [Estè08] as functions of the barrier height between the wells. Then, the solutions for $\psi_l(x)$ and $\psi_r(x)$ are inserted in Eqs. (2.13) instead of the Wannier functions. Solving the integrals gives us values for U and J. Those parameters are shown, for the potential valid during the near-adiabatic ramp, in FIG. 3.2. This calculation was done for the barrier heights relevant in the experiment by S. Giovanazzi et al., see Ref. [Giov08].

As we see in FIG. 3.3, for potentials between the limiting cases depicted in FIG. 3.1 the minimum width of the lowest band of states is obtained in the limit of large U/J, i.e. it is where the scaling parameter s is the lowest. As will become clear in the following section, see e.g. Eq. (3.8), the width in this limit is approximately $UN^2/4 \simeq (2\pi)1.2\,\text{kHz}$, for a total number of particles $N = 100$. To estimate the validity of the single-band

model this needs to be compared to the typical temperatures in the experiment which are on the order of 100 nK, i.e., 10^{-7} Hz. This is much lower than the band width, therefore we can say that our dynamics stay within that first single band.

Properties of the Hamiltonian (3.5) and the fragmentation of a Bose-condensate in a double-well potential have been discussed in detail before [Cira98, Stee98a, Spek99, Meno01, Mahm03, Stre04, Isel05, Isel06, Stre07], and we review here only the aspects relevant to our discussion. See Refs. [Ribe07, Ribe08] for a determination of the spectrum in the thermodynamic limit. For a general review see Ref. [Legg01]. See also Refs. [Dunn99, Dunn01] for proposals for the manipulation of number and phase correlations in condensates trapped in a double well.

In the next two sections, we mainly present the result of our work, that was to put together and understand the various results relevant to our study. Furthermore, we present our numerical results on the static properties of the Hamiltonian (3.5). Those results were obtained for values of the parameters relevant in the experiment we follow.

3.3   Energy spectrum

As we have a fixed total number of particles N, it means that we are considering the canonical ensemble. A convenient basis to express the energy eigenstates of (3.5) in, are the Fock number eigenstates of $\hat{n} = (\hat{b}_1^\dagger \hat{b}_1 - \hat{b}_2^\dagger \hat{b}_2)/2$,

$$\hat{n} \, |N/2 + n, N/2 - n\rangle = n \, |N/2 + n, N/2 - n\rangle , \qquad (3.6)$$

with $-N/2 \leq n \leq N/2$. Since the total number of particle is fixed, a Fock state will be referred to as, simply, $|n\rangle = |N/2 + n, N/2 - n\rangle$.

In that case, the dimension of the Hilbert space is $N+1$. This grows slow enough that the Hamiltonian can be diagonalized exactly, using numerical methods. In practice, this allows us to study the energy spectrum by diagonalizing numerically the Hamiltonian and in Chapter 4 to study its evolution by integrating, also numerically, the exact equations of motion derived from this Hamiltonian. In general, we will take a particle number of $N = 100$ in the following illustrations. While diagonalization can be made for higher particle count, the value we chose allows us to calculate the dynamics within a reasonable time.

As far as the form of the spectrum is concerned, three different regimes can be distinguished by means of the ratio U/J [Para01]. In the *Rabi regime*, $U/J \ll N^{-1}$, the system consists of N nearly independent particles. This corresponds to the non-interacting limit. In the *Josephson regime*, $N^{-1} \ll U/J \ll N$, atom number fluctuations are small and coherence is high. This is called the classical regime as eigenstates are described by predominantly positive Wigner functions with widths near the standard

FIGURE 3.3: Spectrum of the Bose-Hubbard Hamiltonian in different regimes. The energies are given in units of U/s, with s a scale factor given in the legend. All energies are shifted such that $E_0 = 0$.

quantum limit. The *Fock regime*, $N \ll U/J$, is dominated by the interaction energy U, thus the atom number in each well is well defined. Reduced number fluctuations and other non-classical effects appear in the Fock regime.

In the Rabi regime, the spectrum consists of a series of equally spaced states with a level spacing of ω_p where the plasma frequency ω_p is given by

$$\omega_p = \sqrt{2J\left(NU + 2J\right)}. \tag{3.7}$$

Increasing U/J beyond $1/N$ to the Josephson regime introduces an approximately quadratic part to the spectrum for energies $E \gtrsim 2NJ$, for which

$$E_i \simeq NJ + \frac{U}{4}i^2. \tag{3.8}$$

In the Fock regime only quasi-degenerate pairs of states remain, forming an approximately quadratic spectrum. It was shown in Ref. [Salg07] that the splitting between these quasi-degenerate states vanishes with $1/N!$.
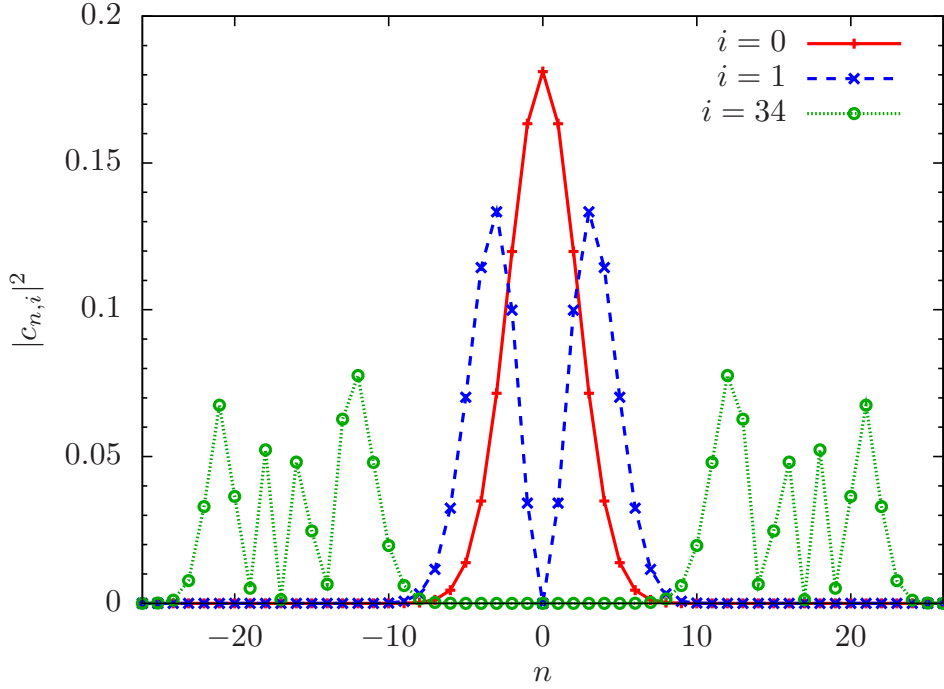
FIGURE 3.4: Distribution of the relative particle number $n = (n_1 - n_2)/2$ in three different eigenstates of the Hamiltonian in the Josephson regime, $U/J = 1$, for $N = 100$ particles. For the states with odd i, the coefficients are odd under $n \to -n$, and vice-versa for the even-i states.

3.3.1 Properties of the eigenstates

FIG. 3.4 shows the occupation number distribution $|c_{n,i}|^2$ of three different energy eigenstates $|E_i\rangle$ in the Fock basis $|n\rangle$ defined in Eq. (3.6),

$$|E_i\rangle = \sum_{n=-N/2}^{N/2} c_{n,i} |n\rangle. \tag{3.9}$$

The value of U/J is chosen such those states are in the Josephson regime.

We find that the coefficients of the ground state are well approximated by a Gaussian centered around $n = 0$, reflecting its semiclassical nature. The first exited state has a wider distribution around the same mean value. Since it must be an antisymmetric state, one has $c_{0,1} = 0$. The higher excited states show an increasingly wider distribution around $n = 0$ with an increasing number of "nodes" in $c_{n,i}$. In the end, the final energy states present a gap in the occupation of modes with nearly-equal particle number in each well, i.e. $n \sim 0$. Those states are quasi-degenerate with very similar symmetric
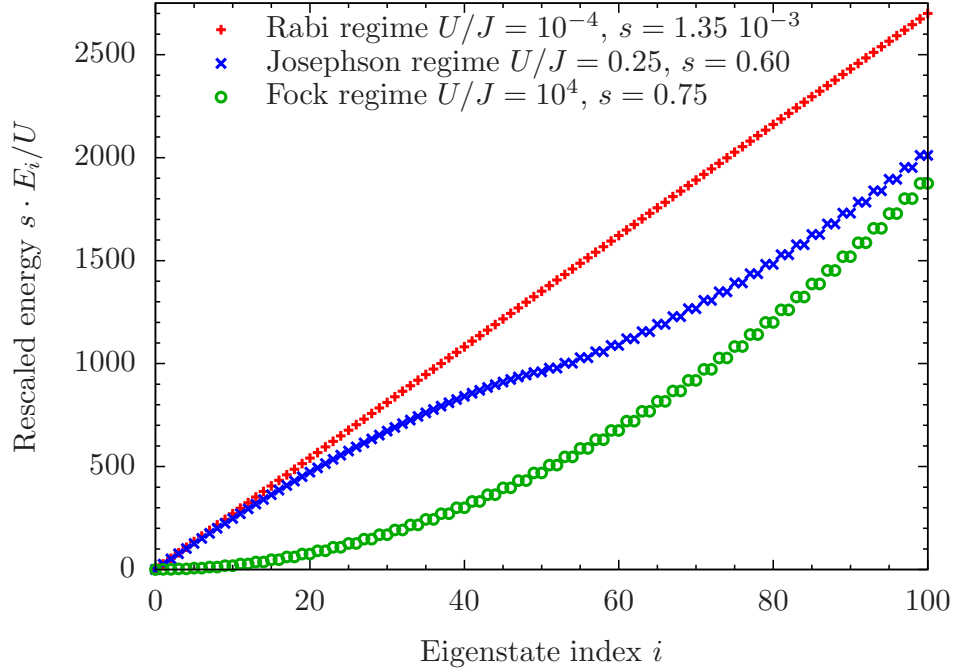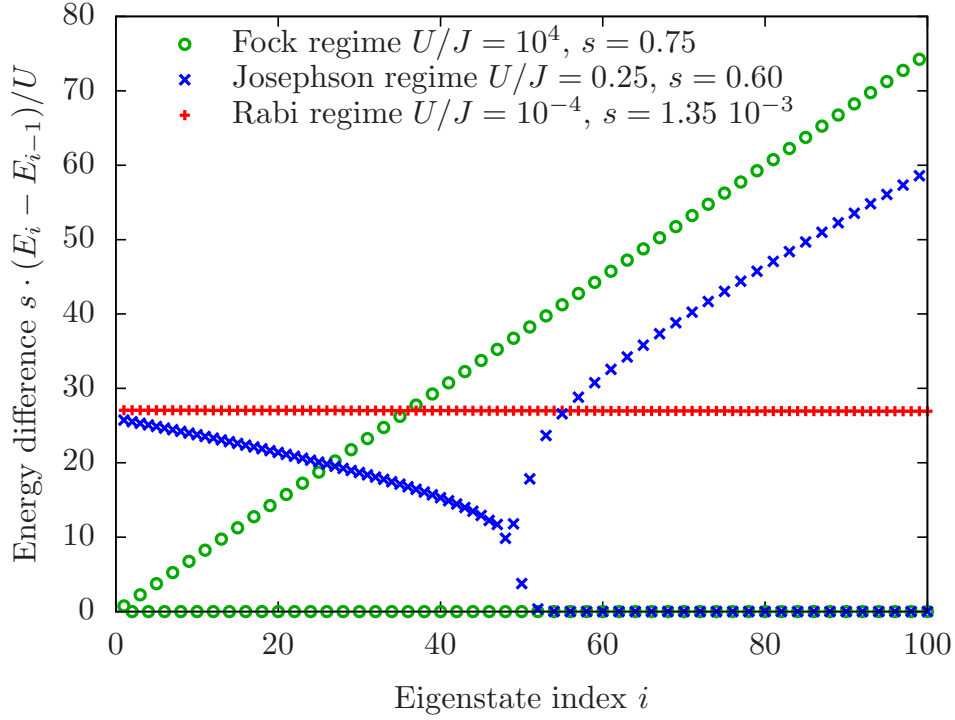
FIGURE 3.5: Energy differences of the spectrum of the Bose-Hubbard Hamiltonian in different regimes. The energies are given in units of U/s, with s a scale factor given in the legend.

and anti-symmetric distribution. Also, this gap means that those states are so-called cat states. Those are, for us, states where the system is in a superposition of a condensate predominantly in the left well and one in the right one, and not only the diametrically opposed state $(|0, N\rangle + |N, 0\rangle)/\sqrt{2}$.

In FIG. 3.5, we present the evolution of the eigenenergies with increasing eigenstate index i, i.e. we show the difference between the energy of an eigenstate and the one of the state before it, $E_i - E_{i-1}$. This is done in the three regimes for the same parameter U/J as in FIG. 3.3. In the Rabi regime, the energy difference is constant, as the spectrum is linear. In the Fock regime, the energy difference shows two branches. For odd i, it grows linearly, as the quadratic nature of the spectrum would suggest, while for even i, the values of the difference is nearly zero, as the pairs of states are quasi-degenerate. We mentioned that this degeneracy goes with $1/N!$, which means that the difference in energies is not distinguishable from zero in our calculation, due to the numerical noise. In the Josephson regime, those two behaviors mix together. First the spectrum grows without degeneracies, though the energy difference is not as constant as in the Rabi regime. Then its evolution splits into two branches, introducing the degeneracies and quadratic behavior of the later Fock regime.
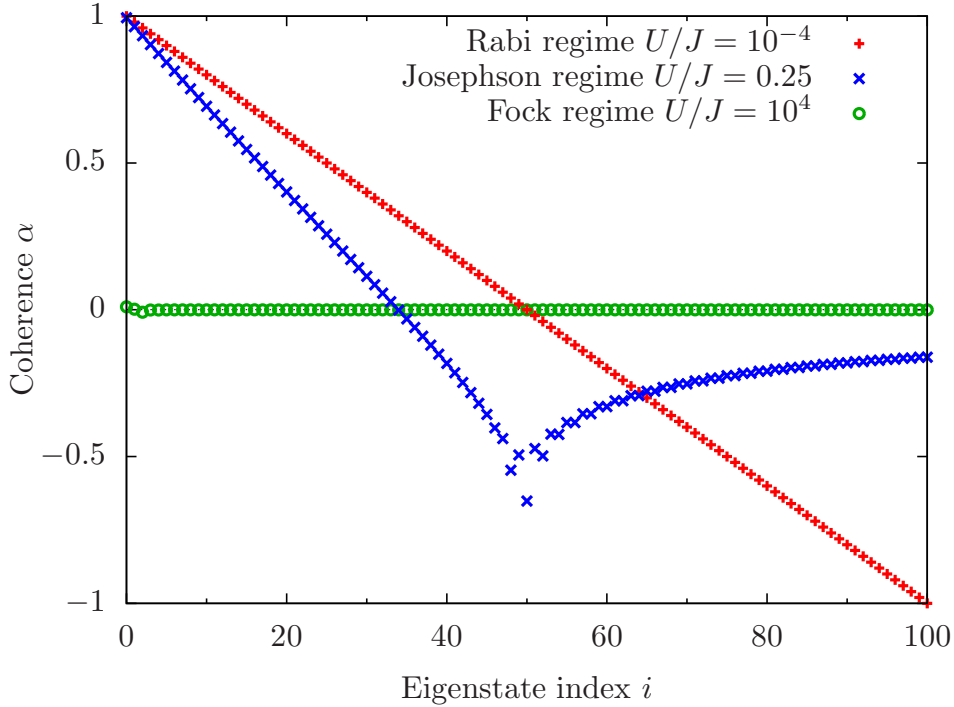
FIGURE 3.6: Coherence of the Bose-Hubbard Hamiltonian spectrum in different regimes.

In a second time, we conside the coherence of the condensate, which is measured by comparing the phases of the condensate present in each well. In terms of the operators $\hat{b}$ and $\hat{b}^\dagger$, the observable is defined as

$$\hat{\alpha} = \frac{1}{2N}(\hat{b}_2^\dagger \hat{b}_1 + \hat{b}_1^\dagger \hat{b}_2). \tag{3.10}$$

In FIG. 3.6, we present the expectation value of this observable $\alpha = \langle \hat{\alpha} \rangle$ for the eigenstates of the Hamiltonian. In the Rabi regime, this coherence starts very high, but the ground state exhibits $\alpha = 1$ only in the non-interacting case $U = 0$. Then, this values goes down linearly towards "anti-coherent" states $\alpha \approx -1$. In the Fock regime, the two wells are nearly decoupled and therefore coherence is low over the entire spectrum, though not exactly zero, especially for the first eigenstates. The Josephson regime is once more at the crossing of those two behaviors, starting at an high coherence and tending towards zero for high energies after a section with negative coherences.

The last observable we will discuss in this section is the variance of the particle number difference (3.6). Defined as

$$(\Delta \hat{n})^2 = \langle (\hat{n} - \langle \hat{n} \rangle)^2 \rangle, \tag{3.11}$$
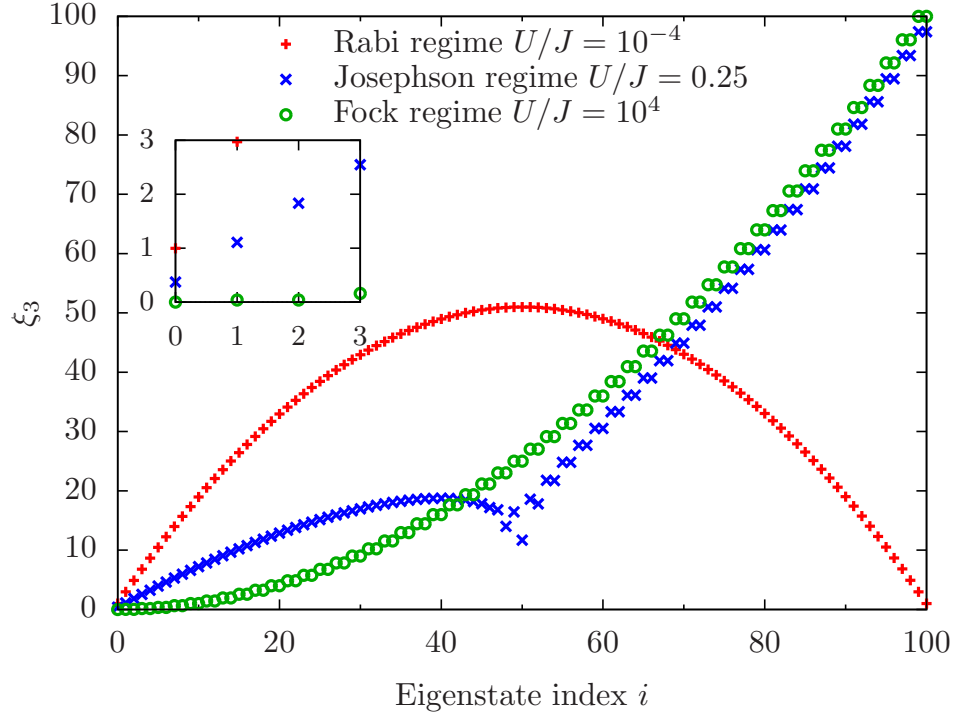
FIGURE 3.7: Variance of the particle number difference for the Bose-Hubbard Hamiltonian spectrum in different regimes.

its evolution is given in FIG. 3.7. However, we have chosen to express this variance in terms of the parameter ξ_3, defined as

$$\xi_3 = \frac{2}{N}(\Delta\hat{n}). \tag{3.12}$$

In the following, the fluctuations of particle number difference will be discussed in details using this parameter. Its name follows from the discussion in Sect. 3.4. In the Fock regime, the variance grows quadratically with i, but is exactly zero in the ground state only for the limit $U/J \to \infty$. As shown in the inset, in the Rabi regime, the variance start and ends around $\xi_3 \approx 1$, this value is called the classical limit. Its maximal value is around $N/2$. Again, those values are exact when $U/J = 0$. As it was the case for the previous observables, the Josephson regime is borrowing features from the other two.

3.3.2 Large interaction limit

In the Fock regime, $U/J > N$, all states are quasi twofold degenerate. In this regime, there is no longer any contribution near $n = 0$. A gap opens up in the distribution of

$|c_{n,i}|^2$. The size of this gap increases towards larger i. Note, however, that excitations of the double-well system up to $|E_{N+1}\rangle$, e.g., at higher temperatures, easily exceeds the validity of the single-band approximation.

In the limit $U/J \to \infty$, the number operator $\hat{n}$ commutes with the Hamiltonian, meaning that the energy eigenstates can be expressed easily in the Fock basis. The result depends on the parity of the total particle number N. If it is even, the ground state is non degenerate and writes as $|E_0\rangle = |N/2, N/2\rangle$. The following states are degenerate in pairs, and read as the cat states

$$|E_{2i-1}\rangle = \frac{1}{\sqrt{2}} \left(\left| \frac{N}{2} + i, \frac{N}{2} - i \right\rangle - \left| \frac{N}{2} - i, \frac{N}{2} + i \right\rangle \right), \tag{3.13a}$$

$$|E_{2i}\rangle = \frac{1}{\sqrt{2}} \left(\left| \frac{N}{2} + i, \frac{N}{2} - i \right\rangle + \left| \frac{N}{2} - i, \frac{N}{2} + i \right\rangle \right), \tag{3.13b}$$

where $i = 1, ..., N/2$. One easily sees how those states are the limit of the Fock regime eigenstates, with the two distributions in $|c_{n,i}|^2$ and separated by an increasing gap in i. Those two distributions tend towards the two "delta" functions present in Eq. (3.13), whose distance is also increasing with i.

In the case of an odd total number of particles, even the ground state is degenerate,

$$|E_{0,1}\rangle = \frac{1}{\sqrt{2}} \left(\left| \frac{N+1}{2}, \frac{N-1}{2} \right\rangle \pm \left| \frac{N-1}{2}, \frac{N+1}{2} \right\rangle \right). \tag{3.14}$$

The following states consists in a similar series of pairs of degenerate states with increasing imbalance. We will see in Section 4.2 that this dependence on the parity of the total particle number has an influence on the production of quantum statistical squeezing.

3.4   Angular-momentum representation

In this section, we will discuss another convenient representation of the Hamiltonian using Schwinger operators. They relate directly to the number and phase operators, and allow for an easier visualization of the system. Then, in this representation, we will review different measures of squeezing. Fundamental limits for the respective squeezing parameters are then derived from the Heisenberg uncertainty relations.

Since we are studying a two-site system, we can use the properties of the SU(2) symmetry group to visualize the relation between number and phase. It can be most conveniently seen on the Bloch sphere. To that end, we express the Hamiltonian in

terms of the Schwinger operators [Schw65], defined as

$$\hat{S}_k = \frac{1}{2} \sum_{i,j=1}^{2} \hat{a}_i^\dagger \sigma_{ij}^k \hat{a}_j, \quad k = 1, 2, 3, \tag{3.15}$$

where σ^k is the Pauli k-matrix.

$$\sigma^1 = \begin{pmatrix} 1 & 0 \\ 0 & 1 \end{pmatrix}, \quad \sigma^2 = \begin{pmatrix} 0 & -i \\ i & 0 \end{pmatrix} \text{ and } \quad \sigma^3 = \begin{pmatrix} 1 & 0 \\ 0 & -1 \end{pmatrix}. \tag{3.16}$$

The corresponding angular-momentum-type states of the system can be represented by quantum phase-space (Wigner) distributions on the Bloch sphere, see for example Refs. [Dowl94, Barn97]. Appendix A presents more details about this representation.

In our system with fixed total particle number N, the total spin $S = |\hat{\mathbf{S}}|$ is also fixed and is worth $S = N/2$. This means that our spin representation will stay on the surface of a Bloch sphere of radius $N/2$. The first two operators, that relate to the phase difference between the two wells, are

$$\hat{S}_1 = \frac{1}{2}(\hat{b}_2^\dagger \hat{b}_1 + \hat{b}_1^\dagger \hat{b}_2), \tag{3.17a}$$

$$\hat{S}_2 = \frac{i}{2}(\hat{b}_2^\dagger \hat{b}_1 - \hat{b}_1^\dagger \hat{b}_2). \tag{3.17b}$$

Those orthogonal components relate, on the Bloch sphere, to the projection on the x–y equatorial plane. Classically, it means that they relate, up to a normalization of $N/2$, to the cosine and sine of the angle between the phase in each well. The absolute phase is undefined as we assume a fixed total particle number. Physically this phase is not measurable without comparing and therefore coupling the system to another system.

Also, one sees that the third operator

$$\hat{S}_3 = \frac{1}{2}(\hat{b}_1^\dagger \hat{b}_1 - \hat{b}_2^\dagger \hat{b}_2) = \hat{n} \tag{3.17c}$$

is simply the particle number difference. Therefore, in this representation, the Fock states can be written as angular momentum states $|S, S_3\rangle$ with $S = N/2$ and $S_3 = n$.

As a consequence of the commutation relations (2.11), the operators $\hat{S}_i$ form the fundamental representation of the angular momentum algebra,

$$[\hat{S}_k, \hat{S}_l] = i\varepsilon_{klm}\hat{S}_m, \tag{3.18}$$

with ε_{klm} being the total antisymmetric tensor of rank 3. They give rise to a set of uncertainties relations that determine lower bounds for the fluctuations of the observables,

$$(\Delta S_k)^2 (\Delta S_l)^2 \geq \frac{1}{4}|\epsilon_{klm}\langle \hat{S}_m \rangle|^2, \tag{3.19}$$

$$(\Delta S_k)^2 = \langle (\hat{S}_k - \langle \hat{S}_k \rangle)^2 \rangle. \tag{3.20}$$

Those relations will allow us to derive fundamental limits for squeezing, as we will show in the next section

The Hamiltonian (2.14) in this representation can be written in terms of the Schwinger angular momentum operators and reads

$$\hat{H} = -J(\hat{S}_+ + \hat{S}_-) + U(\hat{S}_3^2 + \hat{\mathbf{S}}^2 - N), \tag{3.21}$$

where we have defined

$$\hat{S}_\pm = \hat{S}_1 \pm i\hat{S}_2 \tag{3.22}$$

and the total spin squared

$$\hat{\mathbf{S}}^2 = \sum_{i=1}^{3} \hat{S}_i^2 \tag{3.23}$$

is, in our case of fixed total particle number N, given by $S(S-1) = N(N-1)/4$. The model (3.21) has also been investigated in much detail in nuclear theory [Lipk65, Mesh65, Glic65], solid-state physics [Gara98], and in the context of entanglement measures, see [Orús08] and the references cited therein.

3.4.1   Number-squeezing

To quantify angular momentum squeezing, one introduces a squeezing parameter adapted to the problem under consideration. In our case, a suitable definition of such a parameter relates the variance of one Cartesian component to the total spin $S = N/2$, i.e., to the total number of mode excitations or particles. Hence, we define

$$\xi_i = \frac{(\Delta S_i)^2}{S/2}. \tag{3.24}$$

For the third component $i = 3$, this is equivalent to the ratio of the variance of the number difference n to the total number,

$$\xi_3 = \frac{(\Delta n)^2}{N/4}. \tag{3.25}$$

In the following chapter, we will discuss the evolution of this squeezing parameter under the slow ramp-up of the potential barrier. It essentially reflects the suppression of the relative number fluctuations below the classical limit $(\Delta n)^2 = N/4$, or $\xi_3 = 1$, as given by the central-limit theorem, see (3.26).

As mentioned above, we consider only situations where the total number N of atoms in the wells and therefore the total spin S are fixed. However, before proceeding with this, we briefly remark that in the general case of varying S the squeezing parameters ξ_i measure the deviation from an angular momentum coherent state which is represented, in Bloch space, as a spherical Gaussian uncertainty distribution around $\langle \mathbf{S} \rangle$ with radial width $\sigma = \sqrt{N}/2$. Such a state can be written as a product of coherent states in the two modes 1 and 2, $|\alpha\rangle|\alpha\rangle$, where the occupation in both wells is $|\alpha| = \sqrt{N/2}$. That state has equal fluctuation in all direction, meaning

$$\xi_1 = \xi_2 = \xi_3 = 1. \tag{3.26}$$

In analogy to spin-squeezed states, two-mode states can exhibit squeezing in particular directions at the expense of increased fluctuations in directions perpendicular to this [Wine94]. Back in the case of fixed S, meaning that we limit ourselves to the surface of the Bloch sphere, an eigenstate of $\hat{S}_3$, for example, can be illustrated by a circle parallel to the equator of the sphere, i.e. the 1-2-plane. In that case, the variances are given by

$$(\Delta S_1)^2 = (\Delta S_2)^2 = \frac{1}{2}[S(S+1) - S_3^2], \tag{3.27}$$

and of course $(\Delta S_3)^2 = 0$, as we discuss its eigenstates.

The operators $\hat{S}_1$ and $\hat{S}_2$ measure the phase between the Fock modes 1 and 2 which is accessible to interference measurements of the particle occupation numbers, see Ref. [Estè08]. Hence, the commutators (3.18) characterize the uncertainty relation (3.19) between relative number and cosine of the relative phase.

The potential we consider is symmetric and, in general, each well has an equal average population. Hence, the two-mode states considered in the following, with relative particle number centered around $n = 0$. That corresponds to a distribution on the surface of the Bloch sphere, centered around the equator, i.e., around a polar angle $\theta = \pi/2$ or $\langle \hat{S}_3 \rangle = 0$. We take the state to be symmetric with respect to an exchange of the two sites. It means that the second spin operator vanishes on average, i.e. $\langle \hat{S}_2 \rangle = 0$.

A more convenient parameter to reflect the squeezing below the standard quantum limit, in accordance with the uncertainty relation (3.19) is given by

$$\xi_{kl} = \frac{(\Delta S_k)^2}{|\langle \hat{S}_l \rangle / 2|}. \tag{3.28}$$

As we consider the special case $\langle \hat{S}_2 \rangle = \langle \hat{S}_3 \rangle = 0$, the only nontrivial combinations are ξ_{21} and ξ_{31}. The variances $(\Delta S_k)^2$ are subject to the uncertainty relation (3.19) such that the relevant parameters ξ_{kl} obey the inequality

$$\xi_{21}\xi_{31} \geq 1. \tag{3.29}$$

This defines the Heisenberg limit for the fluctuations.

One might think at first glance that the limit $\xi_{31} \to 0$ is allowed at the expense of $\xi_{21} \to \infty$ and vice versa. However, as long as $|\langle \hat{S}_1 \rangle| > 0$ perfect squeezing in either the relative number or the phase is not possible as we have assumed fixed S and thus a fixed Bloch-sphere radius.

3.4.2 Determination of the Heisenberg limits

In order to determine the actual squeezing limit for a fixed total number, one could take the general upper limit $(\Delta S_2)^2 \leq S^2 = N^2/4$ given by the radius of the Bloch sphere and infer, from the uncertainty relation (3.19) for the variances of the angular momenta, the lower limit

$$(\Delta S_3)^2 \geq \langle \hat{S}_1 \rangle^2 / N^2. \tag{3.30}$$

This limit vanishes at $\langle \hat{S}_1 \rangle = 0$ and becomes as large as $1/4$ for $\langle \hat{S}_1 \rangle = N/2$. However, as we will show in a minute, this approximation, while valid, is too rough and a better inequality must be found.

Since the variance of S_2 depends nontrivially on the mean value of S_1 it is rather necessary to take into account the constraint given by the fixed total particle number $N = 2S$. Using

$$
\begin{aligned}
\langle \hat{\mathbf{S}}^2 \rangle = S(S+1) &= \langle \hat{S}_1^2 \rangle + \langle \hat{S}_2^2 \rangle + \langle \hat{S}_3^2 \rangle \\
&= \langle \hat{S}_1^2 \rangle + (\Delta S_2)^2 + (\Delta S_3)^2,
\end{aligned}
\tag{3.31}
$$

as $\langle \hat{S}_2 \rangle = \langle \hat{S}_3 \rangle = 0$, in the definition (3.28) of ξ_{21}, one finds

$$\xi_{21} = \frac{S(S+1) - \langle \hat{S}_1^2 \rangle}{|\langle \hat{S}_1 \rangle/2|} - \xi_{31}. \tag{3.32}$$

Inserting this in (3.29), one finds the inequality

$$\xi_{31}^2 - 2\xi_{31}\gamma + 1 \leq 0, \tag{3.33}$$

where we have defined

$$\gamma = \frac{S(S+1) - \langle \hat{S}_1^2 \rangle}{|\langle \hat{S}_1 \rangle|}. \tag{3.34}$$

This contains, besides the average, also the fluctuations of the "phase operator" $\hat{S}_1$. In general, as (3.33) is a quadratic inequality, it returns both a lower bound $\xi_{31,\min} \leq \xi_{31}$ and an upper bound $\xi_{31,\max} \geq \xi_{31}$ for ξ_{31}.

For the special case that $\langle \hat{S}_1 \rangle = S = N/2$, one has $\langle \hat{S}_1^2 \rangle = S^2$ such that the inequality (3.33) becomes an equation fixing the variance to the unique value

$$(\Delta S_3)^2 = \frac{N}{4} \tag{3.35}$$

which is both a lower and an upper bound. Note that this bound is enhanced by a factor N as compared to the naive limit (3.30) derived from the uncertainty relations above.

To continue the discussion in the general case $\langle \hat{S}_1 \rangle \leq N/2$, one sees that

$$\langle \hat{S}_1^2 \rangle \geq \langle \hat{S}_1 \rangle^2, \tag{3.36}$$

and the minimum $\langle \hat{S}_1^2 \rangle = \langle \hat{S}_1 \rangle^2$ is realized, for any $\langle \hat{S}_1 \rangle$, by the eigenstates of $\hat{S}_1$. Hence, one can replace $\langle \hat{S}_1^2 \rangle$ by $\langle \hat{S}_1 \rangle^2$ in (3.34),

$$\gamma = \frac{S(S+1)}{|\langle \hat{S}_1 \rangle|} - |\langle \hat{S}_1 \rangle|. \tag{3.37}$$

Since $|\langle \hat{S}_1 \rangle| \leq 1$, one has that $\gamma \geq 1$. Therefore, the inequality (3.33) possesses two roots and defines both the lower and upper bounds to ξ_{31} for any given value of the average $\langle \hat{S}_1 \rangle$,

$$\gamma - \sqrt{\gamma^2 - 1} \leq \xi_{31} \leq \gamma + \sqrt{\gamma^2 - 1}. \tag{3.38}$$

Using the definition (3.28), the limits for $(\Delta S_3)^2$ is then

$$\tilde{\gamma} - \sqrt{\tilde{\gamma}^2 - \frac{\langle \hat{S}_1 \rangle^2}{4}} \leq (\Delta S_3)^2 \leq \tilde{\gamma} + \sqrt{\tilde{\gamma}^2 - \frac{\langle \hat{S}_1 \rangle^2}{4}}, \tag{3.39}$$

where we have defined

$$\tilde{\gamma} = \frac{|\langle \hat{S}_1 \rangle|}{2} \gamma = \frac{S(S+1) - \langle \hat{S}_1 \rangle^2}{2}. \tag{3.40}$$

In FIG. 3.8, we show the resulting bounds on

$$\xi_3 = \frac{4}{N}(\Delta n)^2 = \frac{4}{N}(\Delta S_3)^2 = \frac{2}{N} \xi_{31} |\langle \hat{S}_1 \rangle| \tag{3.41}$$

as functions of the coherence

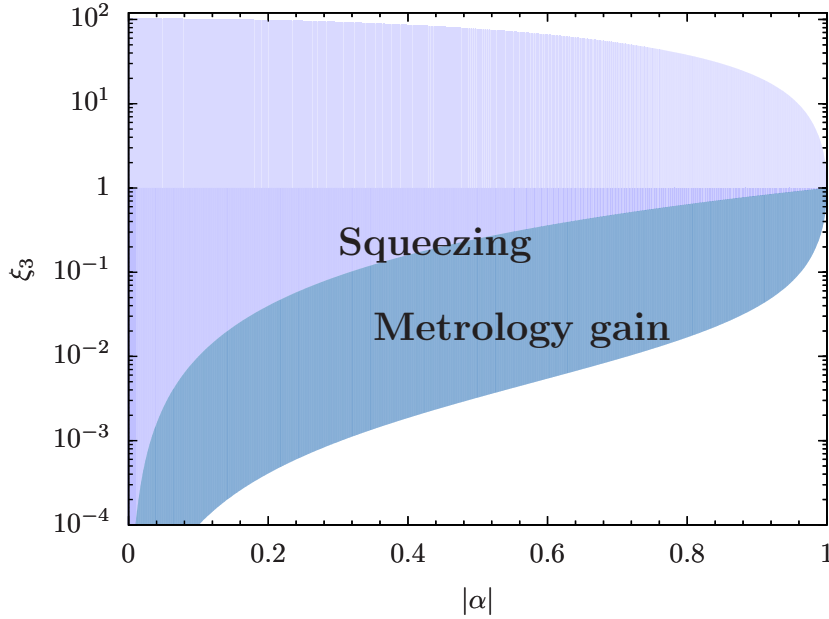$$\alpha = \frac{4}{N} \langle \hat{S}_1 \rangle. \tag{3.42}$$

FIGURE 3.8:   Phase diagram for $N = 100$ particles in a double-well potential, with on the average equal populations in the two wells, $\langle \hat{n} \rangle = \langle \hat{n}_1 - \hat{n}_2 \rangle / 2 = 0$, and the absolute phase chosen such that $\langle \hat{S}_2 \rangle = i \langle \hat{a}_2^\dagger \hat{a}_1 - \hat{a}_1^\dagger \hat{a}_2 \rangle = 0$, see Eq. (3.15). For any given coherence parameter $\alpha = 2\langle \hat{S}_1 \rangle / N$ the variance $(\Delta n)^2 = N\xi_3/4$ of the number difference between the wells is bounded below and above by Heisenberg's uncertainty relation and the constraint that the total particle number N is fixed. The allowed area is defined by the inequality (3.33) shaded in colors in the above diagram. In the medium (violet) and dark (blue) shaded regimes, the squeezing parameter is below the standard quantum limit, $\xi_3 \leq 1$, see Eq. (3.25). In the dark (blue) regime, the squeezing can be used to gain precision in metrology, see Eq. (3.44).

The shaded areas are allowed by the inequality (3.33). In the medium (violet) and dark (blue) shaded areas the system is below the standard quantum limit, $\xi_3 \leq 1$, see Eq. (3.25).

For $|\langle \hat{S}_1 \rangle| \to 0$, one finds a lower bound, to quadratic approximation in $\langle \hat{S}_1 \rangle$, of[1]

$$(\Delta S_3)^2 \geq \frac{\langle \hat{S}_1 \rangle^2}{4S(S+1)}, \tag{3.43}$$

This limit is by a factor of $S/(S+1)$ lower than the naive bound (3.30), a difference which only disappears in the limit of large particle numbers.

---

[1]This inequality was also found in Ref. [Søre01b], where Eq. (3), taking into account that the square-bracketed term under the root needs to be squared, gives our bound in the limit of small $\langle J_z \rangle = \langle \hat{S}_1 \rangle$, see arXiv: quant-ph/0011035v2.
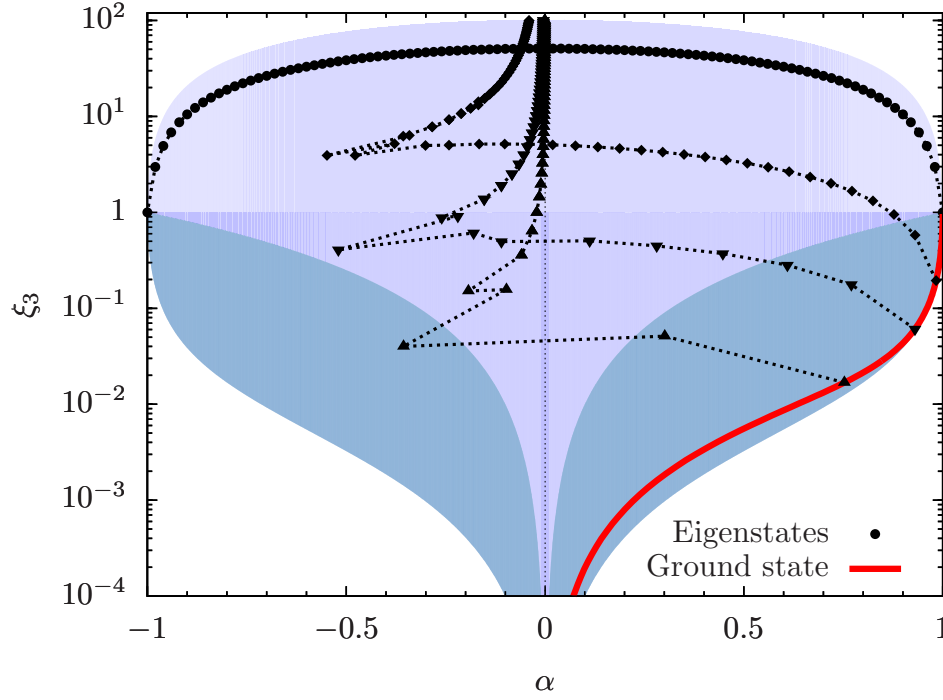
FIGURE 3.9: Positions of the energy eigenstates of the Hamiltonian (3.21) for a system with $N = 100$ particles in the phase diagram introduced in FIG. 3.8. Each black dot corresponds to one such state. The dotted lines are drawn to guide the eye between successive eigenstates of a Hamiltonian with fixed ratio U/J. From top to bottom, the sets of states are obtained for $U/J = 0, 1, 10$, and 100, respectively. The (red) solid line connects all ground states for different U/J. We emphasize that the energy eigenstates do not extend over the full (shaded) region allowed by Heisenberg's uncertainty.

The angular momentum representation (3.21) of the Hamiltonian shows that, for a given set of parameters U and J, each of the energy eigenstates corresponds to a point in the $|\langle \hat{S}_1 \rangle|$-$(\Delta S_3)^2$ plane. In FIG. 3.9 we show these points for $J = 1$ Hz and four different values of U (black dots). Those values are, from top to bottom, $U/J = 0, 1, 10$, and 100. The dotted lines serve to guide the eye between the values for subsequent states of the same Hamiltonian. This figure can be seen as a parametric plotting of FIG. 3.6 and FIG. 3.7, but the values of U/J are not the same.

This shows that states with lower energies have larger $|\langle \hat{S}_1 \rangle|$ and smaller $(\Delta S_3)^2$ than states with higher energy. We find that the ground-state values are in accordance with the limit set by the Heisenberg uncertainty relation (3.33) but correspond with this limit only for coherences $\alpha = 0$ and $\alpha = 1$. Similarly, the eigenstates with the highest energies, do not give the highest possible number fluctuations $(\Delta S_3)^2$. The only

exception are the cases $\langle \hat{S}_1 \rangle = \pm S$, i.e., $U = 0$, where the lower and upper Heisenberg limits meet at $\xi_3 = 1$, and the case $\langle \hat{S}_1 \rangle = 0$. Hence, the diagram in FIG. 3.9 shows that adiabatic changes of the parameters cannot drive the system, starting in some classical (diagonal) mixture of energy eigenstates, into the maximally squeezed state, for any value of the coherence α other than 0 or ± 1. It means that maximum squeezing allowed by Heisenberg's uncertainty relation is only possible in a non-equilibrium procedure.

3.4.3   Metrology gain

Spin-squeezed states with large total angular momentum quantum number S have been suggested as means for increasing the precision of interferometric and metrology measurements beyond the standard quantum limit [Wine92, Kita93, Wine94, Boll96]. One can, e.g., use the squeezing of the uncertainty ellipsoid around the mean spin vector $\langle \hat{\mathbf{S}} \rangle$. If the ellipsoid is squeezed perpendicular to the spin direction along a direction $\boldsymbol{\sigma}$ this increases the measurement sensitivity of an angle θ of rotation of $\langle \hat{\mathbf{S}} \rangle$ about an axis $\boldsymbol{\rho}$ perpendicular to the spin and the squeezing direction, $\langle \hat{\mathbf{S}} \rangle \cdot \boldsymbol{\rho} = \boldsymbol{\sigma} \cdot \boldsymbol{\rho} = 0$. The resolution of the angle θ is proportional to the variance $(\Delta \mathbf{S}_{\boldsymbol{\sigma}})^2$ of the spin vector along the squeezing direction $\boldsymbol{\sigma}$, $\Delta \theta = (\Delta \mathbf{S}_{\boldsymbol{\sigma}})^2 / |\langle \hat{\mathbf{S}} \rangle|$. This needs to be compared to the angular noise in the angular momentum coherent states, $1/\sqrt{N} = 1/\sqrt{2S}$. Hence, the squeezing parameter measuring the sensitivity of the squeezed states considered before ($\langle \hat{S}_2 \rangle = \langle \hat{S}_3 \rangle = 0$) under rotations around the 2-axis reads

$$\xi_R^2 = \frac{N(\Delta S_3)^2}{\langle S_1 \rangle^2 + \langle S_2 \rangle^2}. \tag{3.44}$$

The area allowed by $\xi_R \leq 1$ is indicated in FIG. 3.8 by dark shading.

In summary, the fluctuations of the spin in one direction have to be reduced below shot noise ($(\Delta S_3)^2 < S/2$), and the spin polarization in the orthogonal plane, $\langle S_1 \rangle^2 + \langle S_2 \rangle^2$, has to be large enough to maintain the sensitivity of the interferometer. The precision of such a quantum-enhanced measurement is $\xi_R / \sqrt{N}$ [Søre01a], whereas the standard quantum limit set by shot noise is $1/\sqrt{N}$.

3.5   Summary

In this chapter, we discussed some of the relevant properties of the two-mode Bose-Hubbard Hamiltonian. In particular, we discussed the three regimes of the Hamiltonian. We also introduced the angular-momentum representation of the system, making an analogy with a spin $1/2$ system. In that picture, we discussed which areas of the phase space of the system was connected to spin–squeezed states. A yet smaller area allows for

metrology gain in interferometry experiments. We have shown that the eigenstates of the Hamiltonian do not exploit the full region of possible squeezing allowed by Heisenberg's uncertainty relation for number and phase fluctuations.

In the next chapter, we will see how it is possible to dynamically produce squeezed states by going, in a finite ramp-up, from the Rabi to the Fock regime. We will theoretical describe the dynamics of the experiment discussed in Ref. [Estè08]. The quantum evolution will be explained by changes in the spectrum of the Hamiltonian for various U/J, using properties discussed here. Then, those results are compared to the ones resulting from a semi-classical evolution. Finally, we will discuss quantum statistical effects in the evolution of the system outside of the range of the parameters available for the experiment in Ref. [Estè08].

Chapter 4

Dynamics in the double-well

In this chapter, we describe the dynamical production of squeezing squeezed states by providing a theoretical description the dynamics of the experiment discussed in Ref. [Estè08]. Later on, we will discuss quantum statistical effects in the evolution of the system outside of the range of the parameters available for the experiment.

The change the barrier height between the two wells, as shown in FIG. 3.1, can be used to produced squeezing in many-body states. This squeezing occurs in the relative number difference of particles in the two wells. It is, in fact, a suppression of the fluctuations of that number. In the experiment described in [Estè08], such squeezing was observed in the distribution of atoms, by counting them after high-resolution imaging of the atom cloud in subsequent runs and by calculating the variance of the resulting count.

In each such run, a condensate was prepared in the potential (3.1) with a low barrier height allowing the atoms to be delocalized across the potential floor, see for e.g. the blue curve in FIG. 3.1[1]. Then, the potential barrier was slowly raised, allowing for an almost adiabatic adjustment of the system's state to the modified external conditions. As anticipated, the finally strong barrier was observed to suppress the fluctuations $(\Delta n)^2$ in the particle number difference below the estimated classical variance $(\Delta n)^2/4 \sim N = \langle n_1 + n_2 \rangle$. This suppression was interpreted [Estè08] as due to the squeezing that manifests itself theoretically in the approximate low-energy many-body eigenstates.

As we describe in more detail in the following, during the first stage, the near-adiabatic ramp-up of the barrier, the population of the varying energy states remains approximately constant. The change of parameters in the Hamiltonian during the ramp deforms the populated states, causing adiabatic cooling of the system and squeezing, i.e., reduced relative number fluctuations which reflect the localization of the particles

---

[1]The experiment was not only realized in a double well system, but their qualitative conclusion turned out to remain the same with a slightly higher number of sites.

in either of the wells. In a second stage when the populated levels successively become pairwise quasi-degenerate, isothermal evolution is observed during which the squeezing reaches saturation.

In Sect. 4.1, we describe the dynamics observed in the experiment [Estè08], and we characterize the common properties as well as the differences between quantum and classical statistical many-body evolution of the system. To this end, we study the dynamical evolution both by direct integration of the von Neumann equation as well as by simulation in terms of a classical field equation of motion derived from the classical Hamiltonian function corresponding to the operator (2.14).

In Sect. 4.2, we will pursue the same analysis for values of the temperature and of the barrier height U/J outside of the range discussed in Ref. [Estè08]. This will drive the system in a regime where the dynamics exhibits characteristics of non-classical evolution. We will also show that in this regime, the parity of the total number of particles plays a role in the final amount of squeezing.

4.1   Production of squeezed states

In this section, we concentrate on the description and understanding of the experiment [Estè08]. In that experiment, a Bose gas is prepared in a double well trap with a relatively shallow barrier. Then, this barrier is ramped-up with a slow but finite speed. The resulting reduction of the particle number difference below the metrology gain limit was of particular interest for the experimentalist. In this theoretical work, we concentrate on the description of the evolution using both quantum and classical simulations, and comparing the differences and the common points.

4.1.1   Quantum evolution

We consider a system whose dynamics is described by the Hamiltonian (3.5). At the initial time $t = t_0$ the gas is assumed to be evenly distributed among the two wells of the potential, such that $\langle \hat{S}_3(t_0) \rangle = 0$. Due to the symmetry of the Hamiltonian, this remains true at all times $t > t_0$. Its initial state is described by a canonical density matrix with a given temperature T_0, with the spectrum determined by diagonalizing the Hamiltonian (3.5) to obtain its eigenstates $|E_i\rangle$. The density matrix then reads

$$\hat{\rho}(t_0) = \frac{1}{Z} \sum_{i=0}^{N} \mathrm{e}^{-E_i(t_0)/k_B T_0} |E_i(t_0)\rangle \langle E_i(t_0)|, \tag{4.1}$$

where Z is the normalization,

$$Z = \sum_{i=0}^{N} \mathrm{e}^{-E_i(t_0)/k_B T_0}, \tag{4.2}$$

and k_B is the Boltzmann constant.

The time evolution of the Bose-Hubbard parameters $J(t)$ and $U(t)$ was calculated as a function of the barrier height $V_0(t)$ in Fig. 3.2. The evolution of those parameters at times $t > t_0$ is given by a linear ramp-up of the barrier $V_0(t) = V_0(t_0) + v_0(t - t_0)/t_{\max}$. Experimentally,the total ramp-up was $v_0/h = (2\pi)2570\,\mathrm{Hz}$. Fig. 3.1 shows the 1D potential for the two extreme values of V_0 discussed in this section. The initial parameters $J(t_0)$ and $U(t_0)$ are taken to be in the Rabi regime as discussed in Sect. 3.3. The evolution of U and J during the ramp up of the barrier is also shown in Fig. 3.2, with the time given in units of the duration of the ramp $t_{\max}$, and with $t_0 = 0$.

Decreasing in this way the tunneling parameter J and at the same time preserving or slightly increasing the local interactions U drives the system from the Rabi through the Josephson into the Fock regime, see Sect. 3.3. Starting with the initial state (4.1) we compute the time evolution of the system by integrating the von Neumann equation for the density matrix numerically, with the Hamiltonian (3.5) being time-dependent according to the variation of U/J. This method is less time-consuming than numerically extracting the evolution from the diagonalization of the Hamiltonian, since its time-dependence requires a rediagonalization at each time step.

Using this method, we study the evolution of the squeezing parameters described in Sect. 3.4.1, in particular of the number variance $(\Delta n)^2 = (\Delta S_3)^2$ and the coherence parameter or relative phase $\alpha = \langle \hat{S}_1 \rangle$. For the purpose of comparing with experimental data we fit the initial temperature T_0 such that the initial number variance and coherence fit the experimentally determined values.

Fig. 4.1 shows the evolution of a system of $N = 100$ atoms in the α-$(\Delta n)^2$ plane as a (blue) solid line, under a $t_{max} = 0.16\,\mathrm{s}$ ramp-up of $J(t)/U(t)$ as given in Fig. 3.2. The system starts in a state with $(\Delta n(t_0))^2 = 37.5$ and $\alpha(t_0) = 0.994$ which is obtained for an initial temperature $T_0 = 20\,\mathrm{nK}$. The (red) short-dashed line shows the corresponding evolution of $(\alpha(t),(\Delta n(t))^2)$ under an adiabatic change of the parameters U and J, i.e., for $v_0 \to 0$. The areas allowed by the constraint Heisenberg, squeezing, and metrology gain limits, respectively, are shaded differently as discussed in Chapter 3 and Fig. 3.8.

Comparing the different lines in Fig. 4.1, we find that the system starts in from a near-adiabatic evolution before crossing over to an isothermal evolution. The crossover occurs as soon as the initially occupied levels transfer from the linear to the quadratic part of the spectrum. Please refer to Fig. 3.3 for examples of that spectrum for different values of U/J.
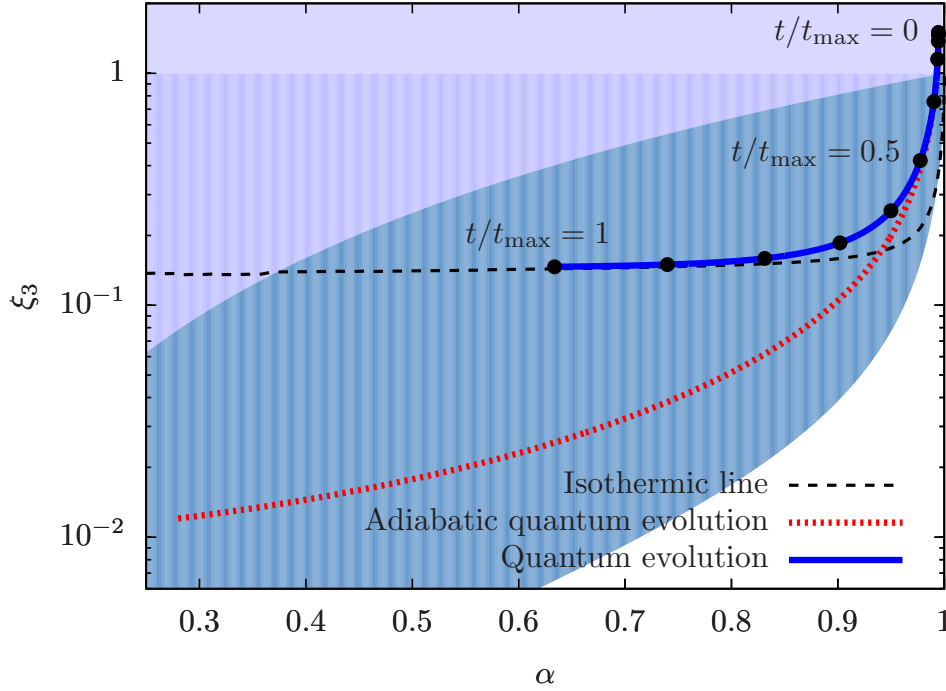
FIGURE 4.1:   (Color online) Evolution of the coherence α and the number variance $(\Delta n)^2$ for a gas of $N = 100$ atoms ((blue) solid line) under a slow ramp-up of $U(t)/J(t)$ over a time $t_{max} = 0.16\,$s as given in FIG. 3.2. The system starts in a state with $(\Delta n(t_0))^2 = 37.5$ and $\alpha(t_0) = 0.994$ which is obtained for an initial temperature $T_0 = 20\,$nK. A range of time points is indicated by black dots. They are spaced by $0.1\,t_{max}$ and the first completely distinct point is for $t = 0.3\,t_{max}$. The evolution under an adiabatic change of the parameters U and J, i.e., for $v_0 \to 0$ is shown by the (red) dotted line. An isotherm for $T = 0.17\,$nK is shown as a dashed line. See FIG. 3.8 and Sect. 3.4.1 for the definition of the differently shaded areas allowed by the constraint Heisenberg, squeezing, and metrology gain limits.

Let us discuss this crossover in more detail. To understand what happens, we consider the evolution of the density matrix in the energy eigenbasis. For an adiabatic evolution, this density matrix would stay constant. FIG. 4.2 shows the diagonal elements of the density matrix for 5 different times during the ramp-up of $U(t)/J(t)$ given in FIG. 3.2, on a semi-logarithmic scale. Those elements are calculated in the basis of the energy eigenstates (3.9) of the Hamiltonian (3.5), and are given by $\langle E_i | \hat{\rho}(t) | E_i \rangle$. FIG. 3.2 shows only the lowest energies E_i, $i = 1, \ldots, 50$. Note that the density matrix at times $t > 0$ is no longer diagonal as correlations have been formed. Nevertheless, the amplitudes of the off-diagonal elements are strongly reduced compared to the diagonal elements and the latter serve as a measure of the distributions of particles across the energy eigenstates.
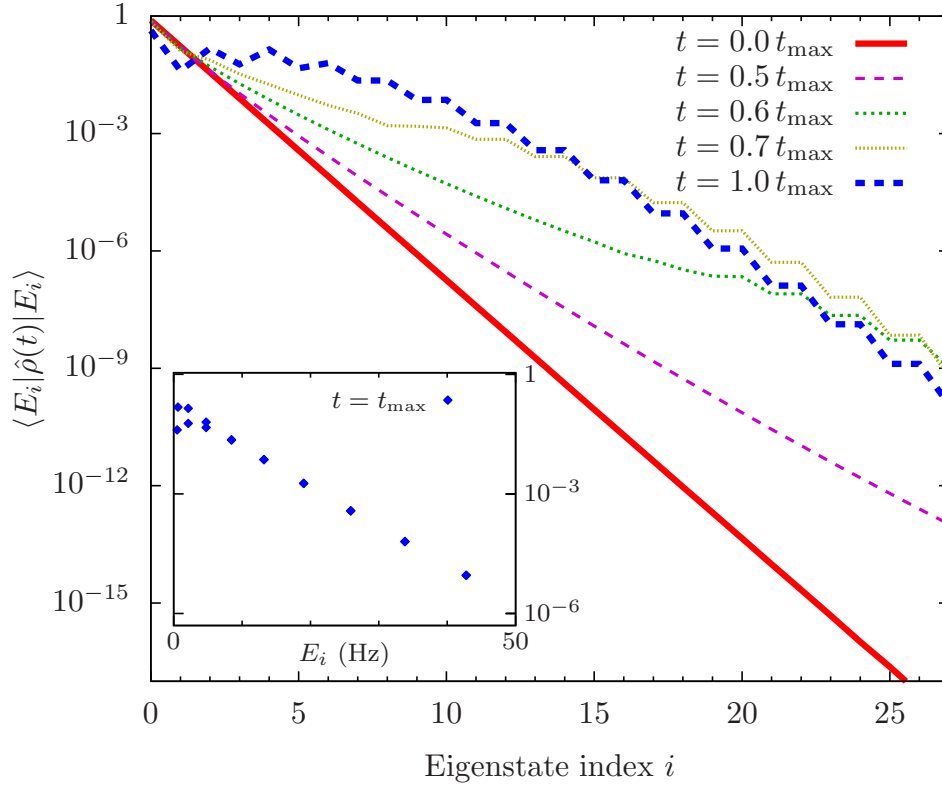
FIGURE 4.2: Diagonal elements of the density matrix, $\langle E_i|\hat{\rho}(t)|E_i\rangle$ in the basis of the energy eigenstates (3.9) of the Hamiltonian (3.5), for 5 different times during the ramp-up of $U(t)/J(t)$ shown in FIG. 3.2. Note the semi-logarithmic scale. The initial temperature is $T_0 = 20\,\text{nK}$. The inset shows the diagonal elements of the density matrix for $t = t_{max}$ as a function of the energy on a logarithmic scale, demonstrating the thermal character of the state.

The linear distribution at $t = 0$ corresponds to a density matrix with temperature $T_0 = 20\,\text{nK}$ (4.1). Since the spectrum is linear in the Rabi regime, see FIG. 3.3, the density matrix elements plot also linearly on a semi-logarithmic graph. Up until around $t = 0.5\ t_{max}$, the density matrix barely changes its character indicating a close-to-adiabatic evolution. However, as long as the occupied levels are linearly spaced in energy strong adiabatic cooling takes place. This can be seen in FIG. 3.3, by comparing the energy scaling s from the (red) "Rabi" to the (blue) "Josephson" spectrum. Hence, starting at the temperature $T_0 = 20\,\text{nK}$, after the initial near-adiabatic evolution the temperature arrives at the much lower final temperature assumed on the isotherm. The isotherm plotted in FIG. 4.1 corresponds to a temperature $T = 0.17\,\text{nK}$, therefore the adiabatic cooling is of a factor of 100.

Thereafter the system quickly leaves its near-adiabatic behavior to develop a stair-

case-like shape of the energy distribution. Around $t \simeq 0.5\ t_{max}$ the occupied levels enter the quadratic regime. In this regime, the energy spectrum develops two-fold quasi degeneracies, starting in the higher levels, corresponding to symmetric and antisymmetric states, see Sect. 3.3. There is no redistribution within the quasidegenerate pairs in the quadratic part of the spectrum as the symmetry of the Hamiltonian forbids transitions between states of different parity in the relative particle number n. However, the redistribution becomes possible between the pairs of states in the gradually changing spectrum because the levels at the boundary between the linear and quadratic parts of the spectrum approach each other closely. This is illustrated in the blue curve of FIG. 3.3, around $i \approx 50$.

For times $t \simeq 0.8\ t_{max}$, the energies of all but the largest occupied states belong to the quadratic regime. Note that at $t = t_{max}$ the occupation of the second lowest energy state, $i = 1$, is lower than the occupations of both the ground state $i = 0$ and second excited state $i = 2$. This is explained again from a symmetry argument. The initial state $\hat{\rho}(t_0)$ is dominated by the symmetric ground state with $c_{n,0} = c_{-n,0}$ and therefore the final state is predominantly symmetric, with a suppressed contribution from $|E_1\rangle$.

The redistribution of the initial single-energy eigenstates during the ramp would suggest that the final state is generically far from representing a thermal distribution. However, the spectrum of eigenenergies is no longer linear, the eigenstate index i is no longer a good abscissa for a plot. One needs to plot the the diagonal elements of the density matrix as a function of the energy on a semilogarithmic scale. This is shown in FIG. 4.2 for the final time $t = t_{max}$ in our simulations. The symmetric states are occupied according a thermal distribution, while the occupation of the odd-i levels remains suppressed. This suppression stabilizes the system against symmetry breaking to a self-trapped state with a non-zero mean value n. If the odd-i states would be equally strongly occupied, they could combine with the even states to yield self-trapping. In short, our results show, a thermal mixture of these initial eigenstates redistributes occupation numbers to yield a thermal state again at the endpoint of the ramp.

In summary, the system changes considerably during the entire ramp. During the initial evolution strong adiabatic cooling takes place. At the crossover to the isothermal evolution redistribution sets in and a "freeze out" of the fluctuations, fixing the system's temperature. During the following evolution period, the squeezing stays put while the mean coherence keeps decreasing.

4.1.2   Semiclassical description

To understand if quantum effects are responsible of the production of squeezed states discussed above, we will now turn to a semiclassical statistical description. To that end,

we start by taking a sample of the phase-space probability distribution corresponding to the initial quantum density matrix. This will be achieved by using Wigner representation, see App. A. Then, each realization is sampled independently using the classical equation of motion. At later times in the evolution, the correlation functions are obtained as moments over the independently propagated probability distribution. The semiclassical description of the dynamics of the two-mode Bose-Hubbard system has recently been studied in Refs. [Trim08, Trim09].

As discussed in Ref. [Ragh99], the classical dynamic equations are derived from the classical Hamiltonian function. This function is in turn obtained from the Hamiltonian in Eq. (3.21) by substituting the operators $\hat{S}_1 = \hat{S}_+ + \hat{S}_-$ and $\hat{S}_3$ by the classical variables,

$$\hat{S}_3 \to n, \tag{4.3a}$$

$$\hat{S}_1 \to \sqrt{S_1^2 + S_2^2} \cos \phi = \frac{N}{2} \sqrt{1 - \frac{4n^2}{N^2}} \cos \phi, \tag{4.3b}$$

and reads

$$H = U n^2 - JN \sqrt{1 - \frac{4n^2}{N^2}} \cos \phi. \tag{4.4}$$

One condition for the classical description to be valid is that the particle number in each well is much larger than one, i.e., $n \ll N$. The canonical variables are (half) the number difference n and the relative phase ϕ between the two wells.

From the above Hamiltonian the Josephson equations are obtained as

$$\frac{dn}{dt} = -NJ \sqrt{1 - \frac{4n^2}{N^2}} \sin \phi, \tag{4.5a}$$

$$\frac{d\phi}{dt} = 2Un - \frac{4n}{N} J \left(1 - \frac{4n^2}{N^2}\right)^{-1/2} \cos \phi. \tag{4.5b}$$

The expectation values of an observable $\mathcal{O}$ at a time $t > t_0$ are obtained as weighted average of the probability distribution

$$\langle \mathcal{O} \rangle = \mathcal{Z}^{-1} \int dn \, d\phi \, P(n, \phi; t) \, \mathcal{O}(n, \phi), \text{ with} \tag{4.6a}$$

$$\mathcal{Z} = \int dn \, d\phi \, P(n, \phi; t). \tag{4.6b}$$

The probability distribution P is then evolved using the classical path integral

$$P(n, \phi; t) = \int_{t_0}^{t} \mathcal{D}n \, \mathcal{D}\phi \, P(n, \phi; t_0)$$

$$\times \, \delta \left\{ \frac{\mathrm{d}\phi}{\mathrm{d}t} - 2Un - \frac{4n}{N}J \left(1 - \frac{4n^2}{N^2} \right)^{-1/2} \cos\phi \right\} \quad (4.7)$$

$$\times \, \delta \left\{ \frac{\mathrm{d}n}{\mathrm{d}t} + NJ\sqrt{1 - \frac{4n^2}{N^2}} \sin\phi \right\},$$

with the functional measures $\mathcal{D}n$ and $\mathcal{D}\phi$ defined as

$$\mathcal{D}n = \prod_{\tau=t_0}^{t} \mathrm{d}n(\tau), \quad (4.8a)$$

$$\mathcal{D}\phi = \prod_{\tau=t_0}^{t} \mathrm{d}\phi(\tau). \quad (4.8b)$$

The delta functionals evaluate the variables n and ϕ at each point in time according to the solution of the equations of motion, with initial values distributed according to $P(n, \phi; t_0)$. The probability distribution $P(n, \phi; t_0)$ at initial time is determined from the Wigner function corresponding to $\hat{\rho}(t_0)$, the semiclassical initial state, defined in Eq. (4.1), used in the quantum simulations in the previous section. See Appendix A for details.

4.1.3   Comparison of classical and quantum evolutions

In practice, the classical path integral (4.7) is solved numerically. The probability distribution is sampled from the Wigner function (A.7). One then gets a ensemble of points in the n–ϕ plane, (n_i, ϕ_i). Then each of those pairs are independently evolved in time using (4.5). Finally, observables are calculated using (4.6).

FIG. 4.3 shows the semiclassical evolution of a system of $N = 100$ atoms in the previously introduced α–$(\Delta n)^2$ plane as a (purple) dotted line, under the ramp-up of $J(t)/U(t)$ given in FIG. 3.2. The initial classical distribution was calculated from the density matrix (4.1) for an initial temperature $T_0 = 20\,\mathrm{nK}$. The (blue) solid line shows the corresponding quantum evolution as discussed in Sect. 4.1.1 and FIG. 4.1 for the same parameters $U(t)$ and $J(t)$, the same initial temperature T and the same evolution time $t_{\max}$.

As one can see in the figure, the semiclassical and the quantum evolutions are nearly identical. This indicates that dynamics of the production of squeezing is essentially a
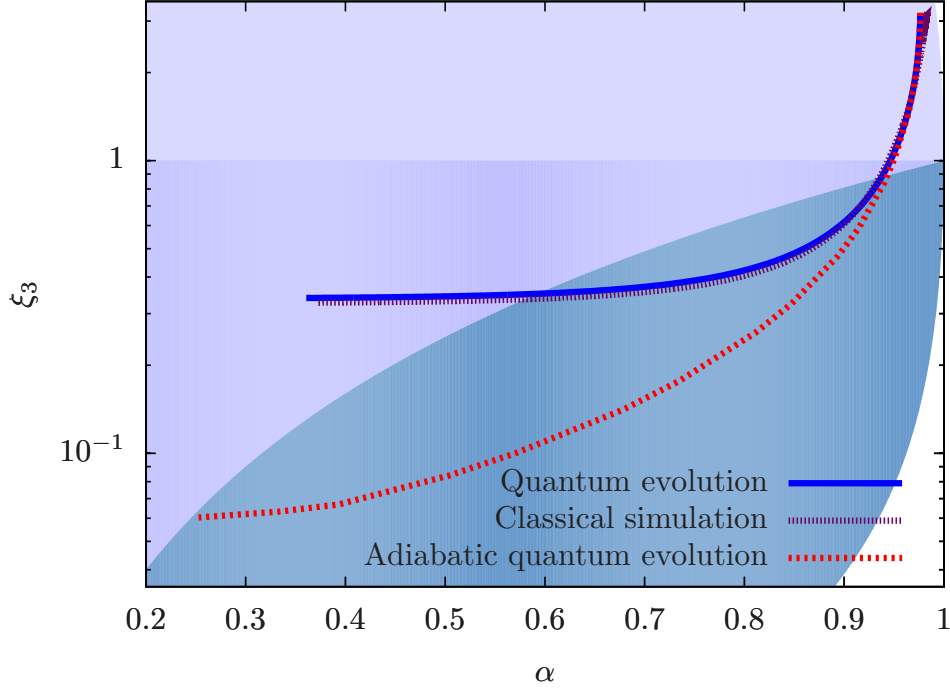
FIGURE 4.3: Semiclassical evolution ((purple) dotted line) of the coherence α and the number variance $(\Delta n)^2 = N\xi_3/4$ for a gas of $N = 100$ atoms under a slow ramp-up ($t_{max} = 0.16\,\text{s}$) of $U(t)/J(t)$ as given in FIG. 3.2. The (blue) solid line shows the corresponding quantum evolution, as discussed in Sect. 4.1.1 and FIG. 4.1 for the same evolution time t_{max} and the same time dependent parameters U and J. The initial temperature is $20\,\text{nK}$ as in FIG. 4.1. The definition of the shadings was introduced in FIG. 3.8.

classical process. Nonetheless, the precise shape of the initial probability distribution as derived from the Wigner function corresponding to the state (4.1) plays a role as is shown in more detail in FIG. 4.4.

There, we plot, for the same parameters as in FIG. 4.3, the difference between the ξ_3 obtained from the semiclassical and the quantum evolutions, normalized to the quantum result, for three different kind of initial phase-space distributions:

- An ellipsoidal Gaussian distribution with main-axes widths given by the number and phase distributions derived from the state (4.1) (blue dashed line),

- a product of the distributions of initial relative number and coherence derived from Eq. (4.1) (red dotted line), and

- a distribution as given by the full Wigner function for the state (4.1) (purple solid line).
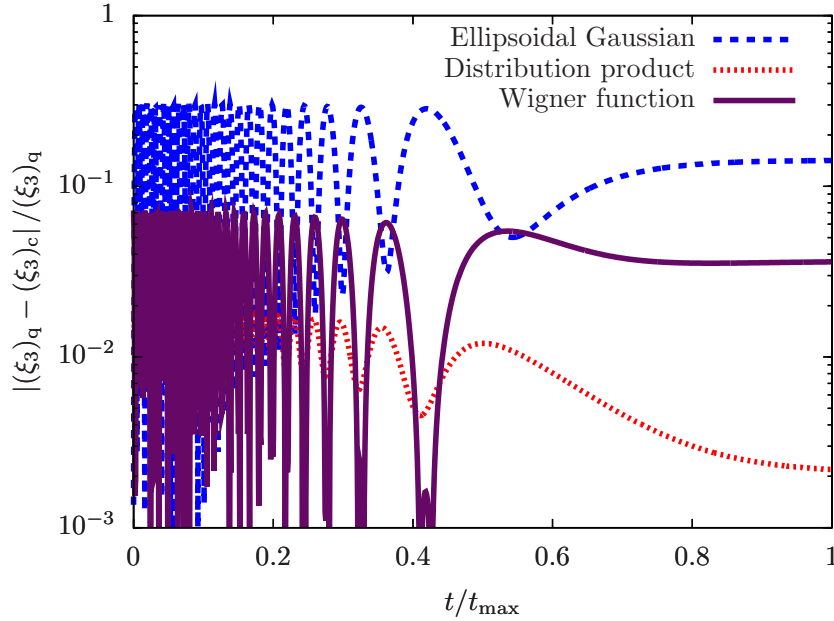
FIGURE 4.4: Difference between the ξ_3 obtained from the semiclassical and the quantum evolutions, normalized to the quantum result, for three different initial phase-space distributions: Purple solid line: Wigner function for the state (4.1). Red dotted line: Product of distributions of initial relative number and coherence derived from Eq. (4.1). Blue dashed line: Ellipsoidal Gaussian state with widths given by these relative number and coherence distributions. See the main text for a discussion.

The frequency of the oscillations is approximately given by the plasma frequency (3.7) in the classical potential (4.4) and decreases with increasing U/J. We find that the solution derived from the Wigner function shows smaller oscillatory deviations from the exact result than that derived from the Gaussian distribution. The classical simulations starting from the distribution product give an even smaller deviation. While the distribution product gives the least deviations during the evolution, the initial-time value of ξ_3 derived from the Wigner function is closest to the exact result. We believe that the remaining deviation is due to the discrete sampling of the Wigner function. Finally, the oscillations take place only during the initial near-adiabatic decrease of ξ_3, see FIG. 4.1, such that they remain mostly invisible in the comparisons shown in FIG. 4.3.

The fact that the variance of the Gaussian distribution oscillates stronger indicates that the initial Wigner function, though almost entirely positive and therefore classical-like, contains information about non-Gaussian correlations in the initial state. In particular, at lower temperatures also quantum effects are expected to play a more important role. This will show up in the negativity of the Wigner function, as we will discuss in
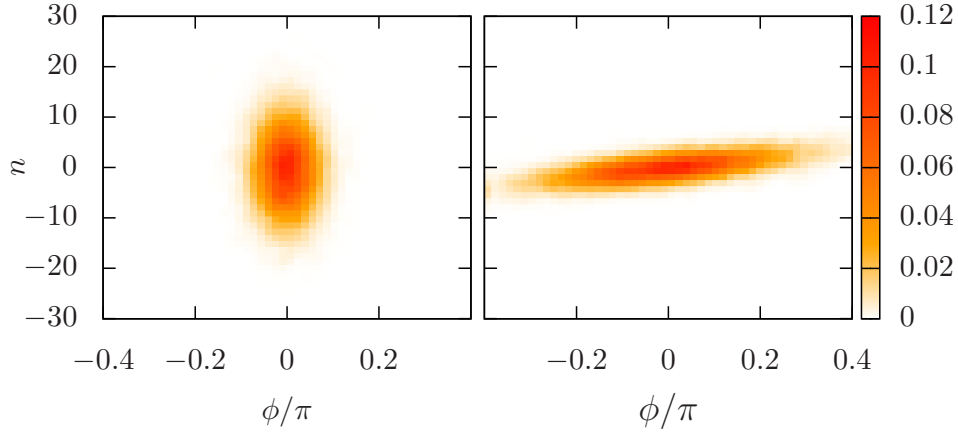
FIGURE 4.5:   Evolution of the phase-space probability distribution $P(n, \phi; t)$, Eq. (4.7), between $t = 0$ (left panel) and $t = 0.68\, t_{max}$ (right panel) as obtained by classical simulations according to Eq. (4.7). White color indicates $P(n, \phi; t) \approx 0$ while colors indicate a positive probability. The initial distribution is derived from a quantum gas of $N = 100$ atoms at a temperature of $T_0 = 20\,\mathrm{nK}$. The tilt of the final phase-space distributions reflects classical correlations between the generalized position and momentum which reduce the squeezing in n and are due to the non-adiabatic settling to a thermal state, see FIG. 4.3.

Section 4.2.

In FIG. 4.5, we illustrate the evolution of the probability distribution $P(n, \phi; t)$, Eq. (4.7), for $N = 100$ particles, for the usual evolution as shown in FIG. 4.3. The left picture shows the initial distribution corresponding to the Wigner function (A.7) at $t = 0$ while the right panel shows P after $t = 0.68\, t_{max}$ of classical evolution. The white areas indicate $P(n, \phi; t) \approx 0$ while colors according to the colormap indicate an increasing probability.

A wide distribution in either direction reflects large fluctuations of the respective observable. On the other hand, a narrow distribution indicates squeezing of the corresponding observable. The initial distribution would remain unchanged if the parameters U and J remained constant, as it corresponds to a thermal state and is therefore in equilibrium. Changing, however, these couplings as in the ramp defined by FIG. 3.2, i.e., decreasing the ϕ-dependent potential term in the Hamiltonian (4.4), the distribution P varies as the finite distribution over "momenta" n leads to an expansion of the distribution in the widened cosine potential, see Eq. (4.4). Tuning J to zero allows infinite expansion in the "position" direction ϕ within the n–ϕ phase space.

Due to the initial finite distribution in n, however, classical correlations between n and ϕ develop, tilting the large-time probability distribution with respect to the vertical axis as seen in the right panel of FIG. 4.5 and keeping the expansion finite. In summary,

the evolution of the system in the experiment [Estè08] can be understood to a good approximation as classical squeezing of the phase-space distribution.

4.2   Squeezing: Quantum statistical effects

In the evolution of a weakly interacting quantum gas, quantum fluctuations to leading order enter through zero-point fluctuations in the initial state, i.e., they characterize the scattering into empty and out of nearly empty modes and play little role in the scattering in and out of strongly occupied modes. In the language of the path integral this means that the full quantum evolution is, to a good approximation, given by a classical Liouvillean propagation of the initial-time Wigner function which accounts for quantum fluctuations in the initial state, see, e.g., [Berg07, Polk09]. Strong interactions have the potential to alter this semi-classical evolution considerably. However, as is illustrated by our above results, quantum fluctuations also in this case have only little effect if all available modes are strongly occupied during the evolution.

To see the distinct effects of quantum fluctuations during the evolution, it is required use a larger number of degrees of freedom. Most of which should stay weakly occupied. Alternatively, one needs to measure observables with a resolution at the few-particle level. Using the two-well potential, one may see the effect of quantum fluctuations by introducing a tilt such that, on average, only a few particles occupy one of the wells.

In the following we stay with equal populations in the two modes but consider the variance of the relative particle number at very low temperatures, where fluctuations on the order of a few atoms become relevant. At the low temperatures to be considered the initial state is dominated by the ground state of the Hamiltonian. When we drive the system into the Fock regime, i.e. we allow it to move to the lower left corner in the graph shown in FIG. 3.8. For an even total number of atoms the relative number fluctuations between the modes in this regime are strongly reduced while the undefined phase allows interferences on the surface of the Bloch sphere. As we will see later, this does not hold for an odd total particle number.

In FIG. 4.6, we compare the evolution of the exact quantum (blue solid line) and semiclassical (purple solid line) evolutions of a system starting in the ground state of the Hamiltonian, with the initial parameters U and J given by the ratio

$$\frac{J(t_0)}{UN} = 6, \tag{4.9}$$

for a gas of $N = 100$ atoms. This corresponds to $(\Delta n(t_0))^2 = 24$ and $\alpha(t_0) = 0.993$. We take $U = $ const. during the entire evolution and an exponential ramp of J given by

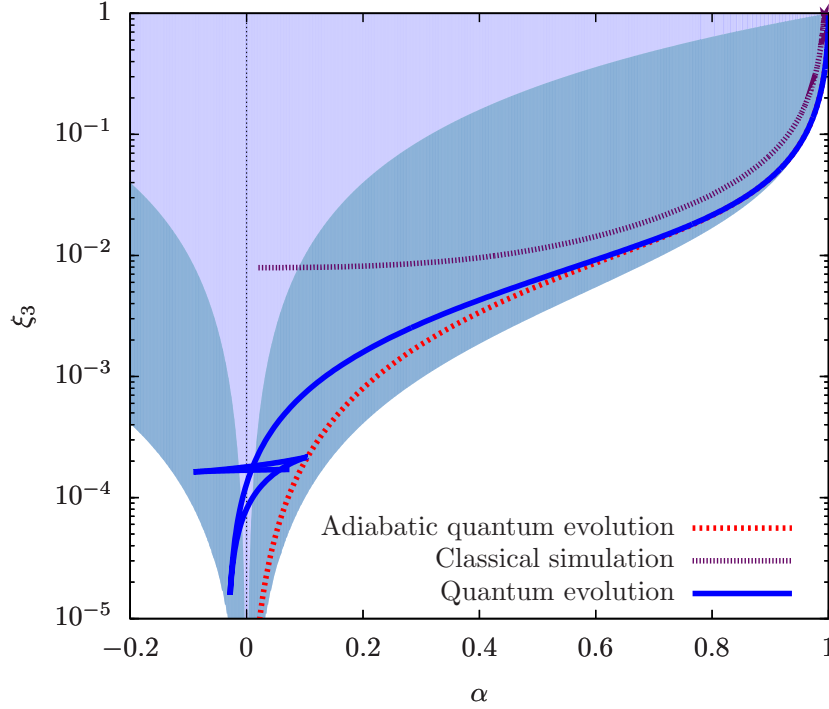$$\frac{J(t)}{UN} = \frac{J(t_0)}{UN} \exp\{-t/\tau\} \tag{4.10}$$

FIGURE 4.6: Evolution of the coherence α and the squeezing parameter ξ_3 related to the number variance through $(\Delta n)^2 = N\xi_3/4$ for a gas of $N = 100$ atoms under a very slow ramp-up of $U(t)/J(t)$ as given in Eq. (4.10). The quantum evolution is represented by the (blue) solid line while the classical statistical evolution is the (purple) dotted line. The system starts in the ground state of the Bose-Hubbard Hamiltonian for $NU/J(t_0) \simeq 0.16$. This corresponds to $(\Delta n(t_0))^2 = 24$ and $\alpha(t_0) = 0.993$. The total evolution time is $t_{\max} = 10.18\,\text{s}$. The evolution under an adiabatic change of the parameters U and J, i.e., for $1/\tau \to 0$ is shown by the (red) short-dashed line. See FIG. 3.8 and Sect. 3.4.1 for the definition of the areas allowed by the constraint Heisenberg and metrology gain limits, distinguished by different shading.

with $\tau = 0.55\,\text{s}$. The evolution takes place over the period of $t_{\max} = 64\,\text{s}$. For a fully adiabatic change of the parameters U and J, i.e., for $1/\tau \to 0$, the evolution would follow the red short-dashed line which corresponds to the dependence of $(\Delta n)^2$ on α in the ground state shown as a red solid line in FIG. 3.9.

Let us first discuss the the semi-classical evolution in FIG. 4.6. We see it that exhibits deviations to the adiabatic and quantum evolution, significantly bigger than those shown in FIG. 4.3. The evolution of both $(\Delta n)^2$ and α as a function of time show those differences. On the first hand, regarding atom number fluctuations, the classical curve approaches the value $(\Delta n)^2 \simeq 0.2$ and cannot follow the quantum one below this limit. To actually see this in an experiment, one needs a initial temperature T low enough

that the adiabatic evolution goes below the quantum regime $(\Delta n)^2 \lesssim 0.2$. We have found numerically that it can only be reached for $T \lesssim 20\,\mathrm{nK} \simeq 10\,UN$. On the second hand, concerning the coherence parameter α, the classical curve simply approaches zero indicating a distribution on the Bloch sphere symmetric under $S_1 \leftrightarrow -S_1$. In this limit, the classical phase space distribution wraps around the equator of the Bloch sphere and reflects a completely undetermined relative phase between the wells.

Let us now discuss the quantum evolution of the system. We see that, in contrast, the coherence oscillates around zero, corresponding to an asymmetric distribution of phase. This is shown by the means of the the Wigner function in FIG. 4.7. In particular, the lower left panel shows the Wigner function when the coherence α is the most negative. Due to interferences the Wigner function starts to oscillate as soon as the phase distribution fully wraps around the equator. This leads to oscillations both in $(\Delta n)^2$ and α during the final time evolution shown in FIG. 4.6. The oscillations in $(\Delta n)^2$ are damped and equilibrate at a value close to the point where α reached zero for the first time. In the lower panels of FIG. 4.7 the Wigner function is shown for the evolution times $t/t_{max} = 0.75$ (left) and $t/t_{max} = 0.9$ (right), i.e. for maximally small $\xi_3 \simeq 2 \cdot 10^{-5}$ at $\alpha \simeq -0.02$, and maximally negative $\alpha \simeq -0.1$ at $\xi_3 \simeq 2 \cdot 10^{-4}$, respectively, see FIG. 4.6. This shows that negative α arises from a maximum of the Wigner function at $|\phi| = \pi$, instead of having it at $\phi = 0$ as in the rest of the evolution. We remark that, in this pure quantum regime of the evolution, W becomes negative, for all ϕ, as we go away from equal population, for $|n| > 5$. In fact, there is a series of decaying oscillations of the Wigner function around zero as we go to higher n. Those are however hard to see in FIG. 4.7. The first minima at $|n| \simeq 6$ are at the center of the grey zones.

FIG. 4.8.(a) shows the dependence of $\xi_3 = 4(\Delta n)^2/N$ on t, on a semi-logarithmic scale, as above for the exponential ramp (4.10) with $\tau = 0.55\,\mathrm{s}$. The red dashed line corresponds to adiabatic evolution ($\tau \to \infty$) while the blue solid and purple short-dashed lines represent the near-adiabatic quantum and semiclassical evolutions for $\tau = 0.55\,\mathrm{s}$, respectively. The adiabatic curve shows three regimes in each of which $\log \xi_3$ varies linearly with time which correspond to the Rabi, Josephson, and Fock regimes, see Sect. 3.3. The full quantum evolution, as shown in FIG. 4.6, exhibits an oscillatory behavior of ξ_3, during which the squeezing parameter undershoots the adiabatic ground-state curve and eventually settles to a finite value smaller than that in the classical limit. Although ξ_3 falls below the value it can reach in an adiabatic ramp, this does not contradict the Heisenberg limit as is clearly seen in FIG. 4.6.

As a contrast we show, in FIG. 4.8.(b), that squeezing below the classical limit is not possible for systems with an odd total number N of particles. This is due to the degenerate nature of the ground state, as was discussed in Section 3.3.2 and in particular in Eq. (3.14). In this case, the semiclassical evolution perfectly describes the dynamics of the formation of squeezing correlations. To see the difference to the case of an even number of particles one trivially has to measure the particle number to better than half
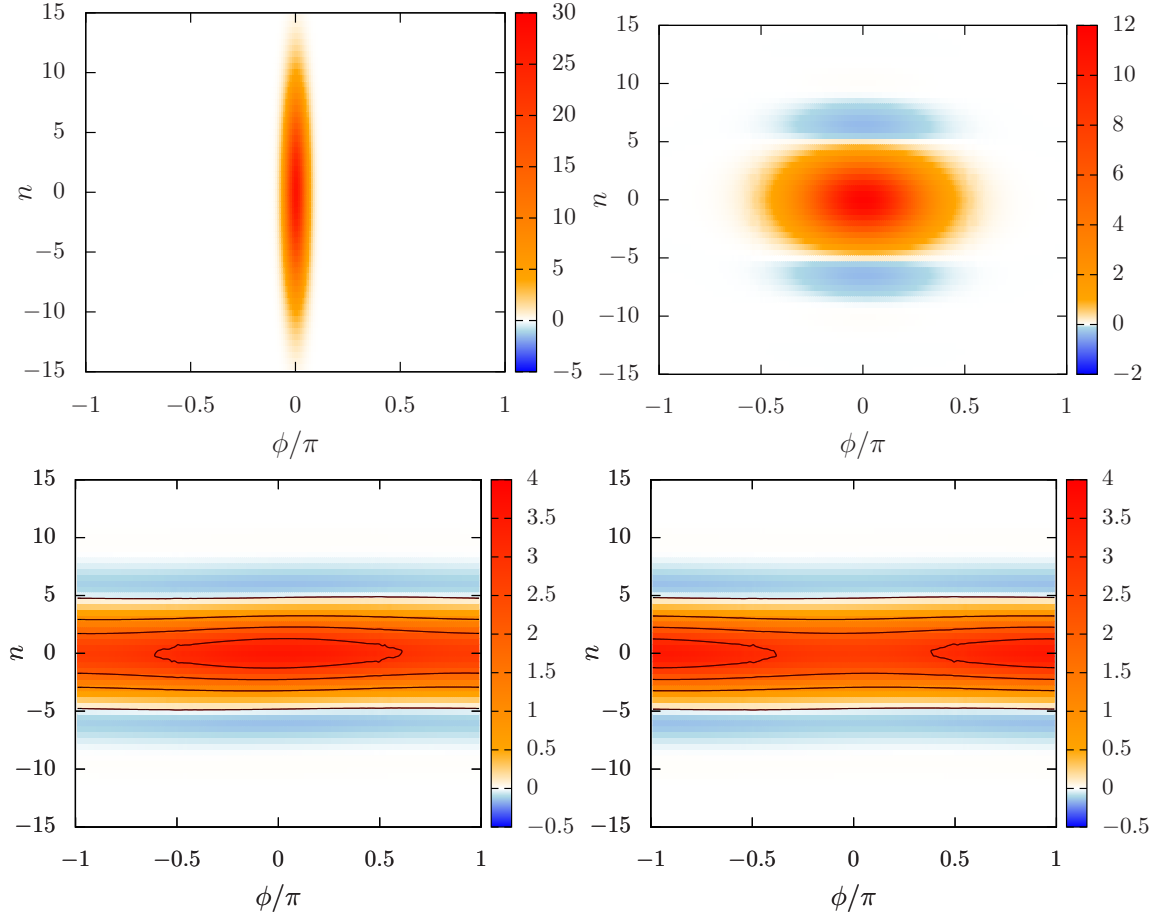
FIGURE 4.7: Evolution of the Wigner function for an inverse ramp speed $\tau = 0.55\,\mathrm{s}$, corresponding to the quantum evolution shown in Figs. 4.6 and 4.8. Colors encode the value of $W(n, \phi) \times 10^3$, see Eq. (A.7), with $n = (|\alpha|^2 - |\beta|^2)/2$ and $\phi = 2\arg(\alpha)$. W is negative in the blue areas. The initial distribution shown in the upper left panel is derived from the ground state of the Hamiltonian with $J(t_0)/NU = 6$ for $N = 100$ atoms. The upper right panel shows the Wigner function for the number-squeezed state reached at $t/t_{max} = 0.5$, with $\xi_3(0.5\,t_{max}) \simeq 3 \cdot 10^{-2}$, $\alpha(0.5\,t_{max}) \simeq 0.86$. In the lower panels we show the Wigner function at $t/t_{max} = 0.75$ (left) and $t/t_{max} = 0.9$ (right), i.e. for maximally small $\xi_3 \simeq 2 \cdot 10^{-5}$ at $\alpha \simeq -0.02$, and maximally negative $\alpha \simeq -0.1$ at $\xi_3 \simeq 2 \cdot 10^{-4}$, respectively (cf. FIG. 4.6). The contour lines help to show the position of the maxima in $|\phi| = 0$ and $|\phi| = \pi$, respectively.

a particle.

As was shown in Ref. [Java99], the relative number variance $(\Delta n)^2$ in the ground state as a function of the ratio $NU/4J$ of interaction over tunneling coupling, has the approximate value[2]

$$\xi_3 = 4(\Delta n)^2/N = (1 + NU/4J)^{-1/2}, \tag{4.11}$$

in the Josephson regime where the variance is distinctly smaller than the classical limit, $\xi_3 \ll 1$, but sufficiently larger than 1, i.e., where $N^{-1} \ll U/J \ll N$, see Sect. 3.3.

Taking into account the time evolution (4.10), our data confirms the approximate expression (4.11) in the Josephson regime. In the Fock regime the dependence of ξ_3 on J is approximately given by [Java99]

$$\xi_3 = 4(\Delta n)^2/N = 4NJ^2/U^2, \tag{4.12}$$

and the transition between the Josephson and Fock regimes occurs where $J/U \simeq 2^{-4/3}N^{-1}$.

Considering the non-adiabatic quantum evolution for $J(t)$ in Eq. (4.10), we find that $\xi_3(t)$ follows the ground-state dependence as long as the ramp rate is smaller than the Josephson frequency (3.7), $1/\tau \ll \omega_p$. As soon as the decreasing frequency ω_p falls below $1/\tau$ the squeezing parameter ξ_3 is frozen out, after some oscillations, at the approximate value [Java99]

$$\xi_3 = \sqrt{1 + (\pi NU\tau/2)^2} - \pi NU\tau/2. \tag{4.13}$$

FIG. 4.9 shows this limit as a function of the inverse ramp rate τ. The solid line gives the analytical formula (4.13) while the blue crosses and purple circles correspond to the asymptotic values for ξ_3 determined from a set of our quantum and semiclassical evolutions, respectively. Clearly, the semiclassical evolution cannot enter the Fock regime.

4.3   Conclusion

In this chapter, we have studied the production of squeezed states in an ultracold Bose gas in a double-well trap. First, we tuned our trapping parameters as to describe the experiment [Estè08]. There, the temperatures are such that the two-site Bose-Hubbard Hamiltonian well describes the system. We followed their experimental setup, starting from a gas separated by a weak barrier between the two wells, and therefore with a high possibly of tunneling. Afterwards, the time evolution was driven by a slow, yet

---

[2]Note that in Eqs. (18), (23), and (25) of Ref. [Java99], the factor $\sqrt{N/2}$ should rather read $\sqrt{N}/2$.
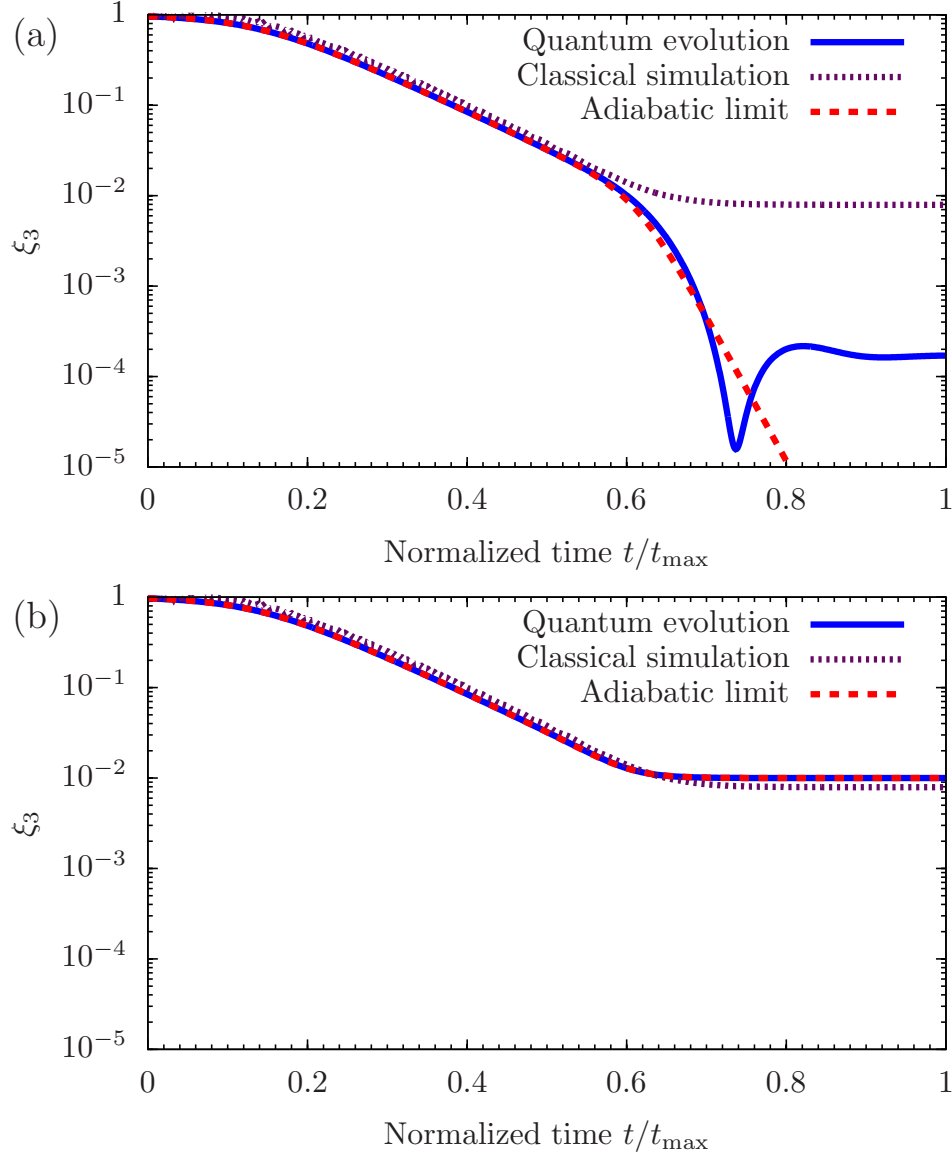
FIGURE 4.8: Evolution of the squeezing parameter ξ_3 related to the number variance through $(\Delta n)^2 = N\xi_3/4$ for a gas of $N = 100$ (top) or $N = 101$ (bottom) atoms under a very slow ramp-up of $U(t)/J(t)$ as given in Eq. (4.10). The quantum evolutions are represented by the (blue) solid lines while the classical statistical evolutions are the (purple) short-dashed lines. The initial state and all other parameters are chosen as in FIG. 4.6. The evolution under an adiabatic change of the parameters U and J is shown by the (red) long-dashed line.
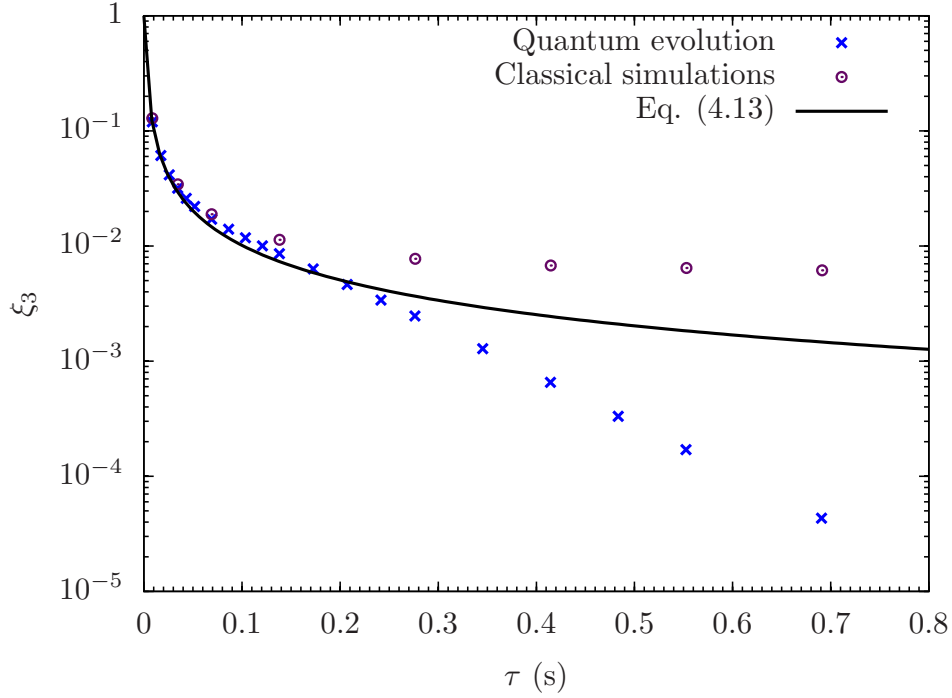
FIGURE 4.9:   (Color online) Final value of $\xi_3(t_{\max})$ obtained after an evolution time $t_{\max} = 18.4\tau$ vs ramp speed τ. The solid line corresponds to the analytical result in Eq. (4.13) valid in the Rabi and Josephson regimes. The (blue) crosses and (purple) circles are the corresponding final values obtained from a full quantum evolution and semiclassical evolution of the initial state, respectively. In the Fock regime which can be reached for ramp rates $1/\tau < 2\pi\,\mathrm{s}^{-1}$ the squeezing becomes stronger than the classical limit $\xi_3 \simeq 6 \cdot 10^{-3}$.

non-adiabatic, ramp-up of the barrier. During that evolution, we studied in particular the change of the fluctuation of the particle number difference between the two sites and the coherence, which is an observable related to the relative phase. We have seen how a many-body state with particle number squeezing was created during the evolution, and how it was at the expense of the relative phase.

We have shown that squeezing was possible for a finite ramp-up speed, and how its final value was determined by the initial temperature and the ramp-up speed. This is due to the quadratic nature of the high energy part of the spectrum in the Josephson regime. This quadratic part reaching populated states at a point in the ramp-up depending on the initial temperature. Futhermore, once the tunneling is suppressed such that the two lowest states are separated by an energy similar to the inverse ramp rate, the squeezing reaches a saturation point. We have expressed the model and the dynamics in terms of Bloch angular momentum operators. We want to stress again here that this pictorial

description makes it easier to draw the connection between a two site system to a system with two internal degrees of freedom, and to spin squeezing.

Secondly, we focused on the distinction between quantum and classical statistical fluctuations. To that end, we compared the full quantum evolution to classical statistical simulation, using the Wigner function formalism. We have shown that, for the parameter range of the experiment in Ref. [Estè08], the production of squeezing is purely classical. Going to a squeezing below that classical limit is possible. However, to get to the low number of degrees of freedom, one needs significantly lower temperatures and a precision in the particle number measurement up to the single-particle level. In that regime, significant differences arise between systems with odd and even particle number. As a final note, the results are immediately applicable to any other experimental realization in which the two-mode Bose-Hubbard model can by used to describe the system. Those results may be of particular interest for mesoscopic dynamics experiments.

Part II

Quantum field evolution:
2PI effective action approach

Chapter 5

The two-particle irreducible effective action

In Part I, we discussed in detail the dynamics of a Bose-Gas on a lattice composed of two sites. In that case, it was possible to compute the quantum evolution using an exact numerical integration of the Bose-Hubbard Hamiltonian. This will no longer be possible in this second part when we expand the number of sites as the size of the Hilbert space is proportional to N^{N_S-1}, and therefore grows exponentially with the number of sites. If one want to simulate more than a few particles, the memory limit of actual computers is very quickly reached. Hence other numerical methods have to be considered to describe the dynamics of the Bose gas.

In Part II, we choose an approach which involves 2PI effective action. This approach makes no assumption on how close the initial state should be to thermal equilibrium. Other numerical schemes exist to describe quantum systems, both near and far from equilibrium, for example density matrix renormalization group [Scho05, Whit04], time-dependent block-decimation [Vida04] and functional renormalization group [Gase08] methods.

This chapter covers the introduction of the 2PI method, and the derivation of its equations of motion. It is discussed in detail by J. Berges in the review [Berg05], and the derivation of the equations of motion for the case of the Bose-Hubbard model in 1D is described with and without field expectation value in Refs. [Gase05, Temm06].

This procedure starts from a well-chosen generating functional $Z[J, R; \rho_D]$, from which an effective action $\Gamma[\phi, G]$ is derived. The equations of motion for the lowest-order one- and two-point correlation functions ϕ and G then follow using the principle of least action. These form a set of coupled non-linear differential equations. We will consider this problem from a given initial-value, which will yield path integrals along a Schwinger-Keldysh closed time path.

5.1   Lagrangian and classical action

The 2PI effective action can be used to solve a variety of problems described by different Hamiltonians. We will, in this case, limit ourselves to the study of systems described by the Bose-Hubbard Hamiltonian, as discussed in Chapter 2 and defined in Eq. (2.14). A classical action can be derived from it by replacing the operators $\hat{b}_i$ and $\hat{b}_i^\dagger$ by the complex fields $b_i(t)$ and $b_i^*(t)$ in the Lagrangian, and then integrating it over time.

$$
\begin{aligned}
S[b, b^*] = \int \mathrm{d}t \sum_i \Bigg(& \frac{i\hbar}{2}\left[b_i^*(t)\partial_t b_i(t) - b_i^*(t)\partial_t b_i(t)\right] - \epsilon_i b_i^*(t) b_i(t) \\
& J\left[b_{i+1}^*(t) b_i(t) + b_i^*(t) b_{i+1}(t)\right] + \frac{U}{2} b_i^*(t) b_i^*(t) b_i(t) b_i(t) \Bigg).
\end{aligned}
\tag{5.1}
$$

Using the expression of the Hamiltonian under an $\mathcal{O}(2)$-decomposition given in Eq. (2.18) and assuming $\hbar = 1$, the classical action, as a function of $\Phi_i^a(t)$, reads

$$
\begin{aligned}
S[\Phi] = \frac{1}{2} \int \mathrm{d}t \sum_i \Bigg(& \Phi_i^a(t) h^{ab} \partial_t \Phi_i^b(t) - \epsilon_i \Phi_i(t) \Phi_i(t) \\
& 2J\Phi_i^a(t)\Phi_{i+1}^a(t) + \frac{U}{2\mathcal{N}}\Phi_i^a(t)\Phi_i^a(t)\Phi_i^b(t)\Phi_i^b(t) \Bigg),
\end{aligned}
\tag{5.2}
$$

where $\mathcal{N}$ refers to the number of fields considered in the $\mathcal{O}(\mathcal{N})$ decomposition. In our case, this is simply $\mathcal{N} = 2$.

In the following derivation, another quantity $(G_{0ij}^{ab})^{-1}(t, t')$, obtained from this action by functional derivation, is used. It is called the classical inverse propagator, or free inverse propagator, and is defined as

$$
\begin{aligned}
(G_{0ij}^{ab})^{-1}(t, t') &= \frac{\delta^2 S[\Phi]}{\delta \Phi_i^a(t) \delta \Phi_j^b(t')} \\
&= \Bigg(\delta_{ij} h^{ab}\partial_t - \epsilon_i \delta_{ij}\delta^{ab} + J(\delta_{i-1,j} + \delta_{i+1,j})\delta^{ab} \\
&\quad - \frac{2U}{\mathcal{N}}\left[\Phi_i^c(t)\Phi_i^c(t)\delta_{ij}\delta^{ab} + 2\Phi_i^a(t)\Phi_j^v(t)\delta_{ij}\right] \Bigg) \delta(t - t').
\end{aligned}
\tag{5.3}
$$

In the following sections, it is sometimes convenient to simplify the notation by writing the time and space indices into a single generic variable $x = (i, t)$. So when it is not necessary to treat space and time differently, we will write, for example, $\Phi_i^a(t) = \Phi^a(x)$ or $(G_{0ij}^{ab})^{-1}(t, t') = (G_0^{ab})^{-1}(x, y)$.

5.2   Generating functional

In the following chapters, we will consider the dynamics of systems that are far from equilibrium, that is to say that the initial density matrix of the system $\hat{\rho}_D(t_0)$ is not, for example, a thermal state, $\hat{\rho}_D(t_0) \neq \mathrm{e}^{-\beta \hat{H}}$. This has to be encoded in the generating functional. Therefore, we choose a generating functional that covers both the initial conditions and the dynamics of the system, as we will see later. It reads

$$Z[J, R; \rho_D] = \mathrm{Tr}\left\{\hat{\rho}_D(t_0)\mathcal{T}_\mathcal{C} \exp\left[i\left(\int_x J^a(x)\hat{\Phi}^a(x) + \frac{1}{2}\int_{xy} R^{ab}(x,y)\hat{\Phi}^a(x)\hat{\Phi}^b(y)\right)\right]\right\}.$$
(5.4)

In this equation, $\mathcal{T}_\mathcal{C}$ denotes time ordering along the closed time path $\mathcal{C}$ that will be discussed just below. We introduced auxiliary source terms, J and R, to be able to extract values on the macroscopic field and the connected two-point function (5.3). Let us go further and express the generating functional (5.4) into a functional integral representation. We now use the basis of the eigenstates of the field operators at time t_0, defined as

$$\hat{\Phi}(i,t_0)\left|\Phi_\pm(i,t_0)\right\rangle = \Phi_\pm(i,t_0)\left|\Phi_\pm(i,t_0)\right\rangle,$$
(5.5)

making again the time dependence explicit. First, we express the trace in that basis, $\mathrm{Tr}\{\cdot\} = \int \mathcal{D}\Phi_+ \langle\Phi_+| \cdot |\Phi_+\rangle$ and we insert the closing relation $1 = \int \mathcal{D}\Phi_- |\Phi_-\rangle \langle\Phi_-|$ in Eq. (5.4), yielding

$$Z[J, R; \rho_D] = \int \mathcal{D}\Phi_+ \int \mathcal{D}\Phi_- \langle\Phi_+|\hat{\rho}_D(t_0)|\Phi_-\rangle$$
$$\langle\Phi_-|\mathcal{T}_\mathcal{C} \exp\left[i\left(\int_x J^a(x)\hat{\Phi}^a(x) + \frac{1}{2}\int_{xy} R^{ab}(x,y)\hat{\Phi}^a(x)\hat{\Phi}^b(y)\right)\right]|\Phi_+\rangle.$$
(5.6)

The second part of this expression is a transition matrix element which can be expressed, in quantum field theory, as a path integral. Since the two boundaries of this integral have the same time, one uses a closed, finite real-path called the Schwinger-Keldysh closed time path [Schw61]. This path $\mathcal{C}$ starts for the initial time t_0, extends to the largest relevant time, then goes back to t_0 again, as pictured in FIG. 5.1.

The time ordering operator of (5.4) takes here all its meaning, as it orders times along the path and not in absolute values. It is the normal time ordering along the forward path $\mathcal{C}^+$, it goes then backwards with time on the return curve $\mathcal{C}^-$, where all the times are considered to be after $\mathcal{C}^+$. Using standard techniques [Hatf86] on those
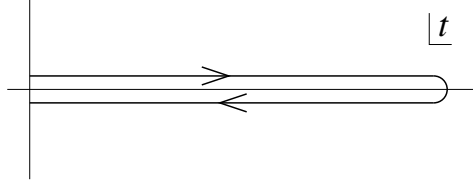
FIGURE 5.1:   Representation of the Schwinger-Keldysh closed time path [Schw61]. Figure from [Berg05].

matter elements, with that time contour, one obtains

$$
\langle \Phi_- | \mathcal{T}_\mathcal{C} \exp \left[i \left(\int_x J^a(x) \hat{\Phi}^a(x) + \frac{1}{2} \int_{xy} R^{ab}(x,y) \hat{\Phi}^a(x) \hat{\Phi}^b(y) \right) \right] | \Phi_+ \rangle .
$$
$$
= \int_{\Phi_+}^{\Phi_-} \mathcal{D}' \Phi \exp \left[i \left(S[\Phi] + \int_x J^a(x) \Phi^a(x) + \frac{1}{2} \int_{xy} R^{ab}(x,y) \Phi^a(x) \Phi^b(y) \right) \right] , \tag{5.7}
$$

where $S[\Phi]$ is the classical action of our system (5.2).

As mentioned above, the initial conditions are encoded in the density matrix $\rho_D(t_0)$. However, its elements $\langle \Phi_+ | \hat{\rho}_D(t_0) | \Phi_+ \rangle$ can be expressed in a way that is more convenient in the path integral formalism. One can always write the elements of an arbitrary density matrix by functional expansions in cumulants [Berg05], that is to say

$$
\langle \Phi_+ | \hat{\rho}_D(t_0) | \Phi_- \rangle = \exp \left[i f_\mathcal{C}[\Phi] \right] \tag{5.8}
$$

The functional $f_\mathcal{C}[\Phi]$ can then be expressed in powers of the fields,

$$
f_\mathcal{C}[\Phi] = \alpha_0 + \sum_{n=1}^{\infty} \frac{1}{n!} \int_{x_1 \dots x_n} \alpha_n(x_1, \dots, x_n) \prod_{i=0}^{n} \Phi(x_i), \tag{5.9}
$$

where the α_n are the coefficients of the expansion. The density matrix is only specified at the initial time, which means those coefficients are all zero for all other times, $\alpha_n(x_1, \dots, x_n) = 0$, $\forall t_i \neq t_0$. Thus, the integration of the density matrix along the same time path as the second part of (5.7) will only contribute at both ends of the contour.

Furthermore, in many experimental setups, the system at the initial time t_0 is sufficiently well characterized if only the first two correlation functions are specified. Those are the mean-field $\phi^a(x)$ and the two-point correlation function $G^{ab}(x,y)$. It can be shown, as in Ref. [Berg05], that such condition is equivalent to taking an initial Gaussian many-particle density matrix, i.e. $\alpha_n = 0$, $\forall n > 2$.

The initial condition can therefore be included in the source terms by making the translation $J(x) \rightarrow J(x) - \alpha_1(x)$ and $K(x,y) \rightarrow K(x,y) - \alpha_2(x,y)$, and by α_0 in the

normalization constant of Z. The generating functional therefore takes the form:

$$Z[J, R; \rho_D] = \int \mathcal{D}'\Phi \exp\left[i\left(S[\Phi] + \int_x J^a(x)\Phi^a(y)\right.\right.$$
$$\left.\left. + \frac{1}{2}\int_{xy} R^{ab}(x, y)\Phi^a(x)\Phi^b(y)\right)\right]. \tag{5.10}$$

This is the same function as in the case of equilibrium, but with a closed time path $\mathcal{C}$, and the initial condition encoded in the source terms J are R are the initial times.

Because of the Schwinger-Keldysh contour $\mathcal{C}$, the dynamics possesses in general a dependence on the previous history of the system, that is to say that it is non-Markovian. This means that we will have to deal with non-local integro-differential equations. This time non-locality leads to memory integrals, that are numerically costly to evaluate but are in general necessary for accurate dynamics of the system.

5.3   2PI effective action

This section presents the derivation of an effective action for both the mean-field and and the two-point correlation function from the non-equilibrium generating functional. From this action, one can derive a set of coupled non-linear equations that are then solved numerically.

5.3.1   Correlation functions and Legendre transformations

The correlation functions are obtain from the the generating functional $W[J, R]$ defined from $Z[J, R]$ as

$$Z[J, R] = \mathrm{e}^{iW[J,R]}. \tag{5.11}$$

The mean field $\phi^a(x)$ and the connected two-point correlation function $G^{ab}(x, y)$ are obtained by functional derivatives of W,

$$\frac{\delta W[J, R]}{\delta J^a(x)} = \phi^a(x), \tag{5.12a}$$

$$\frac{\delta W[J, R]}{\delta R^{ab}(x, y)} = \frac{1}{2}(\phi^a(x)\phi^b(y) + G^{ab}(x, y)). \tag{5.12b}$$

Before constructing the 2PI effective action, let us first consider for a moment the 1PI effective action, which is constructed from $W[J, R]$ using a Legendre transform on

the source term linear in the fields $J^a(x)$ [Hatf86].

$$\Gamma^R[\phi] = W[J,R] - \int_x \frac{\delta W[J,R]}{\delta J^a(x)} J^a(x), \tag{5.13}$$

where one can see the non-vanishing source term $R \neq 0$ as an additional quadratic interaction. In other terms, this 1PI effective action could be derived in a standard way from the modified classical action $S^R[\Phi]$ related to the physical one by

$$S^R[\phi] = S[\phi] + \frac{1}{2}\int_{xy} R^{ab}(x,y)\phi^a(x)\phi^b(y). \tag{5.14}$$

The usual 1PI relations can then be derived from (5.13) for this modified action, for instance, the 1PI effective action to one-loop oder, see [Berg05], can be expressed as

$$\Gamma^{R(1\ \text{loop})}[\phi] = S^R[\phi] + \frac{i}{2}\text{Tr}\left[\ln(G_0^{-1}[\phi] - iR)\right], \tag{5.15}$$

where we have made use of the free inverse propagator $iG_0^{ab-1}(x,y)$ as defined in (5.3) but for the modified classical action (5.14).

5.3.2   2PI effective action

The full 2PI effective action is then obtained by performing a second Legendre transform with respect to the quadratic source term R:

$$\Gamma[\phi,G] = \Gamma^R[\Phi] - \int_{xy} \frac{\delta\Gamma^R[\phi]}{\delta R^{ab}(x,y)} R^{ab}(x,y). \tag{5.16}$$

Using the equations (5.12) and the definition (5.13), the 2PI effective action can be written as

$$\Gamma[\phi,G] = W[J,R] - \int_x \phi^a(x)J^a(x) - \frac{1}{2}\int_{xy} R^{ab}(x,y)\phi^a(x)\phi^b(y) - \frac{1}{2}\text{Tr}[RG]. \tag{5.17}$$

The stationarity conditions derived from this effective action, where a closed system corresponds to vanishing sources J and R,

$$\frac{\delta\Gamma[\phi,G]}{\delta\phi^a(x)} = -J^a(x) - \int_y R^{ab}(x,y)\phi^b(y)\bigg|_{J=R=0} = 0, \tag{5.18a}$$

$$\frac{\delta\Gamma[\phi,G]}{\delta G^{ab}(x,y)} = -\frac{1}{2}R^{ab}(x,y)\bigg|_{J=R=0} = 0, \tag{5.18b}$$

are leading to the equation of motion that we will integrate numerically later on.

The 2PI effective action action can also be expressed to the one-loop-order approximation, see [Berg05]. We use here the property $G^{-1} = G_0^{-1} - iR$, which is true due to the stationary condition at the one-loop level. We have

$$\Gamma^{(1 \text{ loop})}[\phi, G] = S[\phi] + \frac{i}{2}\text{Tr}\left\{\ln(G^{-1})\right\} + \frac{i}{2}\text{Tr}\left\{G_0^{-1}[\phi]G\right\} + \text{const}, \tag{5.19}$$

where we have taken into account that $\text{Tr}\left\{G^{-1}G\right\} = \text{Tr}\mathbb{1}$ is an irrelevant infinite constant.

We can then use this solution to ease the calculation of the general solution by separating the exact 2PI effective action into its one-loop component and *rest* term $\Gamma_2[\phi, G]$ containing all the remaining contributions to the effective action.

$$\begin{aligned}\Gamma[\phi, G] &= \Gamma^{(1 \text{ loop})}[\phi, G] + \Gamma_2[\phi, G] \\ &= S[\phi] + \frac{i}{2}\text{Tr}\left\{\ln(G^{-1})\right\} + \frac{i}{2}\text{Tr}\left\{G_0^{-1}[\phi]G\right\} + \Gamma_2[\phi, G] + \text{const}.\end{aligned} \tag{5.20}$$

We now vary this equation with respect to G, it yields

$$(G^{ab})^{-1}(x, y) = (G_0^{ab})^{-1}(x, y; \phi) - iR^{ab}(x, y) - \Sigma^{ab}(x, y), \tag{5.21}$$

where we have defined

$$\Sigma^{ab}(x, y) = 2i\frac{\delta\Gamma_2[\phi, G]}{\delta G^{ab}(x, y)}. \tag{5.22}$$

Eq. (5.21) is called the Schwinger-Dyson equation [Hatf86], while Eq. (5.22) establishes a relation between the self-energy Σ^{ab} and the functional derivatives of the term Γ_2. Since only 1PI diagrams contribute to the self-energy, one can see that Γ_2 contains only contribution from 2PI diagrams[1].

It shall be noted that by inverting (5.21) and expanding the result in Σ, one obtains the following expression for the full propagator,

$$\begin{aligned}G &= (G_0 - iR)^{-1} + (G_0 - iR)^{-1}\Sigma(G_0 - iR)^{-1} \\ &\quad + (G_0 - iR)^{-1}\Sigma(G_0 - iR)^{-1}\Sigma(G_0 - iR)^{-1} + ...,\end{aligned} \tag{5.23}$$

where we have neglected the indices for ease of notation. This means that there is a direct correlation between the full propagator G and an infinite series of 1PI diagrams expressed in terms of the classical propagator G_0, for example the two diagrams presented in Fig. 5.2.

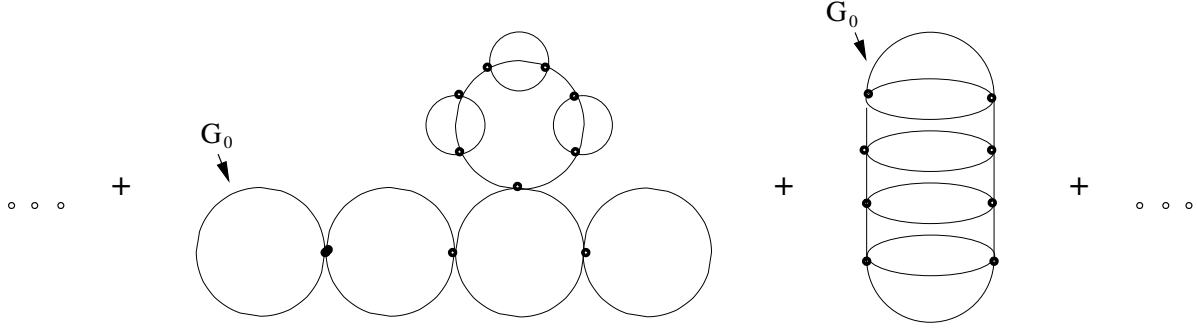[1]and therefore also nPI diagrams for all $n \geq 2$.

FIGURE 5.2: Two examples of the infinite number of 1PI diagrams expressed in terms of the classical propragator G_0 included in the full propagator G (5.23). Figure from [Berg05].

5.3.3   Loop-expansion of the 2PI effective action

The diagrammatic expression of Γ_2 is obtained in Ref. [Corn74] using a similar method to the 1PI expansion of the full propagator mentioned just above. However, the full propagator G is associated to a line, and only two-particle irreducible diagrams are considered. The Feynmann rules are obtained in the standard way [Hatf86] using the interaction part $S_{\text{int}}[\phi, \varphi]$ obtained by shifting the field $\Phi^a(x)$ to $\phi^a(x) + \varphi^a(x)$ on the classical action (5.2) discussed in section 5.1. Then, all the terms cubic and quartic in the fluctuation $\varphi^a(x)$ are collected, which yields

$$S_{\text{int}}[\phi, \varphi] = -\frac{U}{4\mathcal{N}} \int_x (\varphi^a(x)\varphi^a(x))^2 - \frac{U}{\mathcal{N}} \int_x \phi^a(x)\varphi^a(x)\varphi^b(x)\varphi^b(x), \qquad (5.24)$$

where $\mathcal{N}$ is the number of fields and where, in the first term, the sum over a is done before taking the square. This action gives us directly the allowed vertices, the first term connecting four full propagators G , while the second is an effective three-point vertex where the mean field ϕ is coupled to the propagators in an effective cubic interaction for non-vanishing mean fields. As Γ_2 is a functional, it contains only closed diagrams, and again those diagrams must be two-particle irreducible. They also contain only the vertices allowed by (5.24). In fact, Γ_2 contains all diagrams that fulfill those three conditions.

The contributing diagrams, up to three-loop order, are presented, for example, in FIG. 5.3. The red crosses represent the mean field ϕ, while the full propagator G is represented by the internal blue lines. The dots are the vertices. The four-vertex has a coupling of $U/4\mathcal{N}$, while the effective three vertex, denoted by a dot with a red cross attached, has a coupling of $U/\mathcal{N}$. At each vertex, there is a summation and an integration on the remaining free field indices a or b and space-time argument x, respectively.
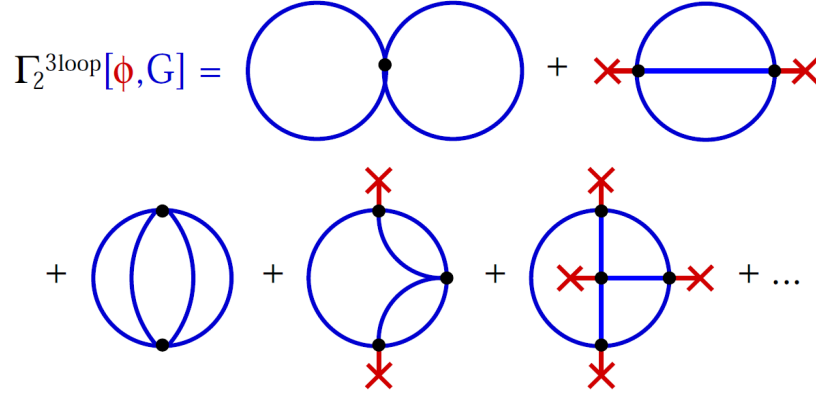
$$\Gamma_2^{3\text{loop}}[\phi,G] =$$

FIGURE 5.3: 2PI diagrams contribution to $\Gamma_2[\phi,G]$ and containing up to three loops. Figure from [Temm06].

5.3.4 Particle number and energy conservation

In order to solve the equations of motion (5.39) and (5.41) that we discuss below, details about the self-energy Σ (5.22) have to be known. In particular, we cannot practically take into account all the diagrams of expansion discussed of Γ_2 discussed in Section 5.3.3. Several expansion exists, for instance in powers of U or in the number of loops. We will consider a expansion in power of $1/\mathcal{N}$ as we will see in the next section. However, we show here that any truncation of diagrammatic expansion of Γ_2 conserves important quantities such as particle number or energy.

Number conservation

Particle number conservation follows from Noether and the invariance of the theory under orthogonal transformations. In the 2PI effective action formalism, it can be seen as follows. The stationary conditions (5.18) can be combined in the equation

$$h^{ab}\left[\phi^a(x)\frac{\delta\Gamma[\phi,G]}{\delta\phi^b(x)} + 2\int_y \frac{\delta\Gamma[\phi,G]}{\delta G^{cb}(y,x)}G^{ca}(y,x)\right] = 0. \tag{5.25}$$

Using the expression (5.20) of the effective action, this is equivalent to the relation

$$\partial_t n(x) + \nabla\cdot\mathbf{j}(x) = h^{ab}\left[\phi^a(x)\frac{\delta\Gamma_{\text{int}}[\phi,G]}{\delta\phi^b(x)} + 2\int_y \frac{\delta\Gamma_{\text{int}}[\phi,G]}{\delta G^{cb}(y,x)}G^{ca}(y,x)\right]. \tag{5.26}$$

where we have defined

$$n(x) = \phi^a(x)\phi^a(x) + G^{aa}(x,x), \tag{5.27a}$$

$$\mathbf{j}(x) = \frac{1}{m}\Big(\phi^1(x)\nabla\phi^2(x) - \phi^2(x)\nabla\phi^1(x)$$
$$+ \big\langle \mathcal{T}_{\mathcal{C}}[\hat{\Phi}^1(x)\nabla\hat{\Phi}^2(x) - \hat{\Phi}^2(x)\nabla\hat{\Phi}^1(x)]\big\rangle^{\mathcal{C}}\Big) \tag{5.27b}$$

corresponding to the particle-number density and to the current density. The interaction part of the effective action is

$$\Gamma_{\text{int}}[\phi,G] = \Gamma[\phi,G] - \Gamma[\phi,G]\big|_{U=0}. \tag{5.28}$$

If the right-hand side of (5.26) vanishes, this equation is a continuity equation and the particle number is automatically conserve. For contributions of $\Gamma_{\text{int}}[\phi,G]$ which contain only ϕ^2 or $\text{Tr}(G^n)$, the terms in the square brackets of (5.26) either vanish separately or are symmetric under the exchange of both field indices. Furthermore, if a term contains a invariant of the form $\text{Tr}(\phi\phi G^n)$, the combination of the terms in the square brackets is symmetric under the same exchange. Their contraction with h^{ab} implies that those terms do not contribute. Hence, the total number density is conserved locally because of the $\mathcal{O}(2)$ symmetry. This statement is true for any truncation of the effective action, since Γ_2 contains only invariants under $\mathcal{O}(2)$ transformations.

Energy conservation

Energy conservation is a consequence of the time translation invariance of $\Gamma[\phi,G]$, see Ref. [Arri05]. Consider the general translation in time

$$t \leftarrow t + \varepsilon(t) \tag{5.29}$$

where $\varepsilon(t)$ is an infinitesimal time-dependent scalar. The mean field and the two-point function transform under this infinitesimal translation as

$$\phi(x) \leftarrow \phi(x) + \varepsilon(t)\partial_t\phi(x), \tag{5.30a}$$
$$G(x,y) \leftarrow G(x,y) + \varepsilon(t)\partial_t G(x,y) + \varepsilon(t')\partial_{t'}G(x,y). \tag{5.30b}$$

Under this transformation, the effective action can be written as $\Gamma[\phi,G] \leftarrow \Gamma[\phi,G] + \delta\Gamma[\phi,G]$ with

$$\delta\Gamma[\phi,G] = \int_t T(x)\partial_t\varepsilon(t) \tag{5.31}$$

Because of the stationary conditions (5.18), the variation $\delta\Gamma[\phi, G]$ vanishes for all solutions of the equations of motion for ϕ_a and G_{ab}. Integration by parts on Eq. (5.31) show that $T(x)$ is the conserved Noether quantity for time translation,

$$\delta\Gamma[\phi, G] = 0 = -\int_t \partial_t T(x)\varepsilon(t). \tag{5.32}$$

The relation of this conserved quantity $T(x)$ with the energy density of the system was established in Refs. [Temm06, Arri05]. As all truncations of the effective action are also invariant under time translation, the energy is conserved for any approximation of the 2PI effective action.

5.3.5 $1/\mathcal{N}$-expansion

If we include the full expansion of Γ_2, the effective action $\Gamma[\phi, G]$ still describes the exact evolution of the system. It is in general not possible to find an useful exact analytic expression for Γ_2, therefore one truncates the series of diagrams at some level. Which approximation to choose depends on the physics of the systems, and the goals of the final numerical integration. There are several well-know methods, for instance [Bely58, Popo87], that include terms that are beyond the two-loop expansion, accounting for multiple scattering of the boson, and leading to non-local equations that include dissipation.

Here, we will use the $1/\mathcal{N}$-expansion. This approximation goes beyond the well-known Hartree-Fock-Bogoliubov mean-field approximation, that only takes Markovian dynamics into account and neglects multiple scattering. To describe a strongly interacting system, the coupling constant U is not a good parameter in which to expand Γ_2. So the classification of the diagrams in the effective action is done with respect to their scaling in $1/\mathcal{N}$, where $\mathcal{N}$ is the number of field component. In our case, as mentioned in Section 5.1, this is $\mathcal{N} = 2$. It includes non-Markovian dynamics (after the leading order) and describes multiple scattering processes.
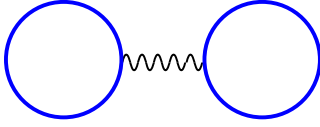
The expansion in powers of $1/\mathcal{N}$ does not depend explicitly on the coupling U, so we expect the truncation to valid also for large U. In practice, we limit our series by taking only the leading order term $\sim \mathcal{N}^1$ and the next to leading order one $\sim \mathcal{N}^0$. Each subsequent contribution being decreased further by a factor $1/\mathcal{N}$.

Details of the $1/\mathcal{N}$ expansion can be found for example in Refs. [Berg05, Temm06]. Here, we state which diagrams contribute to Γ_2 up to the leading order (LO) or the next-to-leading order (NLO),

$$\Gamma_2^{1/\mathcal{N}}[\phi, G] = \Gamma_2^{LO} + \Gamma_2^{NLO}. \tag{5.33}$$

The corresponding diagrams are presented in Fig. 5.4.

(a)

$\Gamma_2^{LO}[\phi,G] \; = \;$,

(b)

$\Gamma_2^{NLO}[\phi,G] = \;$

FIGURE 5.4: 2PI diagrams contribution to $\Gamma_2[\phi, G]$ up to the next to leading order in a $1/\mathcal{N}$ expansion. Each term has a prefactor that is here omitted. Figure from [Temm06].

As one can see in FIG. 5.4.(a), the LO consists of only one diagram which contains two loops, and is ϕ independent. At the leading order, the mean field contributions are all included in the one-loop component of Eq. (5.20). Each propagator loop scales with $\mathcal{N}$ and each vertex with $1/\mathcal{N}$. Therefore, the leading order term scales with $\mathcal{N}$. There is no other 2PI diagram with the same scaling. Its contribution to Γ_2 is given by
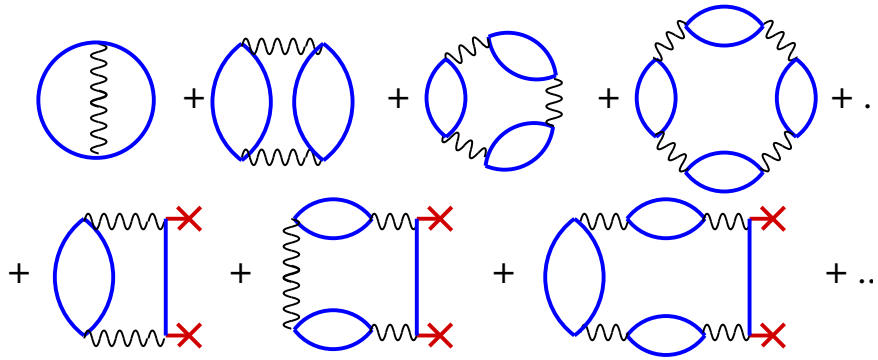
$$\Gamma_2^{LO} = -\frac{U}{\mathcal{N}} \int_x G^{aa}(x,x)G^{bb}(x,x). \tag{5.34}$$

The NLO diagrams, as shown in FIG. 5.4.(b), consists of two infinite series of diagrams in powers of U. All diagrams in the series are in the same power of N since the scaling of a propagator loop cancels the one of a vertex. The part of the diagram which consist of two effective three-point vertices connected by a propagator is of the same order as a propagator loop. So all diagrams are of order $\mathcal{N}^0$. It has been shown that the series can be resummed to an analytic expression using the resummation of the geometric series. Introducing two new functionals $B(x,y)[G]$ and $I(x,y)[G]$, the NLO contributions reads as

$$\Gamma_2^{NLO} = -\frac{i}{2}\mathrm{Tr}\left\{\ln(B[G])\right\}\int_x + \frac{iU}{\mathcal{N}}\int_{xy} I(x,y)[G]\phi^a(x)G^{ab}(x,x)\phi^b(y), \tag{5.35}$$

where the newly introduced functionals are defined as

$$B(x, y)[G] = \delta(x - y) + i\frac{U}{\mathcal{N}}G^{ab}(x, y)G^{ab}(x, y), \tag{5.36a}$$

$$I(x, y)[G] = \frac{U}{\mathcal{N}}G^{ab}(x, y)G^{ab}(x, y) - i\frac{U}{\mathcal{N}}\int_z I(x, z)[G]G^{ab}(z, y)G^{ab}(z, y). \tag{5.36b}$$

As B and I are independent from ϕ, the resulting $\Gamma_2^{1/\mathcal{N}}[\phi, G]$ is only quadratic in the fields. Indeed, it has been shown [Aart02] that invariants containing more than two field insertions are two-particle reducible, and therefore cannot contribute to Γ_2.

5.4 Equations of motion

In this section, we finally derive the equations of motion for our two fields $\phi^a(x)$ and $G^{ab}(x, y)$, first keeping Γ_2 in its general form, then by using the $1/\mathcal{N}$ approximation discussed in Section 5.3.5. Also, since the equation of motion contains explicit time derivatives, we go back to the previous notations $\phi^a(x) = \phi_i^a(t)$ and $G^{ab}(x, y) = G_{ij}^{ab}(t, t')$, discussed in Section 5.1, making the time dependence explicit again.

5.4.1 Exact equation

We will start this calculation by going back to the stationary conditions (5.18) using the generic form of the effective action defined in (5.20). The variation with respect to $G_{ij}^{ab}(t, t')$ yields

$$\frac{\delta\Gamma[\phi, G]}{\delta G_{ij}^{ab}(t, t')} = 0 = \frac{i}{2}\left[(G_0^{-1})_{ij}^{ab}(t, t') - (G^{-1})_{ij}^{ab}(t, t')\right] + \frac{\delta\Gamma_2[\phi, G]}{\delta G_{ij}^{ab}(t, t')}. \tag{5.37}$$

Remembering the definition (5.22) of the self-energy $\Sigma_{ij}^{ab}(t, t')$, the definition (5.3) of the classical inverse propagator, and the identity

$$\int_{\mathcal{C}} dt'' \sum_k \sum_c (G^{-1})_{ik}^{ac}(t, t'')G_{ik}^{cb}(t'', t') = \delta^{ab}\delta_{ij}\delta_{\mathcal{C}}(t - t'), \tag{5.38}$$

a convolution of (5.37) with another propagator G yields

$$\begin{aligned} h^{ac}\partial_t G_{ij}^{cb}(t, t') = & \epsilon_i G_{ij}^{ab}(t, t') - J\left[G_{i+1,j}^{ab}(t, t') + G_{i-1,j}^{ab}(t, t')\right] \\ & + \frac{U}{\mathcal{N}}\left\{\left[\phi_i^d(t)\phi_i^d(t)\right]G_{ij}^{ab}(t, t') + 2\phi_i^a(t)\phi_i^d(t)G_{ij}^{db}(t, t')\right\} \\ & + i\int_{\mathcal{C}} dt''\left(\sum_k \Sigma_{ik}^{ad}(t, t'')G_{kj}^{db}(t'', t')\right) + i\delta^{ab}\delta_{ij}\delta_{\mathcal{C}}(t, t'), \end{aligned} \tag{5.39}$$

where the field index summation remains implicit while we write explicitly space and time integrations.

Similarly, the variation of the action with respect to $\phi_i^a(t)$,

$$\frac{\delta\Gamma[\phi, G]}{\delta\phi_i^a(t)} = 0, \tag{5.40}$$

leads to the equation of motion for this field,

$$
\begin{aligned}
h^{ab}\partial_t\phi_i^b(t) = & \epsilon_i\phi_i^a(t) - J\left[\phi_{i+1}^a(t) + \phi_{i-1}^a(t)\right] \\
& + \frac{U}{\mathcal{N}}\left\{\left[\phi_i^c(t)\phi_i^c(t) + G_{ii}^{cc}(t,t)\right]\phi_i^a(t) + \left[G_{ii}^{ab}(t,t) + G_{ii}^{ba}(t,t)\right]\phi_i^b(t)\right\} \\
& - \frac{\delta\Gamma_2[\phi]}{\delta\phi_i^a(t)}.
\end{aligned}
\tag{5.41}
$$

5.4.2 Spectral and statistical correlation functions

To make the calculations easier, we will decompose the two-point function $G_{ij}^{ab}(t,t')$ into two parts, the spectral and statistical correlation functions. Those are associated with the only two independent real-valued two-point functions of a complex scalar field theory: the expectation values of the commutator and the anti-commutator of the field.

$$
\begin{aligned}
&\text{Spectral function:} \quad \rho_{ij}^{ab}(t,t') = i\left\langle[\hat{\Phi}_i^a(t), \hat{\Phi}_j^b(t')]\right\rangle^c \\
&\text{Statistical function:} \quad F_{ij}^{ab}(t,t') = \frac{1}{2}\left\langle\{\hat{\Phi}_i^a(t), \hat{\Phi}_j^b(t')\}\right\rangle^c
\end{aligned}
\tag{5.42}
$$

The superscript ^{c} refers to the connected two point function. Those two functions relate to the full propagator using the identity

$$G_{ij}^{ab}(t,t') = F_{ij}^{ab}(t,t') - \frac{i}{2}\rho_{ij}^{ab}(t,t')\mathrm{sgn}_\mathcal{C}(t-t'). \tag{5.43}$$

One should note that the spectral and statistical functions obey the symmetry relations,

$$F_{ij}^{ab}(t,t') = F_{ji}^{ba}(t',t), \tag{5.44a}$$

$$\rho_{ij}^{ab}(t,t') = -\rho_{ji}^{ba}(t',t). \tag{5.44b}$$

Furthermore, the definition of the spectral function implies that for equal times $t = t'$, the function is fixed by the bosonic commutation relation (2.16),

$$\rho_{ij}^{ab}(t,t) = h^{ab}\delta_{ij}. \tag{5.45}$$

The matrix h^{ab} was introduced in Eq. (2.17) and reads

$$\left(h^{ab}\right) = \begin{pmatrix} 0 & -1 \\ 1 & 0 \end{pmatrix}. \tag{5.46}$$

It is also convenient to use a similar decomposition for the other two-point quantities involved in the calculation. For instance, the decomposition of the self energy $\Sigma_{ij}^{ab}(t,t)$ is obtained by first separating it into local and non-local parts,

$$\Sigma_{ij}^{ab}(t,t) = \Sigma_{(\text{loc})ii}^{ab}(t,t)\delta_{ij}\delta_{\mathcal{C}}(t-t') + \Sigma_{(\text{nloc})ij}^{ab}(t,t'), \tag{5.47}$$

then the non-local part is split in analogy to (5.43), into two real-valued self-energy functions

$$\Sigma_{(nloc)ij}^{ab}(t,t) = \Sigma^{F\,ab}_{\ ij}(t,t') - \frac{i}{2}\Sigma^{\rho\,ab}_{ij}(t,t')\text{sgn}_{\mathcal{C}}(t-t'). \tag{5.48}$$

In a similar fashion, the field $I(x,y)[G]$, defined in Eq. (5.36b) of Section 5.3.5, is also written as

$$I_{ij}(t,t') = I_{ij}^F(t,t') - \frac{i}{2}I_{ij}^\rho(t,t')\text{sgn}_{\mathcal{C}}(t-t'). \tag{5.49}$$

5.4.3 Equations of motion to next-to-leading order in the $1/\mathcal{N}$-expansion

In this section, we go further in the expressions of the equation of motion (5.39) and (5.41) using the approximation of Γ_2 discussed in Section 5.3.5. That is to say that we will use $\Gamma_2[\phi,G] = \Gamma_2^{1/\mathcal{N}}[\phi,G]$ using the definition (5.33). Also, we use the decomposition (5.43) of the full propagator and (5.48) of the self-energy to express the equations of motion in terms of the new fields. The equation of motion then are given by

$$\begin{aligned}
h^{ac}\partial_t F_{ij}^{cb}(t,t') =& \epsilon_i F_{ij}^{ab}(t,t') - J\left[F_{i+1,j}^{ab}(t,t') + F_{i-1,j}^{ab}(t,t')\right] \\
&+ \frac{U}{\mathcal{N}}\left[\phi_i^d(t)\phi_i^d(t) + F_{ii}^{dd}(t,t)\right]F_{ij}^{ab}(t,t') \\
&+ \frac{2U}{\mathcal{N}}\left[\phi_i^a(t)\phi_i^d(t) + F_{ii}^{ad}(t,t)\right]F_{ij}^{db}(t,t') \\
&+ \int_0^t dt" \sum_k \Sigma^{\rho\,ad}_{ik}(t,t")F_{kj}^{db}(t",t') \\
&- \int_0^t dt" \sum_k \Sigma^{F\,ad}_{\ ik}(t,t")\rho_{kj}^{db}(t",t'),
\end{aligned} \tag{5.50a}$$

$$
\begin{aligned}
h^{ac}\partial_t\rho_{ij}^{cb}(t,t') =& \epsilon_i\rho_{ij}^{ab}(t,t') - J\left[\rho_{i+1,j}^{ab}(t,t') + \rho_{i-1,j}^{ab}(t,t')\right] \\
& + \frac{U}{\mathcal{N}}\left[\phi_i^d(t)\phi_i^d(t) + F_{ii}^{dd}(t,t)\right]\rho_{ij}^{ab}(t,t') \\
& + \frac{2U}{\mathcal{N}}\left[\phi_i^a(t)\phi_i^d(t) + F_{ii}^{ad}(t,t)\right]\rho_{ij}^{db}(t,t') \\
& + \int_{t'}^{t}\mathrm{d}t"\sum_k \Sigma^{\rho ad}_{ik}(t,t")\rho_{kj}^{db}(t",t'),
\end{aligned}
\tag{5.50b}
$$

$$
\begin{aligned}
h^{ac}\partial_t\phi_i^c(t) =& \epsilon_i\phi_i^a(t) - J\left[\phi_{i+1}^a(t) + \phi_{i-1}^a(t)\right] \\
& + \frac{U}{\mathcal{N}}\left[\phi_i^d(t)\phi_i^d(t) + F_{ii}^{dd}(t,t)\right]\phi_i^a(t) \\
& + \frac{2U}{\mathcal{N}}F_{ii}^{ad}(t,t)\phi_i^d(t) \\
& + \int_0^{t}\mathrm{d}t"\sum_k \Sigma^{\rho ad}_{ik}(t,t")\big|_{\phi=0}\,\phi_k^d(t").
\end{aligned}
\tag{5.50c}
$$

One can remark here that this last equation (5.50c) possesses a trivial solution for the mean-field: $\phi_i^a(t) = 0$, valid for any values of the self-energy $\Sigma^{\rho ad}_{ik}(t,t")\big|_{\phi=0}$. This means that if the initial value of the mean field is set to zero, it will remain that way during the entire evolution. While this can simplify the calculations in a huge way, our dynamics usually contain a condensate from the beginning, which means that this mean field is non-vanishing and we have to take it into account.

Let us now express in more details the value of the self-energy Σ under the $1/\mathcal{N}$ approximation (5.33), using the decomposition (5.49) of the field I. One obtains

$$
\begin{aligned}
\Sigma^{F\,ab}_{ij}(t,t') = -\frac{2U}{\mathcal{N}}\Big\{ & I_{ij}^F(t,t')\left[\phi_i^a(t)\phi_j^b(t') + F_{ij}^{ab}(t,t')\right] \\
& + \frac{1}{4}\left[I_{ij}^\rho(t,t') + P_{ij}^\rho(t,t')\right]\rho_{ij}^{ab}(t,t') \\
& + P_{ij}^F(t,t')F_{ij}^{ab}(t,t') \Big\},
\end{aligned}
\tag{5.51a}
$$

$$
\begin{aligned}
\Sigma^{\rho\,ab}_{ij}(t,t') = -\frac{2U}{\mathcal{N}}\Big\{ & I_{ij}^\rho(t,t')\left[\phi_i^a(t)\phi_j^b(t') + F_{ij}^{ab}(t,t')\right] \\
& + \frac{1}{4}\left[I_{ij}^F(t,t') + P_{ij}^F(t,t')\right]\rho_{ij}^{ab}(t,t') \\
& + P_{ij}^\rho(t,t')F_{ij}^{ab}(t,t') \Big\}.
\end{aligned}
\tag{5.51b}
$$

To ease the notation, we have introduced the two functions P^F and P^ρ, defined as

$$
\begin{aligned}
P_{ij}^F(t,t') = -\frac{2U}{\mathcal{N}} \Bigg\{ & H_{ij}^F(t,t') \\
& - \int_0^t \mathrm{d}t'' \sum_k \left[H_{ik}^\rho(t,t'') I_{kj}^F(t'',t') + I_{ik}^\rho(t,t'') H_{kj}^F(t'',t') \right] \\
& + \int_0^t \mathrm{d}t'' \sum_k \left[H_{ik}^F(t,t'') I_{kj}^\rho(t'',t') + I_{ik}^F(t,t'') H_{kj}^\rho(t'',t') \right] \\
& - \int_0^t \mathrm{d}t'' \sum_k \int_0^{t'} \mathrm{d}t''' \sum_l I_{ik}^\rho(t,t'') H_{kl}^F(t'',t''') I_{lj}^F(t''',t'') \\
& + \int_0^t \mathrm{d}t'' \sum_k \int_0^{t''} \mathrm{d}t''' \sum_l I_{ik}^\rho(t,t'') H_{kl}^F(t'',t''') I_{lj}^F(t''',t'') \\
& + \int_0^t \mathrm{d}t'' \sum_k \int_{t''}^{t'} \mathrm{d}t''' \sum_l I_{ik}^\rho(t,t'') H_{kl}^F(t'',t''') I_{lj}^F(t''',t'') \Bigg\},
\end{aligned}
$$
(5.52a)

$$
\begin{aligned}
P_{ij}^\rho(t,t') = -\frac{2U}{\mathcal{N}} \Bigg\{ & H_{ij}^\rho(t,t') \\
& - \int_0^t \mathrm{d}t'' \sum_k \left[H_{ik}^\rho(t,t'') I_{kj}^\rho(t'',t') + I_{ik}^\rho(t,t'') H_{kj}^\rho(t'',t') \right] \\
& + \int_0^t \mathrm{d}t'' \sum_k \int_{t''}^{t'} \mathrm{d}t''' \sum_l I_{ik}^\rho(t,t'') H_{kl}^\rho(t'',t''') I_{lj}^\rho(t''',t'') \Bigg\}.
\end{aligned}
$$
(5.52b)

Again, a pair of new functions H^F and H^ρ was introduced. They are defined as

$$
H_{ij}^F(t,t') = -\phi_i^a(t) F_{ij}^{ab}(t,t') \phi_j^b(t'),
$$
(5.53a)

$$
H_{ij}^\rho(t,t') = -\phi_i^a(t) \rho_{ij}^{ab}(t,t') \phi_j^b(t').
$$
(5.53b)

One can see here that the newly introduced P functions vanish if the mean-field is set to zero. Since they contain double time integration, calculations with mean field are bound to be numerically more costly to solve that those without.

The last step in the derivation of the equation of motion is to find an expression for I. This is obtained by inserting the decomposition (5.49) into the equation (5.36b).

One obtains

$$
\begin{aligned}
I_{ij}^F(t,t') =& \frac{U}{\mathcal{N}} \left(F_{ij}^2(t,t') - \frac{1}{4}\rho_{ij}^2(t,t') \right) \\
& - \frac{U}{\mathcal{N}} \left\{ \int_0^t dt'' \sum_k I_{ik}^\rho(t,t'') \left(F_{kj}^2(t'',t') - \frac{1}{4}\rho_{kj}^2(t'',t') \right) \right. \\
& \left. - 2 \int_0^{t'} dt'' \sum_k I_{ik}^F(t,t'') F_{kj}^{ab}(t'',t')\rho_{kj}^{ab}(t'',t') \right\}, \\
I_{ij}^\rho(t,t') =& \frac{2U}{\mathcal{N}} F_{ij}^{ab}(t,t')\rho_{ij}^{ab}(t,t') \\
& - \frac{2U}{\mathcal{N}} \int_{t'}^t dt'' \sum_k I_{ik}^\rho(t,t'') F_{kj}^{ab}(t'',t')\rho_{kj}^{ab}(t'',t').
\end{aligned}
$$

(5.54a)

(5.54b)

which is a set of coupled integral equations which can be solved numerically.

We will see in the next chapter how one can numerically integrate the series of equations discussed in this chapter, in order to obtain numerical for the evolution of a Bose-gas on a lattice. Furthermore, we show how those simulation can be parallelized to take into advantage the fact that modern processors contain several cores and can execute instructions in parallel.

Chapter 6

Dynamics of a Bose gas in a lattice

In Ref. [Temm06], the dynamics of a degenerate Bose gas in a 1D lattice was studied for two and three sites. They compared the results obtained in the next-to-leading-order of the $1/\mathcal{N}$ expansion to exact numerical calculations and found qualitative agreement. However, quantitative differences were seen, in particular in the damping of the condensate fraction, which was underestimated. The results seemed to indicate the dynamics within the appropriate scheme are in better agreement with exact calculations for larger total number of particle N.

In the present work, we study the dependence of the evolution of the condensate fraction on the number of lattice sites N_S. As no exact calculations are available for a larger amount of site, we use classical statistical calculations as a reference. Therefore, we limit our study to the classical regime, where quantum fluctuations are expected to be small. In the initial states we consider, all particles are condensed on a single site. The lattice is taken with periodic boundary conditions, so it is not necessary to differentiate which site is initially loaded with particles. At later times, we study the distribution of the atoms on the lattice and the damping of the condensate fraction. The focus is set on the comparison between the dynamics obtained with the 2PI $1/\mathcal{N}$ NLO expansion and with semi-classical calculations.

The classical Hamiltonian equation of the system is discussed in Section 6.1 together with the expression of the initial state in that framework. We sketch the numerical implementation of the 2PI formalism in Section 6.2. The resulting dynamics of both schemes are presented in Section 6.3.

6.1 Classical dynamics

The classical model that we describe in this section is very similar to the one discussed in Section 4.1.2. The main difference arises from the ensemble in which we consider the system. In the 2PI formalism, the mean field describes the expectation value of the field operator, whose eigenstates are coherent states. As coherent states do not have a fixed particle count, we consider the classical system in the grand canonical ensemble.

The classical Hamiltonian function is obtained from the Bose-Hubbard equation (2.14) by replacing the field operator by a complex-valued variable $\hat{b} \to b$, or equivalently, using the $\mathcal{O}(2)$ decomposition from Section 2.3.1, by replacing the field components by real-valued numbers

$$\hat{\Phi}_i^a \to \Phi_i^a \tag{6.1}$$

in the Hamiltonian (2.18). The classical equation then reads

$$H = -J \sum_i \sum_a (\Phi_i^a \Phi_{i+1}^a) + \sum_i \frac{\epsilon_i}{2} \sum_a \Phi_i^a \Phi_i^a + \frac{U}{8} \sum_i \sum_{a,b} \Phi_i^a \Phi_i^a \Phi_i^b \Phi_i^b. \tag{6.2}$$

The initial state in the 2PI model is described by a coherent state $|\alpha_i\rangle$ on a single site $i = 1$,

$$\hat{b}_1 |\alpha_1\rangle = \alpha_1 |\alpha_1\rangle. \tag{6.3}$$

As in Sect. 4.1.2, we will use the Wigner function associated to the density matrix describing that state. For a single coherent state $|\alpha\rangle$, an analytic expression of the Wigner function is known, see e.g. Ref. [Wall94]. It reads

$$W_\alpha(\beta) = \frac{2}{\pi} \exp\left[-|\beta - \alpha|^2\right]. \tag{6.4}$$

For the empty lattice sites, the vacuum state $|0\rangle$ is equivalent to the coherent state $|\alpha = 0\rangle$. The Wigner function is a then a Gaussian centered around $\beta = 0$. The total Wigner function is a product of this type over all sites,

$$W(\beta_1, \ldots, \beta_{N_S}) = \left(\frac{2}{\pi}\right)^{N_S} \exp\left[-\sum_{i=1}^{N_S} |\beta_i - \alpha_i|^2\right]. \tag{6.5}$$

For the occupied site, the coherent state is given by $\alpha_1 = \sqrt{N}$, while for all the empty sites $i \neq 1$, $\alpha_i = 0$. The parameters β_i relate to the field components by

$$\beta_i = \frac{1}{\sqrt{2}} \left(\Phi_i^0 + i\Phi_i^1\right). \tag{6.6}$$

Therefore, the initial state is described in our classical simulation by a product of a complex Gaussian distributions of variance 1/2 per lattice bin. Furthermore, the Gaussian functions are always positive, and so is the resulting Wigner function. This confirms the classical nature of the initial states.

Numerical implementation of the semi-classical simulation is a straightforward process. The Gaussian distribution can be sampled using standard methods [Box58]. Then each sample point is evolved using Eq. (6.2). The observables are given as classical moments over the sampled distribution. Since the evolution of each point in the sample is independent, its numerical implementation fall into the category of so-called "embarrassingly parallel" problems. We used two different methods for parallelization: First a computer cluster was used to spread the calculations over multiple networked computers. Then, we used the massively parallel architecture of modern graphic cards for a further gain in computation performance.

6.2 Numerical implementation of the 2PI $1/\mathcal{N}$ NLO expansion

The equations of motion presented in Section 5.4.3 are in general too complicated to be solved analytically. However, they have the nice property to only depend on previous times, as a direct consequence of causality. One can therefore compute the evolution of the system in a single run.

To that end, all variables of the system have to be discretized. Since we consider a gas on a lattice, the space indices are already discrete. The discretization of time is quantified by the time step a_t. We write $t = na_t$, etc. The step size a_t is chosen manually so that the numerical results do not change anymore with a further decrease of its value. Note that numerical methods using variable time steps are not very practical in our case, as it complicates significantly the computation of the time integrals.

As we will see below, it is possible to improve the run time of the simulations by means of parallelization. The most convenient method is to use multiple computation units with shared memory on a single computer. Those units are the multiple core of a processors. Some computers also contains several processor to increase the number of core. We had access to computers equipped with up to 8 computation units.

6.2.1 Time integration

The mean field $\phi_i^a(n)$ depends on a single time index. Its equation of motion is thus integrated using a standard fourth-order Runge-Kutta method. For the two-point

functions $\rho_{ij}^{ab}(n,m)$ and $F_{ij}^{ab}(n,m)$, the picture is slightly more complicated as those function have two time indices. First, we notice that, due to the symmetry properties (5.44), it is sufficient to compute and store only half of the time values of the matrices. We take only $m \leq n$ into account. Then, the transition $F_{ij}^{ab}(n,m) \rightarrow F_{ij}^{ab}(n,m+1)$ depends on a single time. It is evaluated using the same fourth-order Runge-Kutta method. An equivalent technique is applied for $\rho_{ij}^{ab}(n,m)$. For the diagonal, some extra care has to be taken. For the spectral function, the diagonal is simply fixed by its definition (5.45), $\rho_{ij}^{ab}(n,n) = h^{ab}\delta_{ij}$. In order to maintain energy and particle number conservation, the diagonal element $(n+1, n+1)$ of the statistical function has to be calculated as

$$F_{ij}^{ab}(n+1,n+1) - F_{ij}^{ab}(n,n) = F_{ij}^{ab}(n+1,n) - F_{ij}^{ab}(n,n) + F_{ji}^{ab}(n+1,n) - F_{ji}^{ab}(n,n), \quad (6.7)$$

see Ref. [Rey04].

To evaluate the right-hand side of Eqs. (5.50), a few other functions have to be evaluated. First, one sees that the integral equations (5.54) for I^F and I^ρ are Volterra-type equations, see Ref. [Pres07] for a resolution method. These functions are calculated up to time n, then all the other secondary functions can be evaluated up to that time, by numerically computing the P^F and P^ρ integrals (5.52) using the trapezoidal rule. Then, all is known to express the self-energies Σ^F and Σ^ρ. Finally, the correlation functions ρ and F can be calculated for $n+1$, starting at $m=0$ and increasing to $m=n$. The new diagonal element is evaluated using Eq. (6.7) and the mean field is evaluated directly using the Runge-Kutta method.

The main disadvantage of this method is that the computational effort increases at each time step, as the size of the memory integral grows over time. Also, this memory kernel has to be stored on the computer. Fast memory is not available in infinite quantity and caching some of this data to the hard disk drives is not a viable option due to their large access times. However, the influence of early times on the late time behavior is usually suppressed. Therefore, we choose to neglect it and to keep memory only for a time interval T_{fill}. This interval is chosen such that the memory requirement are within the size of the fast RAM. For $t \leq T_{\text{fill}}$, the time integrals start at $t_0 = 0$ and we fill the memory kernel. For $t > T_{\text{fill}}$, the early time are gradually forgotten (removed from the memory) and the time integrals start at $t_0 = t - T_{\text{fill}}$.

To reduce further the computation time, we parallelized the computation regarding the various lattice sites. As the equations of motions are not completely independent, some care as to be taken. We mention here what can be evaluated independently. As most of the computational effort is put into the time integral, it is where the parallelization focus. In the integral equations (5.54), the I functions depend on other Is but only with the same first space index i. Solving the equations for different values of i can therefore be done at the same time. In Eqs. (5.52), the memory integrals of P are done

only on known objects. The calculation for different values of the two space indices i and j is thus independent. The time integration of the self energy in Eq. (5.50) can also be done in parallel, in both indices i and j. Other parallelizations were made, but most of the improvement in the run time comes from the computation of the objects above.

Since calculations are performed in parallel one spatial index, sometimes two, the ideal improvement in the run time is expected to scale at least with the number site N_S, and up to the square of that number N_S^2. Of course, this scaling holds only as long as there is enough computational units to handle all calculations at the same time.

6.2.2 Initial conditions and observables

We consider that the system consists initially of a coherent state of N particles on a single site and that the lattice has periodic boundary condition. This was realized experimentally, e.g., in the setup described in Ref. [Peil03]. We take the initial coherent state to be real valued and located on site 1. The action of the field operator $\hat{b}_i$ on the initial state $|\Psi_0\rangle$ is

$$\hat{b}_i |\Psi_0\rangle = \sqrt{N}\delta_{i,1} |\Psi_0\rangle , \tag{6.8}$$

and, for the field components (2.15),

$$\hat{\Phi}_i^a(0) |\Psi_0\rangle = \sqrt{2N}\delta_{i,1}\delta^{a,0} |\Psi_0\rangle . \tag{6.9}$$

The mean field is given the non-zero value

$$\phi_i^a(0) = \sqrt{2N}\delta_{i,1}\delta^{a,0}. \tag{6.10}$$

The initial spectral component is fixed by the commutation relation (5.45),

$$\rho_{ij}^{ab}(t,t) = h^{ab}\delta_{ij}. \tag{6.11}$$

The statistical component is calculated from its definition (5.42) and reads

$$F_{ij}^{00}(0,0) = F_{ij}^{11}(0,0) = \frac{1}{2}\delta_{ij}, \tag{6.12a}$$

$$F_{ij}^{01}(0,0) = F_{ij}^{10}(0,0) = 0. \tag{6.12b}$$

The two main observables we are interested in are the total population and the condensate fraction on each site. What we call the condensate fraction is the amount of particle on that site that are in a coherent state. The total population is given by

$$n_i(t) = \langle \hat{b}_i^\dagger(t)\hat{b}_i(t)\rangle = \frac{1}{2}(\phi_i^a(t)\phi_i^a(t) + F_{ii}^{aa}(t,t) - 1). \tag{6.13}$$

For a coherent state, the terms $F_{ii}^{aa}(t,t) - 1$ cancel each other, see (6.12). Therefore, we define the condensate fraction as

$$n_{C,i}(t) = \frac{1}{2}(\phi_i^a(t)\phi_i^a(t)). \tag{6.14}$$

In the classical simulation, the difference between those two observables is as follows: For the total particle number, the norm of the complex variable b_i is taken before the classical averaging over our sample is performed. For the condensate fraction, the means of the complex number taken first. The norm is taken on the resulting averages. Therefore, the condensate fraction includes information about the phase coherence of the gas that the total occupation does not.

6.3   Results

In this section, we discuss our results on the dynamics of a Bose gas on a lattice using both the 2PI $1/\mathcal{N}$ expansion. To ease the following discussion, we refer to them as "2PI results". The results are then compared to those obtained from the classical statistical evolution in order to understand what deviations are induced by the various approximations. In all the setups we study below, the atoms are initially all condensed on the same site and the lattice has periodic boundary conditions. The interaction-tunneling ratio is set to $U/J = 0.05$.

In the first case we consider, a condensate consists of $N = 80$ particles for all runs. The size of the lattice is different in each run, $N_S = 3, 5, 10, 20$. The results of both classical and 2PI simulations shown in Fig. 6.1. On the left-hand side of the figure, the total condensate fraction N_C/N is presented. The upper graph shows the results for the 2PI method. The general behavior is the same for all lattice sizes. As all atoms are initially condensed, the condensate fraction starts at 1. It then decays to zero within the same time scale for all lattice sizes. Taking the pink short-dashed curved as a reference, i.e. $N_S = 20$, one sees that the system follows the same evolution for a smaller lattice until it deviates from the reference curve. This happens later in time with increasing lattice sizes. This can be explained as follows: Initially, all the particles are located on a single site, the rest of lattice being empty. As the atoms distribute themselves to the to adjacent sites, the number of empty sites plays no role at that point. Then, the atom cloud gradually distributes on the rest of the lattice. The size of the system only plays a role once the full lattice is occupied. At that point in time, the evolution of the system starts to differ from the reference curve. This occurs latter for larger lattices. In other words, the initial evolution of a localized particle cloud does not depend on the size of the lattice, for as long as the cloud remains smaller than the lattice. At some point,
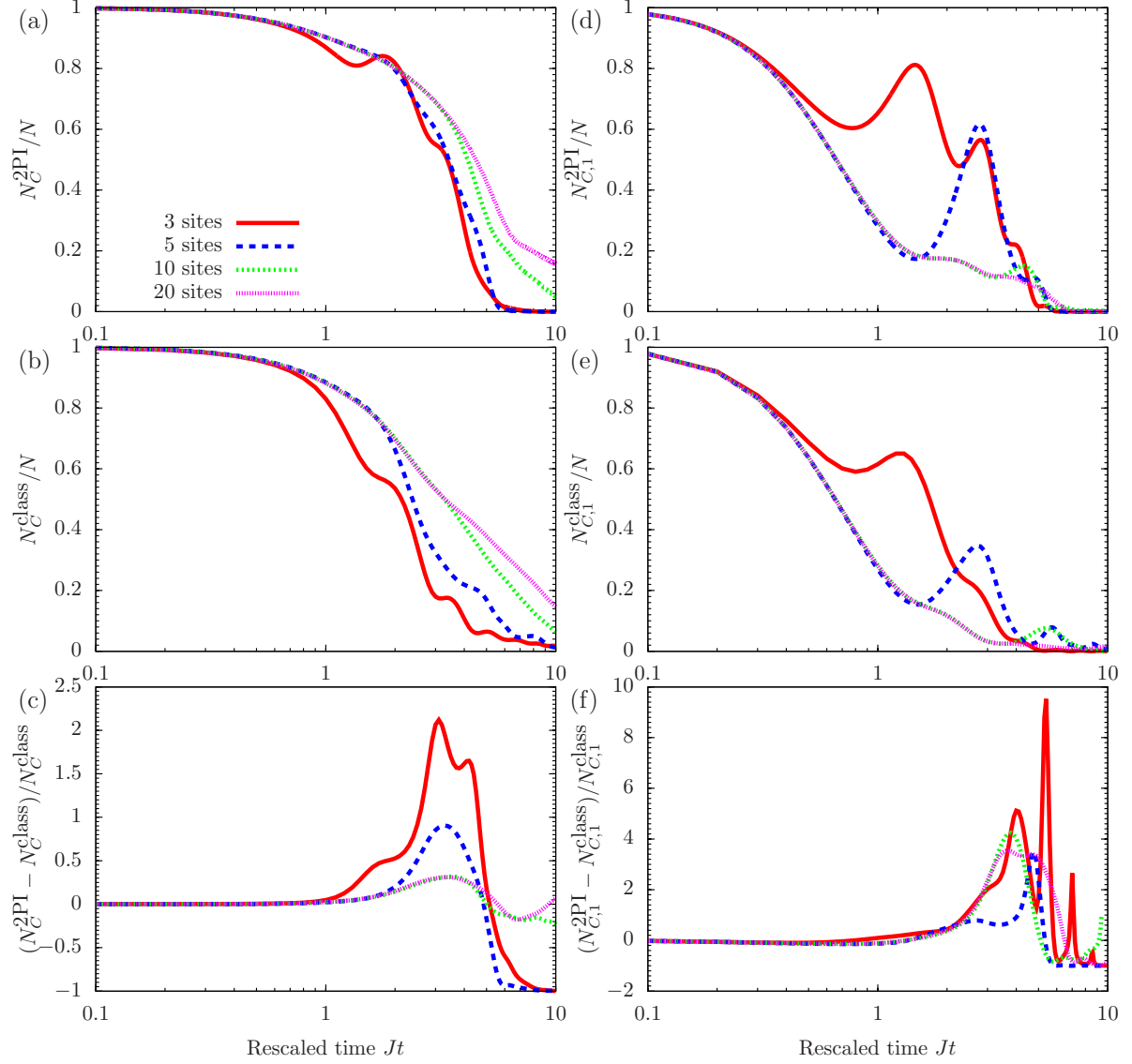
FIGURE 6.1: Evolution of the condensate fraction of a gas of $N = 80$ atoms where all atoms are initially condensed in a single lattice site. All simulations are done for $U/J = 0.05$ and the number of lattice sites is different for each curve $N_S = 3, 5, 10, 20$. The panels on the left present the total condensate fraction, while those on the right only the fraction in the initially occupied bin. The first line shows the quantum evolution obtained using our 2PI algorithm and the second classical simulations. The weighted difference between them is plotted on the last line. The color code is the same for all plots.

the evolution for $N_S = 20$ also differs from bigger lattices, but we have checked that it occurs outside of the times plotted here.

In FIG. 6.1.(b), we present the results obtained from classical statistical simulation. The system is the same as above. As we are in the classical regime, we expect this evolution to be closer to the exact evolution of the system. The behavior is qualitatively the same as is FIG. 6.1.(a), but values after $Jt = 1$ are smaller in the classical case. It confirms results from [Temm06] where it was seen that the 2PI method underestimates the damping of the condensate fraction. Also, the 2PI results shows a revival of the condensate fraction at $Jt \approx 1.5$, which is not present for the classical evolution.

In the lower left plot, FIG. 6.1.(c), we show the difference between those two evolutions, normalized to the classical value. One sees that the difference stays at zero until some time $Jt = 1$, then goes to a strong positive value at around $t/J \approx 2$ and finally goes to the value of -1. It shows again that the 2PI evolution overestimates the condensate fraction at intermediate times. This effect can be of a factor as high as 200% in the case $N_S = 3$, as shown by the red line. This agreement between the two schemes goes better with increasing lattice size, as we expected. However, no perfect agreement is reached even for larger lattices. The difference between the evolutions was still at around 25% for the largest lattices considered. The final value of -1 indicates that the 2PI evolution goes eventually faster to zero than the classical one.

The right-hand side of the graphs in FIG. 6.1 shows the evolution of the condensate fraction in the initially occupied well. The vertical ordering of the graphs is the same as on the left-hand side. The 2PI and semi-classical simulations are presented in graph (d) and (e), respectively. One sees a series of revival in the condensate fraction of the first site. Those are due to the Rabi oscillations, that causes the atoms to be back scattered into the initial well. The oscillations are qualitatively the same in both evolutions, but the 2PI results are overestimating their intensities. Graph (f) in FIG. 6.1 shows the normalized difference between those two results. Particularly large peaks are seen in the case $N_S = 3$, as shown by the red line. This will be explained in more details below, in the discussion of FIG. 6.4. Disregarding those peaks, an important feature to remark there, is that differences in the condensate fraction on a single site do not improve with bigger lattices. Within a Rabi oscillation, the larger difference is seen when the condensate fraction is the lowest.

In the second case we consider, we keep the the number of sites constant, $N_S = 2$ and look at the evolution of the condensate fraction with different total number of particles $N = 0.2, 1, 4, 40, 80$. The results of the 2PI evolution (and of classical simulations) are shown in the left-hand panel of FIG. 6.2 as full (dashed) lines, respectively. The different colors represent different total particle numbers N. The difference between those two results is plotted in the right-hand graph. The general behavior is the same as in the previous case considered, there is a decay of the condensate fraction. The time
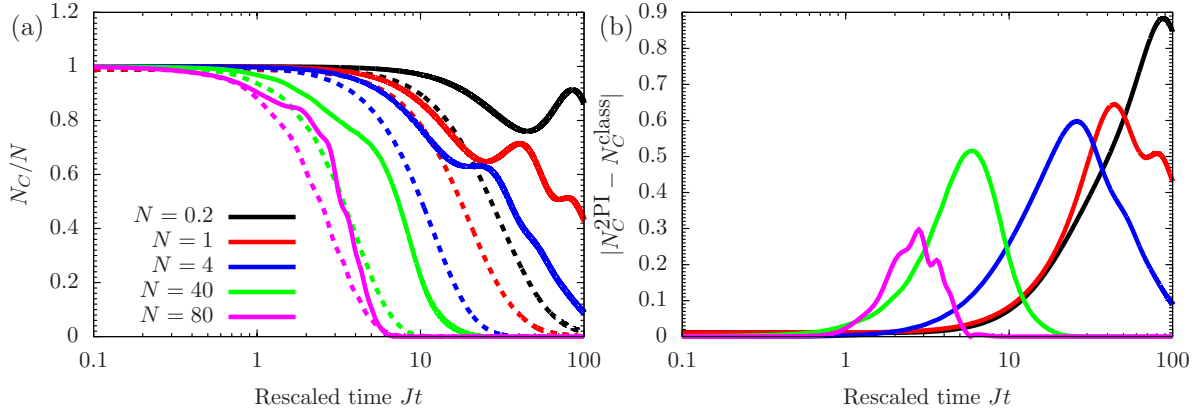
FIGURE 6.2: Evolution of the condensate fraction of a gas in a two-site lattice where all atoms are initially condensed on the first site. The total particle number is $N = 0.2, 1, 4, 40, 80$. The color of the corresponding curve is given in the legend. All simulations are done for $U/J = 0.05$. The left panel presents the total condensate fraction for the 2PI simulation (full line) and for classical evolution (dashed line). The difference between those two is shown in the right panel.

of the decay decrease with larger total particle number. The 2PI results are in better agreement with a larger amount of particles in the system. This confirms the findings from Ref. [Temm06]. Large differences arise for $N = 1$ and 0.2. In those cases, the average occupation per site is no longer larger than one. We are not anymore in the semi-classical regime and the classical simulations (dashed line) are not anymore a good approximation of the exact dynamics. Therefore, we cannot draw conclusions on the quality of the 2PI expansion when comparing its results to the classical ones for those small total particle numbers.

The third and last case we consider is very close to the first one, we also study the changes in the evolution of a condensate with increasing number of lattice sites N_S. This time, the average number of particle per sites is kept constant at $N/N_S = 10$, instead of the total particle number N. The results of the 2PI evolution (and classical simulation) are shown in the left-hand panel of FIG. 6.2, as full (dashed) lines, respectively. The normalized difference is plotted in the right-hand side. The curve of the normalized difference between the two methods is very similar for different lattice sizes. For $N_S = 5$ and 10, one sees a dip in the curve. This is actually a change of sign. After that, the difference settles at the value of -1. This effect was discussed above for the first case, see FIG. 6.1. In this case, when considering only the positive part of that difference, we do not see an improvement of the agreement of the 2PI results with the classical ones for larger lattice sizes.

The time in which the condensate decays decreases for larger lattices. There is
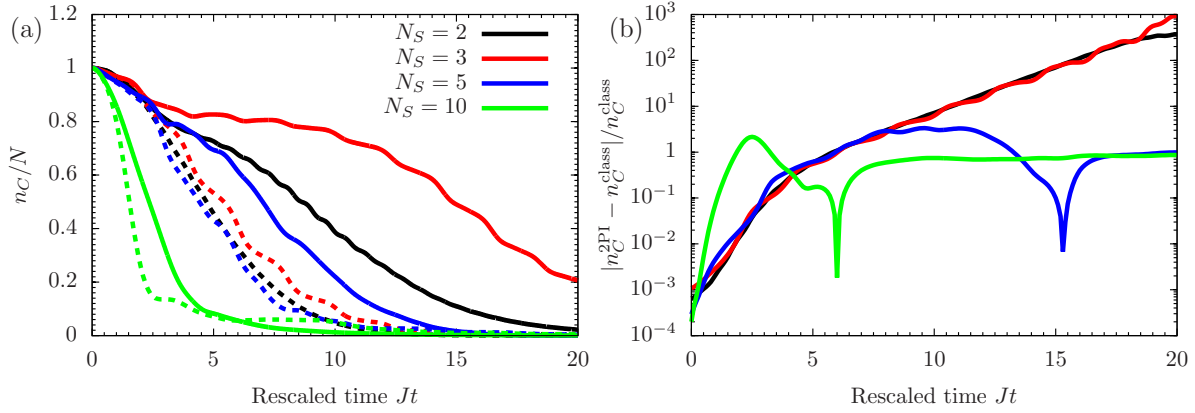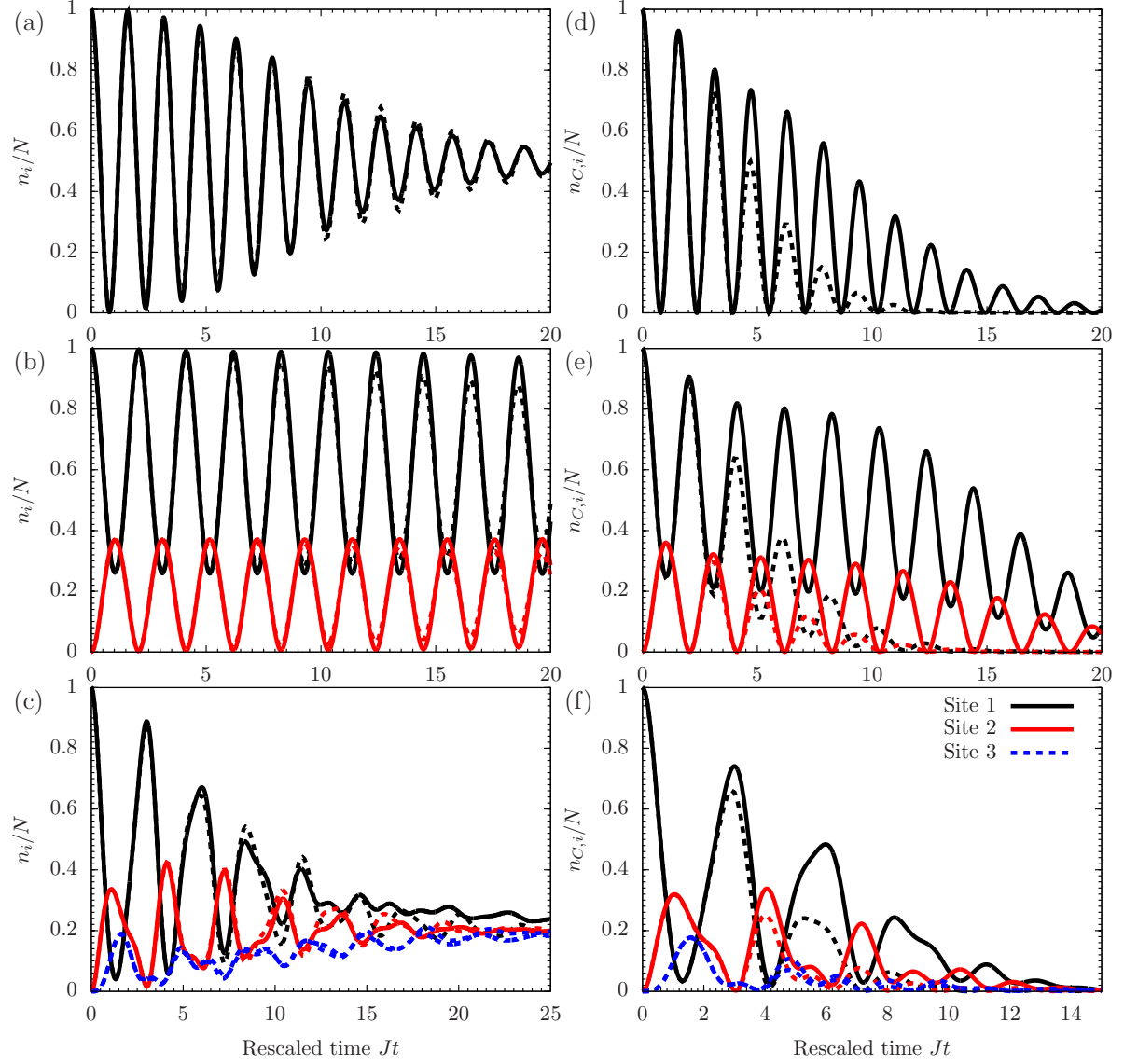
FIGURE 6.3:   Evolution of the condensate fraction of a gas on a lattice where all atoms are initially condensed in the first site. The average particle number is fixed to $N/N_S = 10$. The number of site varies, $N_S = 2, 3, 5, 10$. The color of the corresponding curve is given in the legend. All simulations are done for $U/J = 0.05$. The left panel presents the total condensate fraction for the 2PI simulation (full line) and for classical evolution (dashed line). The normalized difference between those two is shown in the right panel on a logarithmic scale.

however an exception for a three-site lattice. We also notice in FIG. 6.2.(b) that the non-normalized difference between the 2PI and the classical results is very large in that case. To study further this effect, we present in FIG. 6.4 the evolution of the population in each site for a few lattice sizes, $N_S = 2, 3, 5$. Those results are presented in the top, central and bottom lines of the FIG. 6.4, respectively. The left-hand graphs show the evolution the total population on each site while the right-hand ones show the condensate fraction on the corresponding side. Each site is represented by a different color code, shown in the legend of graph (f). The sites that are not represented can be deduced from the graphs by a symmetry argument.

The evolution for a two-site consists, as expected, into a damped oscillation between those two sites. This Rabi oscillations are finally suppressed and the final occupation numbers balance to $n_i/N = 1/2$, half of the particles in each well. The evolution is more complex for five sites but the final expected value of $n_i/N = 0.2 = 1/N_S$ is eventually achieved. For three sites however, there is nearly no damping of the oscillations in the considered time scale. We do not have a final explanation for this phenomenon, but we expect it to be some geometric properties that occur only in a triangular lattice. Comparing the 2PI results with the classical simulations for the total population in each well, we see a very good agreement. So the evolution of the total population is well reproduced by the 2PI $1/\mathcal{N}$ expansion.

On the right-hand side of FIG. 6.4, we present the evolution of the condensate fraction per site. The oscillations of the condensate follow the movement of the particle

FIGURE 6.4: Evolution of the particle population of several sites under the same conditions as in FIG. 6.3 for various number of site N_S. The first line presents the case $N_S = 2$, the second $N_S = 3$ and the last $N_S = 5$. The left side presents the total occupation of the concerned site, while the right side only the condensate fraction on that site. The color code presented in panel (f) is also valid for the other graphs. The full line represents the 2PI evolution and the dashed line the classical one. The sites that are not shown can be deduced from a symmetry argument. The damping of the oscillations for $N_S = 4$ (not shown here) happens in the same time scale as for $N_S = 5$.

between the wells. The damping to zero follows the depletion of the condensate. We notice again that the condensate fraction is overestimated by the 2PI results. The total occupation $\langle \hat{b}_i^\dagger \hat{b}_i \rangle$ contains no information about phases, see Sect. 6.2.2. On the other hand, the condensate fraction measures the phase coherence of the complex mean field $b_i = (\phi_i^0 + i\phi_i^1)/\sqrt{2}$, see Eq. (6.14). Since the 2PI results reproduce properly the total occupation per site but not the local condensate fraction, we can conclude that the 2PI $1/\mathcal{N}$ expansion that information about the phases of the system is not well taken into account. Hence, we find a clear sign of the significance of higher-order correlations left out at the level of the approximation.

6.4   Conclusion and outlook

In this chapter, we have shown how one can implement the 2PI $1/\mathcal{N}$ approach on a computer to solve the equations of motion numerically. We have indicated how to use the multiple cores of modern processors in order to speed up the execution of the simulation. Then, we used it in comparison with classical statistical simulations in order to understand better the validity of that approach in regimes where the classical evolution is expected to be valid.

Our study focused on the evolution of the condensate fraction for different lattice sizes. The results from the 2PI expansion is in better agreement with classical simulations for increasing lattice sizes. However, no perfect agreement is reached even for larger lattices. This points to a general limitation of the NLO $1/\mathcal{N}$ approximation at large couplings.

Finally, some open questions are still left unanswered and would require further investigation. The dynamics of a three-site lattice seems to be a special case when it is initially loaded on a single site. It would be of interest to understand the reasons of this particularity, that we expect to be of geometric nature. Also, we see that the 2PI $1/\mathcal{N}$ expansion is efficient at reproducing the total occupation of each lattice site, but fails to provide a correct description of the phase evolution. Understanding this effect in more details would improve our understanding of the 2PI $1/\mathcal{N}$ expansion.

Chapter 7

Summary

In the first part of the thesis, we have studied in detail the production of squeezed states in an ultracold Bose gas in a double-well trap. The trapping parameters were chosen as in the experiment [Estè08] such that at the temperatures considered, the system can be described by a two-site Bose-Hubbard Hamiltonian. Following the experimental procedure, the gas is initially confined by a double-well trap with very weak interwell barrier such that free tunneling is possible between the sites. We studied the time evolution of the system under a slow but non-adiabatic ramp-up of the barrier, in particular with respect to the change in the variance of the particle number difference between the sites and the coherence which is related to the expectation value of the relative phase. In this way a many-body state with squeezing in the particle number difference, i.e., reduced variance of this observable at the expense of the variance of the relative phase, is prepared.

Our results confirm that the squeezing attainable with a finite barrier ramp-up speed is limited to a value depending on the initial temperature and the ramp speed. This dependence is determined by the spectrum of the model Hamiltonian in which the low-energy states become quasi-degenerate below a certain ratio of the tunneling rate over the on-site energy. Once the tunneling is sufficiently suppressed such that the two lowest states are separated by a frequency on the order of the inverse ramp rate, the squeezing saturates.

We have formulated the model and dynamic equations in terms of Bloch angular momentum operators and their correlation functions to obtain a pictorial description of the underlying dynamics and exhibit the connection to spin squeezing. Beyond a qualitative understanding of the experimental data of Ref. [Estè08], our focus was set on the distinction between quantum and classical statistical fluctuations. For this, classical statistical simulations were conducted and compared to the full quantum evolution and a description in terms of the Wigner function. Our results show that within the

parameter regime realized in the experiment, the production of squeezing is an entirely classical process. Squeezing below the classical limit is possible, however, due to the low degree of degeneracy in the system, only at significantly lower temperatures than in the experiment.

The detection of such squeezing and quantum correlations requires the measurement of particle number at the single-particle level. Crucial differences arise for systems with an even total particle number as compared to such with an odd number. The results are readily applicable to other realizations which can be described by the model employed. We have shown that in the regime where quantum fluctuations become relevant, maximum squeezing is in general not achievable starting from mixtures of energy eigenstates and invoking near-adiabatic parameter changes. We emphasize that our results may be particularly interesting for mesoscopic dynamics experiments.

In the second part of the thesis, we expanded our study to traps with a larger amount of sites. As exact numerical integration of the equations of motion is generally not possible for larger lattices, we introduced a far-from-equilibrium quantum field theory method, the so-called two-particle-irreducible effective action approach. The truncation was used to make the problem solvable numerically, the non-pertubative $1/\mathcal{N}$ next-to-leading order expansion. The resulting dynamics was compared to the classical statistical time evolution. We have shown how one can implement the 2PI $1/\mathcal{N}$ approach on a computer to solve the equations of motion numerically. We have indicated how to use the multiple cores of modern processors in order to speed up the execution of the simulation.

We have limited our study to the semi-classical regime and used classical statistical calculations as a reference in order to test the validity of the quantum field theory method. In the initial states we consider, all particles are condensed on a single site. The lattice is taken with periodic boundary conditions. At later times, we study the distribution of the atoms on the lattice and the damping of the condensate fraction.

Our investigations have shown that the results from the 2PI expansion is in better agreement with classical simulation for increasing lattice sizes and larger total number of particles. However, no perfect agreement is reached even for larger lattices. This points to a general limitation of the NLO $1/\mathcal{N}$ approximation at large couplings. The three-site lattice was found to be a special case compared to larger and smaller lattices. Also, we have seen that the 2PI $1/\mathcal{N}$ expansion is efficient at reproducing the total occupation of each lattice site, but fails to provide a correct description of the phase evolution. We interpret this as a sign of the significance of higher-order correlations that are left out at the level of the approximation.

Finally, some open questions are still left unanswered. The reason of the particular nature of the three-site lattice are not yet know. A better understanding of the phase evolution in the 2PI approach would require further investigations.

Appendix A

Wigner function of two-mode states

The Wigner function of a two-mode system can be calculated from its definition

$$W(\alpha, \beta) = \frac{1}{\pi^4} \int \mathrm{d}^2\lambda \, \mathrm{d}^2\mu \, C_S(\lambda, \mu) e^{\alpha\lambda^\star - \alpha^\star\lambda} e^{\beta\mu^\star - \beta^\star\mu}, \tag{A.1}$$

where C_S is the symmetrically ordered characteristic function, which one obtains as follows [Barn97]. See also Ref. [Dowl94] for a detailed discussion of two-mode Wigner functions on the Bloch sphere. First, the Q-function

$$Q(\alpha, \beta) = \frac{1}{\pi^2} \langle \alpha, \beta | \hat{\rho} | \alpha, \beta \rangle \tag{A.2}$$

is determined as the expectation value of the density matrix $\hat{\rho}$ with respect to the two-mode coherent state

$$|\alpha, \beta\rangle = e^{-(|\alpha|^2 + |\beta|^2)/2} \sum_{i,j=0}^{\infty} \frac{\alpha^i \beta^j}{\sqrt{i!j!}} |i\rangle_l |j\rangle_r. \tag{A.3}$$

The antinormally ordered characteristic function is then obtained by Fourier transforming the Q-function,

$$C_A(\lambda, \mu) = \int \mathrm{d}^2\alpha \, \mathrm{d}^2\beta \, Q(\alpha, \beta) \, e^{\lambda\alpha^\star - \lambda^\star\alpha} e^{\mu\beta^\star - \mu^\star\beta}. \tag{A.4}$$

The symmetrically ordered characteristic function is finally calculated using the Baker-Campbell-Hausdorff relation, leading to

$$C_S(\lambda, \mu) = C_A(\lambda, \mu) \, e^{(|\lambda|^2 + |\mu|^2)/2}, \tag{A.5}$$

and from this the Wigner function by use of Eq. (A.1).

Applying this procedure and using the representation of the density matrix in the Fock basis (3.6), $|n\rangle = |N/2 + n, N/2 - n\rangle$,

$$\rho_{nm} = \langle n|\hat{\rho}|m\rangle, \tag{A.6}$$

we arrive at

$$W(\alpha, \beta) = \frac{4^{1-N}}{\pi^2} \sum_{n,m=0}^{N} \frac{\rho_{nm}}{\sqrt{n!m!(N-n)!(N-m)!}} \tag{A.7}$$
$$\times \; \Omega_{nm}(\alpha)\Omega_{N-n\;N-m}(\beta)e^{-2(|\alpha|^2+|\beta^2|)},$$

with

$$\Omega_{nm}(\alpha) = \sum_{k=0}^{n} \binom{n}{k} \sum_{l=0}^{m} \binom{m}{l} (-1)^k i^{k+l} \tag{A.8}$$
$$\times \; H_{k+l}(2\operatorname{Im}\alpha)H_{n+m-(k+l)}(2\operatorname{Re}\alpha).$$

where $H_n(x)$ is the nth Hermite polynomial. Eqs. (A.7) and (A.8) show that W is real if ρ is hermitian.

As we only consider closed systems, the dependence of W on the absolute phase of the two modes is irrelevant. We therefore need to evaluate W only for different relative phases ϕ, choosing, e.g.,

$$\alpha = |\alpha|e^{i\phi/2}, \qquad \beta = |\beta|e^{-i\phi/2}. \tag{A.9}$$

Taking furthermore into account that the total number of particles $N = |\alpha|^2 + |\beta|^2$ is fixed reduces the number of free arguments of W to two, the quantities $n = (|\alpha|^2 - |\beta|^2)/2$ and $\phi = 2\arg(\alpha)$.

Bibliography

[Aart02]   G. Aarts, D. Ahrensmeier, R. Baier, J. Berges, and J. Serreau. *"Far-from-equilibrium dynamics with broken symmetries from the* 2PI-1/$\mathcal{N}$ *expansion"*. Phys. Rev. D **66**, 045008 (2002).

[Ande95]   M. H. Anderson, J. R. Ensher, M. R. Matthews, C. E. Wieman, and E. A. Cornell. *"Observation of Bose-Einstein Condensation in a Dilute Atomic Vapor"*. Science **269**, 198 (1995).

[Appe09]   J. Appel, P. J. Windpassinger, D. Oblak, U. B. Hoff, N. Kjærgaard, and E. S. Polzik. *"Mesoscopic atomic entanglement for precision measurements beyond the standard quantum limit"*. Proc. Natl. Acad. Sci. U.S.A. **106**, 10960–10965 (2009).

[Arci06]   O. Arcizet, P.-F. Cohadon, T. Briant, M. Pinard, A. Heidmann, J.-M. Mackowski, C. Michel, L. Pinard, O. Français, and L. Rousseau. *"High-Sensitivity Optical Monitoring of a Micromechanical Resonator with a Quantum-Limited Optomechanical Sensor"*. Phys. Rev. Lett. **97**, 133601 (2006).

[Arri05]   A. Arrizabalaga, J. Smit, and A. Tranberg. *"Equilibration in ϕ^4 theory in $3+1$ dimensions"*. Phys. Rev. D **72**, 025014 (2005).

[Asch76]   N. W. Aschcroft and N. D. Mermin. *"Solid State Physics"*. W. B. Saunders Company (1976).

[Barn97]   S. M. Barnett and P. M. Radmore. *"Methods in Theoretical Quantum Optics"*. Clarendon Press, Oxford (1997).

[Baym62]   G. Baym. *"Self-Consistent Approximations in Many-Body Systems"*. Phys. Rev. **127**, 1391 (1962).

[Bely58]   S. T. Belyaev. *"Applications of the methods of quantum field theory to a system of bosons"*. Sov. Phys. JETP **7**, 289 (1958).

[Benn93]   C. H. Bennett, G. Brassard, C. Crépeau, R. Josza, A. Peres, and W. K. Wootters. *"Teleporting an unknown quantum state via dual classical and Einstein-Podolsky-Rosen channels"*. Phys. Rev. Lett. **70**, 1895 (1993).

[Berg01]   J. Berges and J. Cox. *"Thermalization of quantum fields from time reversal invariant evolution equations"*. Phys. Lett. **B517**, 369 (2001).

[Berg05]   J. Berges. *"Introduction to Nonequilibrium Quantum Field Theory"*. eprint hep-ph/0409233; AIP Conf. Proc. **739**, 3 (2005).

[Berg07]   J. Berges and T. Gasenzer. *"Quantum versus classical statistical dynamics of an ultracold Bose gas"*. Phys. Rev. A **76**, 033604 (2007).

[Blak08]   P. B. Blakie, A. S. Bradley, M. J. Davis, R. J. Ballagh, and C. W. Gardiner. *"Dynamics and statistical mechanics of ultra-cold Bose gases using c-field techniques"*. Adv. Phys. **57**, 363 (2008).

[Boll96]   J. J. Bollinger, W. M. Itano, D. J. Wineland, and D. J. Heinzen. *"Optimal frequency measurements with maximally correlated states"*. Phys. Rev. A **54**, R4649 (1996).

[Bose24]   S. N. Bose. *"Plancks Gesetz und Lichtquantenhypothese"*. [Am. J. Phys. **44**, 1056 (1976)] Z. Phys. **26**, 178 (1924).

[Box58]   G. E. P. Box and M. E. Muller. *"A Note on the Generation of Random Normal Deviates"*. Ann. Math. Statist. **29**, 610–611 (1958).

[Brau98]   S. L. Braunstein and H. J. Kimble. *"Teleportation of Continuous Quantum Variables"*. Phys. Rev. Lett. **80**, 869 (1998).

[Bulj08]   H. Buljan, R. Pezer, and T. Gasenzer. *"Fermi-Bose transformation for the time-dependent Lieb-Liniger gas"*. Phys. Rev. Lett. **100**, 080406 (2008).

[Cira98]   J. I. Cirac, M. Lewenstein, K. Mølmer, and P. Zoller. *"Quantum superposition states of Bose-Einstein condensates"*. Phys. Rev. A **57**, 1208–1218 (1998).

[Cond29]   E. Condon. *"Remarks on uncertainty principles"*. Science **69**, 573–574 (1929).

[Corn74]   J. M. Cornwall, R. Jackiw, and E. Tomboulis. *"Effective action for composite operators"*. Phys. Rev. D **10**, 2428 (1974).

[Davi95]   K. B. Davis, M.-O. Mewes, M. R. Andrews, N. J. van Druten, D. S. Durfee, D. M. Kurn, and W. Ketterle. *"Bose-Einstein Condensation in a Gas of Sodium Atoms"*. Phys. Rev. Lett. **75**, 3969 (1995).

[Dowl94]   J. P. Dowling, G. S. Agarwal, and W. P. Schleich. *"Wigner distribution of a general angular-momentum state: Applications to a collection of two-level atoms"*. Phys. Rev. A **49**, 4101 (1994).

[Dunn01]   J. A. Dunningham, K. Burnett, and M. Edwards. *"Relative number squeezing in Bose-Einstein condensates"*. Phys. Rev. A **64**, 015601 (2001).

[Dunn02]   J. A. Dunningham, K. Burnett, and S. M. Barnett. *"Interferometry below the Standard Quantum Limit with Bose-Einstein Condensates"*. Phys. Rev. Lett. **89**, 150401 (2002).

[Dunn99]   J. A. Dunningham and K. Burnett. *"Phase Standard for Bose-Einstein Condensates"*. Phys. Rev. Lett. **82**, 3729 (1999).

[Eins24]   A. Einstein. *"Quantentheorie des einatomigen idealen Gases"*. Sitzungsber. Kgl. Preuss. Akad. Wiss., Phys. Math. Kl. **1924**, 261 (1924).

[Estè08]   J. Estève, C. Gross, A. Weller, S. Giovanazzi, and M. K. Oberthaler. *"Squeezing and entanglement in a Bose-Einstein condensate"*. Nature Physics **455**, 1216 (2008).

[Fern08]   T. Fernholz, H. Krauter, K. Jensen, J. F. Sherson, A. S. S. rensen, and E. S. Polzik. *"Spin Squeezing of Atomic Ensembles via Nuclear-Electronic Spin Entanglement"*. Phys. Rev. Lett. **101**, 073601 (2008).

[Gara98]   D. A. Garanin, X. M. Hidalgo, and E. M. Chudnovsky. *"Quantum-classical transition of the escape rate of a uniaxial spin system in an arbitrarily directed field"*. Phys. Rev. B **57**, 13639 (1998).

[Gase05]   T. Gasenzer, J. Berges, M. G. Schmidt, and M. Seco. *"Non-perturbative dynamical many-body theory of a Bose-Einstein condensate"*. Phys. Rev. A **72**, 063604 (2005).

[Gase08]   T. Gasenzer and J. M. Pawlowski. *"Towards far-from-equilibrium quantum field dynamics: A functional renormalisation-group approach"*. Phys. Lett. **B670**, 135–140 (2008).

[Gati06]   R. Gati, M. Albiez, J. Fölling, B. Hemmerling, and M. K. Oberthaler. *"Realization of a single Josephson junction for Bose-Einstein condensates"*. Appl. Phys. B **82**, 207 (2006).

[Gerb06]   F. Gerbier, S. Fölling, A. Widera, O. Mandel, and I. Bloch. *"Probing Number Squeezing of Ultracold Atoms across the Superfluid-Mott Insulator Transition"*. Phys. Rev. Lett. **96**, 090401 (2006).

[Giov04]   V. Giovannetti, S. Lloyd, and L. Maccone. *"Quantum-Enhanced Measure-ments: Beating the Standard Quantum Limit"*. Science **306**, 1330–1336 (2004).

[Giov06]   V. Giovannetti, S. Lloyd, and L. Maccone. *"Quantum Metrology"*. Phys. Rev. Lett. **96**, 010401 (2006).

[Giov08]   S. Giovanazzi, J. Esteve, and M. K. Oberthaler. *"Effective parameters for weakly coupled Bose-Einstein condensates"*. New Journal of Physics **10**, 045009 (2008).

[Glic65]   A. J. Glick, H. J. Lipkin, and N. Meshkov. *"Validity of many-body approx-imation methods for a solvable model : (III). Diagram summations"*. Nucl. Phys. **62**, 211 (1965).

[Goda08]   K. Goda, O. Miyakawa, E. E. Mikhailov, S. Saraf, R. Adhikari, K. McKenzie, R. Ward, S. Vass, A. J. Weinstein, and N. Mavalvala. *"A quantum-enhanced prototype gravitational-wave detector"*. Nature Phys. **4**, 472 (2008).

[Grei02]   M. Greiner, O. Mandel, T. W. Hänsch, and I. Bloch. *"Collapse and revival of the matter wave field of a Bose-Einstein condensate"*. Nature (London) **419**, 51 (2002).

[Gros10]   C. Gross, T. Zibold, E. Nicklas, J. Estève, and M. K. Oberthaler. *"Nonlinear atom interferometer surpasses classical precision limit"*. Nature **464**, 1165–1169 (2010).

[Gros61]   E. P. Gross. *"Structure of a Quantized Vortex in Boson Systems"*. Nuovo Cim. **20**, 454 (1961).

[Hald99]   J. Hald, J. L. Sørensen, C. Schori, and E. S. Polzik. *"Spin Squeezed Atoms: A Macroscopic Entangled Ensemble Created by Light"*. Phys. Rev. Lett. **83**, 1319 (1999).

[Hatf86]   B. Hatfield. *"Quantum Field Theory of Point Particles and Strings"*. Addison-Wesley fourth Ed. (1986).

[Heis27]   W. Heisenberg. *"Über den anschulichen Inhalt der quantentheoretischen Kinematik und Mechanik"*. Z. Phys. **43**, 172–198 (1927).

[Holl93]   M. J. Holland and K. Burnett. *"Interferometric detection of optical phase shifts at the Heisenberg limit"*. Phys. Rev. Lett. **71**, 1355 (1993).

[Huel97]   S. F. Huelga, C. Macchiavello, T. Pellizzari, A. K. Ekert, M. B. Plenio, and J. I. Cirac. *"Improvement of Frequency Standards with Quantum Entanglement"*. Phys. Rev. Lett. **79**, 3865 (1997).

[Isel05]   L. Isella and J. Ruostekoski. *"Nonadiabatic dynamics of a Bose-Einstein condensate in an optical lattice"*. Phys. Rev. A **72**, 011601(R) (2005).

[Isel06]   L. Isella and J. Ruostekoski. *"Quantum dynamics in splitting a harmonically trapped Bose-Einstein condensate by an optical lattice: Truncated Wigner approximation"*. Phys. Rev. A **74**, 063625 (2006).

[Jaks05]   D. Jaksch and P. Zoller. *"The cold atom Hubbard toolbox"*. Ann. Phys. **52**, 315 (2005).

[Java99]   J. Javanainen and M. Y. Ivanov. *"Splitting a trap containing a Bose-Einstein condensate: Atom number fluctuations"*. Phys. Rev. A **60**, 2351 (1999).

[Jo07]   G.-B. Jo, Y. Shin, S. Will, T. A. Pasquini, M. Saba, W. Ketterle, D. E. Pritchard, M. Vengalattore, and M. Prentiss. *"Long Phase Coherence Time and Number Squeezing of Two Bose-Einstein Condensates on an Atom Chip"*. Phys. Rev. Lett. **98**, 030407 (2007).

[Kim98]   T. Kim, O. Pfister, M. J. Holland, J. Noh, and J. L. Hall. *"Influence of decorrelation on Heisenberg-limited interferometry with quantum correlated photons"*. Phys. Rev. A **57**, 4004 (1998).

[Kita93]   M. Kitagawa and M. Ueda. *"Squeezed spin states"*. Phys. Rev. A **47**, 5138 (1993).

[Kohn59]   W. Kohn. *"Analytic Properties of Bloch Waves and Wannier Functions"*. Phys. Rev. **115**, 809 (1959).

[Legg01]   A. J. Leggett. *"Bose-Einstein condensation in the alkali gases: Some fundamental concepts"*. Rev. Mod. Phys. **73**, 307 (2001).

[Li07]   W. Li, A. K. Tuchman, H.-C. Chien, and M. A. Kasevich. *"Extended Coherence Time with Atom-Number Squeezed States"*. Phys. Rev. Lett. **98**, 040402 (2007).

[Lieb63]   E. H. Lieb and W. Liniger. *"Exact Analysis of an Interacting Bose Gas. I. The General Solution and the Ground State"*. Phys. Rev. **130**, 1605 (1963).

[Lipk65]   H. J. Lipkin, N. Meshkov, and A. J. Glick. *"Validity of many-body approximation methods for a solvable model : (I). Exact solutions and perturbation theory"*. Nucl. Phys. **62**, 188 (1965).

[Lutt60]   J. M. Luttinger and J. C. Ward. *"Ground-State Energy of a Many-Fermion System. II"*. Phys. Rev. **118**, 1417 (1960).

[Mahm03] K. W. Mahmud, H. Perry, and W. P. Reinhardt. *"Phase engineering of controlled entangled number states in a single component Bose-Einstein condensate in a double well"*. J. Phys. B: At. Mol. Opt. Phys. **36**, L265 (2003).

[Meno01]   C. Menotti, J. R. Anglin, J. I. Cirac, and P. Zoller. *"Dynamic splitting of a Bose-Einstein condensate"*. Phys. Rev. A **63**, 023601 (2001).

[Mesh65]   N. Meshkov, A. J. Glick, and H. J. Lipkin. *"Validity of many-body approximation methods for a solvable model : (II). Linearization procedures"*. Nucl. Phys. **62**, 199 (1965).

[Mess00]   A. Messiah. *"Quantum Mechanics"*. Dover Publications (2000).

[Meye01]   V. Meyer, M. A. Rowe, D. Kielpinski, C. A. Sackett, W. M. Itano, C. Monroe, and D. J. Wineland. *"Experimental Demonstration of Entanglement-Enhanced Rotation Angle Estimation Using Trapped Ions"*. Phys. Rev. Lett. **86**, 5870 (2001).

[Orús08]   R. Orús, S. Dusuel, and J. Vidal. *"Equivalence of Critical Scaling Laws for Many-Body Entanglement in the Lipkin-Meshkov-Glick Model"*. Phys. Rev. Lett. **101**, 025701 (2008).

[Orze01]   C. Orzel, A. K. Tuchman, M. L. Fenselau, M. Yasuda, and M. A. Kasevich. *"Squeezed States in a Bose-Einstein Condensate"*. Science **291**, 2368 (2001).

[Para01]   G.-S. Paraoanu, S. Kohler, F. Sols, and A. J. Leggett. *"The Josephson plasmon as a Bogoliubov quasiparticle"*. J. Phys. B: At. Mol. Opt. Phys. **34**, 4689 (2001).

[Peil03]   S. Peil, J. V. Porto, B. L. Tolra, J. M. Obrecht, B. E. King, M. Subbotin, S. L. Rolston, and W. D. Phillips. *"Patterned loading of a Bose-Einstein condensate into an optical lattice"*. Phys. Rev. A **67**, 051603(R) (2003).

[Pita61]   L. P. Pitaevskii. *"Vortex Lines in an Imperfect Bose gas"*. [Zh. Eksp. Teor. Fiz. 40, 646 (1961)] Sov. Phys. JETP **13**, 451 (1961).

[Polk09]   A. Polkovnikov. *"Representation of quantum dynamics of interacting systems through classical trajectories"*. eprint version at arXiv:0905.3384v1 [cond-mat.stat-mech] (2009).

[Popo87]   V. N. Popov. *"Functional Integrals and Collective Excitations"*. Vol. CUP, Cambridge (1987).

[Pres07]   W. H. Press, S. A. Teukolsky, W. T. Vetterling, and B. P. Flannery. *"Numerical Recipes: The Art of Scientific Computing"*. Cambridge University Press third Ed. (2007).

[Ragh99]   S. Raghavan, A. Smerzi, S. Fantoni, and S. R. Shenoy. *"Coherent oscillations between two weakly coupled Bose-Einstein condensates: Josephson effects, π oscillations, and macroscopic quantum self-trapping"*. Phys. Rev. A **59**, 620–633 (1999).

[Rams50]   N. F. Ramsey. *"A Molecular Beam Resonance Method with Separated Oscillating Fields"*. Phys. Rev. **78**, 695 (1950).

[Rey04]   A. Rey, B. Hu, E. Calzetta, A. Roura, and C. Clark. *"Nonequilibrium dynamics of optical-lattice-loaded Bose-Einstein-condensate atoms: Beyond the Hartree-Fock-Bogoliubov approximation"*. Phys. Rev. A **69**, 033610 (2004).

[Ribe07]   P. Ribeiro, J. Vidal, and R. Mosseri. *"Thermodynamical Limit of the Lipkin-Meshkov-Glick Model"*. Phys. Rev. Lett. **99**, 050402 (2007).

[Ribe08]   P. Ribeiro, J. Vidal, and R. Mosseri. *"Exact spectrum of the Lipkin-Meshkov-Glick model in the thermodynamic limit and finite-size corrections"*. Phys. Rev. E **78**, 021106 (2008).

[Robe29]   H. P. Robertson. *"The Uncertainty Principle"*. Phys. Rev. **34**, 163 (1929).

[Salg07]   A. N. Salgueiro, A. F. R. de Toledo Piza, G. B. Lemos, R. Drumond, M. C. Nemes, and M.Weidemüller. *"Quantum dynamics of bosons in a double-well potential: Josephson oscillations, self-trapping and ultralong tunneling times"*. Eur. Phys. J. D **44**, 537 (2007).

[Sant99]   G. Santarelli, P. Laurent, P. Lemonde, A. Clairon, A. G. Mann, S. Chang, A. N. Luiten, and C. Salomon. *"Quantum Projection Noise in an Atomic Fountain: A High Stability Cesium Frequency Standard"*. Phys. Rev. Lett. **82**, 4619–4622 (1999).

[Schl08]   M. H. Schleier-Smith, I. D. Leroux, and V. Vuletix. *"Reduced-quantum-uncertainty states of an ensemble of two-level atoms."*. eprint on arXiv: 0810.2582v2 [quant-ph] (2008).

[Scho05]   U. Schollwöck. *"The density matrix renormalization group"*. Rev. Mod. Phys. **77**, 259 (2005).

[Schw61]   J. Schwinger. *"Brownian Motion of a Quantum Oscillator"*. J. Math. Phys. **2**, 407 (1961).

[Schw65]   J. Schwinger. *"On Angular Momentum"*. In: L. Beidenharn and H. van Dam, Eds., *Quantum Theory of Angular Momentum: A collection of reprints an original papers* (page 229) Academic Press, New York (1965).

[Sebb07]   J. Sebby-Strabley, B. L. Brown, M. Anderlini, P. J. Lee, W. D. Phillips, J. V. Porto, and P. R. Johnson. *"Preparing and Probing Atomic Number States with an Atom Interferometer"*. Phys. Rev. Lett. **98**, 200405 (2007).

[Søre01a] A. Sørensen, L.-M. Duan, J. I. Cirac, and P. Zoller. *"Many-particle entanglement with Bose-Einstein condensates"*. Nature (London) **409**, 63 (2001).

[Søre01b] A. S. Sørensen and K. Mølmer. *"Entanglement and Extreme Spin Squeezing"*. Phys. Rev. Lett. **86**, 4431 (2001).

[Spek99]   R. W. Spekkens and J. E. Sipe. *"Spatial fragmentation of a Bose-Einstein condensate in a double-well potential"*. Phys. Rev. A **59**, 3868–3877 (1999).

[Stee98a] M. J. Steel and M. J. Collett. *"Quantum state of two trapped Bose-Einstein condensates with a Josephson coupling"*. Phys. Rev. A **57**, 2920 (1998).

[Stee98b] M. J. Steel, M. K. Olsen, L. I. Plimak, P. D. Drummond, S. M. Tan, M. J. Collett, D. F. Walls, and R. Graham. *"Dynamical quantum noise in trapped Bose-Einstein condensates"*. Phys. Rev. A **58**, 4824–4835 (1998).

[Stre04]   A. I. Streltsov, L. S. Cederbaum, and N. Moiseyev. *"Ground-state fragmentation of repulsive Bose-Einstein condensates in double-trap potentials"*. Phys. Rev. A **70**, 053607 (2004).

[Stre07]   A. I. Streltsov, O. E. Alon, and L. S. Cederbaum. *"Role of Excited States in the Splitting of a Trapped Interacting Bose-Einstein Condensate by a Time-Dependent Barrier"*. Phys. Rev. Lett. **99**, 030402 (2007).

[Temm06]   K. Temme and T. Gasenzer. *"Non-equilibrium dynamics of condensates in a lattice from the 2PI effective action in $1/\mathcal{N}$ expansion"*. Phys. Rev. A **74**, 053603 (2006).

[Trim08]   F. Trimborn, D. Witthaut, and H. J. Korsch. *"Exact number-conserving phase-space dynamics of the M-site Bose-Hubbard model"*. Phys. Rev. A **77**, 043631 (2008).

[Trim09]   F. Trimborn, D. Witthaut, and H. J. Korsch. *"Beyond mean-field dynamics of small Bose-Hubbard systems based on the number-conserving phase-space approach"*. Phys. Rev. A **79**, 013608 (2009).

[Vaid94]   L. Vaidman. *"Teleportation of quantum states"*. Phys. Rev. A **49**, 1473 (1994).

[Vida04]   G. Vidal. *"Efficient Simulation of One-Dimensional Quantum Many-Body Systems"*. Phys. Rev. Lett. **93**, 040502 (2004).

[Wall94]   D. F. Walls and G. J. Milburn. *"Quantum Optics"*. Vol. Springer, Berlin (1994).

[Whit04]   S. R. White and A. E. Feiguin. *"Real-Time Evolution Using the Density Matrix Renormalization Group"*. Phys. Rev. Lett. **93**, 076401 (2004).

[Wine92]   D. J. Wineland, J. J. Bollinger, W. M. Itano, F. L. Moore, and D. J. Heinzen. *"Spin squeezing and reduced quantum noise in spectroscopy"*. Phys. Rev. A **46**, R6797 (1992).

[Wine94]   D. J. Wineland, J. J. Bollinger, W. M. Itano, and D. J. Heinzen. *"Squeezed atomic states and projection noise in spectroscopy"*. Phys. Rev. A **50**, 67 (1994).

[Zima64]   J. M. Ziman. *"Principles of the Theory of Solids"*. Cambridge University Press (1964).